Polarisation-Tunable Plasmonic Devices

Paul Gordon Thompson

A dissertation submitted for the degree of Doctor of Philosophy

School of Electronic and Electrical Engineering

University College London

May, 2012

I, Paul Gordon Thompson confirm that the work presented in this thesis is my own. Where information has been derived from other sources, I confirm that this has been indicated in the thesis.

For my parents,
Marion and Victor Thompson

Acknowledgements

I would like to thank my supervisor, Dr. Paul Warburton, for all his kind assistance and patient guidance throughout the course of my research. I would also like to thank Dr. Nicolae Panoiu for his invaluable help in aiding my understanding of plasmonics. In addition, I am also very grateful to Edward Osley for helping me to improve my FIB skills and to Claudiu Biris for providing simulations and assisting me in understanding simulation software. Their input has been invaluable during the course of my research. I would also like to extend my thanks to Prof. Paul McMillan for providing some of the facilities necessary for my research.

I thank the Engineering and Physical Sciences Research Council for providing funding for nine terms and to the Department of Electronic and Electrical Engineering for awarding me my studentship. I also wish to express my thanks to the London Centre for Nanotechnology where I carried out most of my research.

From further afield I extend my gratitude to my collaborators and coauthors at Columbia University, Prof. Richard Osgood and Ophir Gaathon.

I offer my heartfelt thanks to my friends for all the encouragement they have given to me over the many years that have led me to this point, especially Allison Tarrant and Raymond Perrier.

I would especially like to express my love and thanks to my partner Gordon McArthur for his unstinting support during my many years of full-time study. Finally I would like to thank my parents, to whom this PhD thesis is dedicated with love.

Abstract

This research project aims to investigate the phenomenon of extraordinary optical transmission (EOT) in arrays of asymmetric cruciform apertures. The specific area of EOT examined is the dependence of transmission on incident polarisation. The approach to investigating this phenomenon can be divided into three main sections: fabrication, characterisation and simulations.

The method of fabrication involved two main processes: fabrication of Au thin films on CaF_2 substrates using thermal evaporation, and the milling of cruciform apertures in the thin films using focused in beam (FIB). A 5 nm adhesion layer of Cr was first thermally evaporated onto the CaF_2 substrate followed by an Au film, typically of 30 nm thickness. The unit cells have a lattice constant of 2 μm and typical feature sizes of the apertures are between 160 nm and 1675 nm.

The transmission and reflection characteristics are examined using Fourier transform infrared spectroscopy (FTIR) for the Mid IR wavelength range. The dependence of the transmission and reflection on polarisation was investigated. It was found that the arrays display two distinct transmission maxima and a point at which transmission is invariant for all polarisations. The transmission peaks occurred in the wavelength range of 2μm to 6 μm. An ensemble of arrays was fabricated to examine the change in wavelength of the transmission peaks and the invariant point as one of the aperture dimensions was varied. It was found that the transmission wavelength and the wavelength of the invariant point could be tuned by altering the dimensions of the cruciform apertures.

Simulations for transmission and reflection were carried out in addition to field profile simulations. Together, these confirmed the assumed processes by which the polarisation dependent transmission maxima were generated, i.e. by localised surface plasmons.

One of the arrays more closely examined had transmission peaks at 3.9μm and 5.75μm and an invariant point at 4.46μm. For this array simulations were also used to determine the polarisation state of the transmitted wave. The simulations show that arrays of asymmetric apertures change the incident polarisation such that the transmitted wave becomes elliptically polarised with a major axis that is in general different from the polarisation angle of the incident wave. A maximum shift of around 33° was determined using simulations for a wavelength $\lambda = 3.9\mu m$ and an incident polarisation of 60° relative to the x axis. Experimental data was obtained that corroborates these findings.

Contents

List of Figures

Chapter 1

Introduction

1.1 The Reasons for the Interest in Extraordinary Optical Transmission

The discovery of extraordinary transmission (EOT) in 1998 [1] challenged the predicted values of classical aperture theory for transmission of electromagnetic (EM) radiation through subwavelength apertures in noble metals. The much higher than expected transmission was found to be the product of the interaction of EM radiation with electrons near the surface of a metal, collectively termed surface plasmons. Since then research related to this phenomenon has rapidly expanded and much fundamental understanding of the physical processes involved has been acquired. The interest in EOT has stemmed not only from a desire to understand the underlying physical processes that cause EOT but also from its many possible applications.

It has been proposed, for example, that by applying circuit analysis and wave guide and transmission line theory to subwavelength structures, it may be possible to produce optical information processing devices that operate at the nanometer scale [2, 3]. Another possible area that could produce applications involves the inclusion of nonlinear materials within the apertures, the nonlinear characteristics of which are augmented by the enhanced electric field that occurs in the subwavelength apertures [4]. Enhanced second-harmonic generation, for example can be obtained by the inclusion of a suitable nonlinear material such as GaAs [5]. Materials with nonlinear refractive index also could be used to implement transmission modulators at Petahertz frequencies [4]. Such devices could lead to the control of optical transmission with subwavelength planar devices. These in turn could be further developed

into integrated, miniaturised, high-density, optical-bandwidth information processing devices for use in optical storage and telecommunications.

Other possible applications include electro-optic devices such as flat-panel displays and spatial light modulators [6]. Also near-field microscopy and optical modulation have been suggested [7].

Much research has also been carried out into the use of EOT for surface-based biological or chemical detection [8, 9, 10, 11, 12]. Such detectors could be included within microfluidic devices. When a biological or chemical substance is inserted into the apertures, the wavelength of transmission increases or decreases by an amount that is characteristic of particular substances, thus enabling identification. The use of multilayer arrays of subwavelength apertures has also been proposed to obtain a left-handed metamaterial, i.e. one with negative refractive index [13, 14].

Arrays of subwavelength cruciform apertures have been fabricated that operate as plasmonic lenses for Fresnel-region focusing [15].

Arrays of apertures that display EOT are found to be frequency selective and can thus be used as filters. Such filters can be designed to be tunable, thus enabling them to operate at different wavelengths [16, 17, 18].

The motivation for my research lies in the fact that the ability to determine transmission wavelength using a change in polarisation could potentially increase the functionality of sensors that rely on transmission shift to determine the nature of a particular molecule. Two distinct transmission wavelengths could thus double the number of molecules detected. Although other methods have been adopted for achieving polarization dependence, the use or cruciform apertures has not been explored experimentally. It would

also be useful to be able to tailor the transmission wavelengths by altering the dimension of the apertures. To this end it would be interested to explore the effects of systematically adjusting aperture dimensions to determine the effect on transmission.

Additionally, it is not clear how the arrays affect the polarisation of the transmitted beam, i.e. whether there is a change in the angle of polarisation from the incident to transmitted beam and whether the transmitted beam remains linearly polarised. Any polarisation change could have potential applications as nanoscale polarisers.

In my research I have studied EOT in arrays of subwavelength asymmetric cruciform apertures fabricated in thin films of gold on a CaF_2 substrate. I have observed the effect of changing the polarisation angle of the incident MIR beam on the transmission and reflection characteristics of these arrays. I have also examined the change in transmission wavelength as one of the aperture dimensions was systematically varied. Finally, I have investigated the change in the polarisation state of the transmitted beam and have found that the transmitted polarisation is not the same as the incident polarisation and that the linearly polarised incident beam is, at most wavelengths, transmitted as an elliptically polarised beam with a major axis that is not the same as the angle of the incident polarisation. This phenomena could be exploited in photonic devices such as biosensors.

1.2 Form of the Dissertation

The dissertation begins with an introduction to extraordinary optical transmission and provides an overview of the broad range of developments in this field, before looking more closely at research related to tunability and polarisation dependence in EOT devices. Following this, Chapter 3 describes the background theory necessary to understand the phenomena observed, and the mathematical formulae necessary for processing experimental data. Chapter 4 outlines the fabrication methods used to make arrays of subwavelength cruciform apertures. The method for obtaining transmission and reflection spectra are then described in Chapter 5 and the results are presented and discussed in Chapter 6. Finally, in Chapter 7, conclusions are drawn and suggestions for further work proposed.

Chapter 2

Extraordinary Optical Transmission and Surface Plasmons

2.1 Transmission Through Subwavelength Aperture Arrays

The transmission properties of metals with arrays of periodically arranged holes, or their complementary raised structures, such as disks, have been examined since the early 1960s. In 1961 and 1962 Collin and Eggimann [19, 20] published two papers examining theoretically the microwave diffraction through two-dimensional lattices and planar arrays of subwavelength circular discs. In 1967, Ulrich [21] examined experimentally the far-infrared properties of a metallic mesh and its complementary structure of raised squares where the individual structures were smaller than the incident wavelength. Further theoretical and experimental work was carried out by Chen [22] in 1971, again in the microwave region for subwavelength circular holes. These researchers found that these hole arrays were frequency selective and this property was further investigated in the 1980s by engineers interested in their possible application in filters for solar energy collectors, improved antennae performance, polarizers, beam splitters, and mirrors for improving the pumping efficiency in molecular lasers [23, 24, 25]. For these structures, the theoretical descriptions made no mention of surface plasmons and no unusual increase in transmission was predicted or observed.

In 1998 Ebbesen *et al* [1] made a discovery that has spurred intense research into the properties of subwavelength apertures. Arrays of cylindrical apertures were fabricated on a 200 nm thick Ag film. These apertures had a diameter d = 150 nm and a periodicity in the x and y directions of Λ = 900 nm. Transmission spectra were obtained for wavelengths between

around 300 nm and 2000 nm (Fig.2.1). For specific wavelengths the zero order transmission was found to be several orders of magnitude greater than predicted by the standard aperture theory described by Bethe in 1944 [26]. Bethe's theory predicts that the transmitted intensity decreases with the hole diameter as $(d/\lambda)^4$. However, Ebbesen found that sharp peaks were observed at wavelengths that were nearly ten times as large as the cylinder diameter. When normalized to the area of the holes, the transmission at these wavelengths was found to be greater than unity.

This surprising phenomenon, referred to as Extraordinary Optical Transmission (EOT), occurs via the coupling of electromagnetic radiation with conduction electrons at the surface of metals, resulting in surface waves termed surface plasmon polaritons (SPPs). This phenomenon was predicted by Ritchie [27] in 1957 and observed experimentally using electron energy loss techniques by Powell and Swann [28] in 1959. The generation of SPPs occurs at the interface of a metal and a dielectric (such as air), and is dependent on the values of the complex dielectric constant in both the metal and the dielectric. These complex values can be defined as follows [29]:

$$\epsilon(\omega) = \epsilon'(\omega) + i\epsilon''(\omega) \tag{2.1}$$

Dielectrics have a positive value for the real part of the dielectric constant, $\epsilon'(\omega)$, while for metals this value is negative. The imaginary part of the dielectric constant, $\epsilon''(\omega)$, provides information on the dissipation, and in metals $\epsilon''(\omega)$ is proportional to the inverse of the collision time. To achieve plasmon resonances in a metal the conduction electrons need a large mean

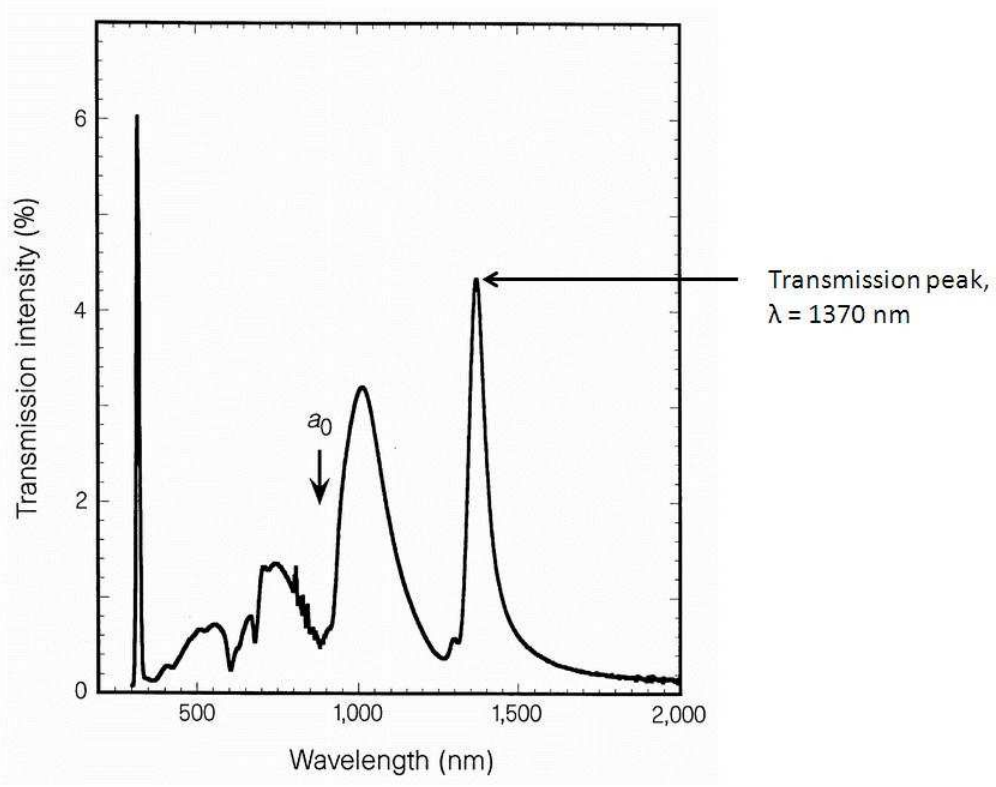

Figure 2.1: This image is taken from Ebbesen *et al* [1]. Transmission spectrum for an array of holes each with diameter 150 nm and a lattice constant $a_0 = 900$ nm in both the x and y directions. The largest transmission peak occurs at 1370 nm, nearly 10 times the diameter of the individual holes. A minimum is observed at a_0 .

free path and thus a low value for $\epsilon''(\omega)$ is desirable.

Ebbesen provided two evidences for suggesting SPPs as a probable cause of EOT. First is the absence of EOT in hole arrays fabricated in Ge films, which suggests that EOT requires metal films. Second is the angular dependence of the spectra in metal samples. Their research showed that the zero-order transmission spectra changed markedly even for angles as small

as 2 degrees from the normal (Fig. 2.2). The peaks are shown to change in intensity and split into new peaks that move in opposite directions. Such behavior is also observed when light couples with SPPs in reflection gratings [30, 31, 32, 33, 34, 35].

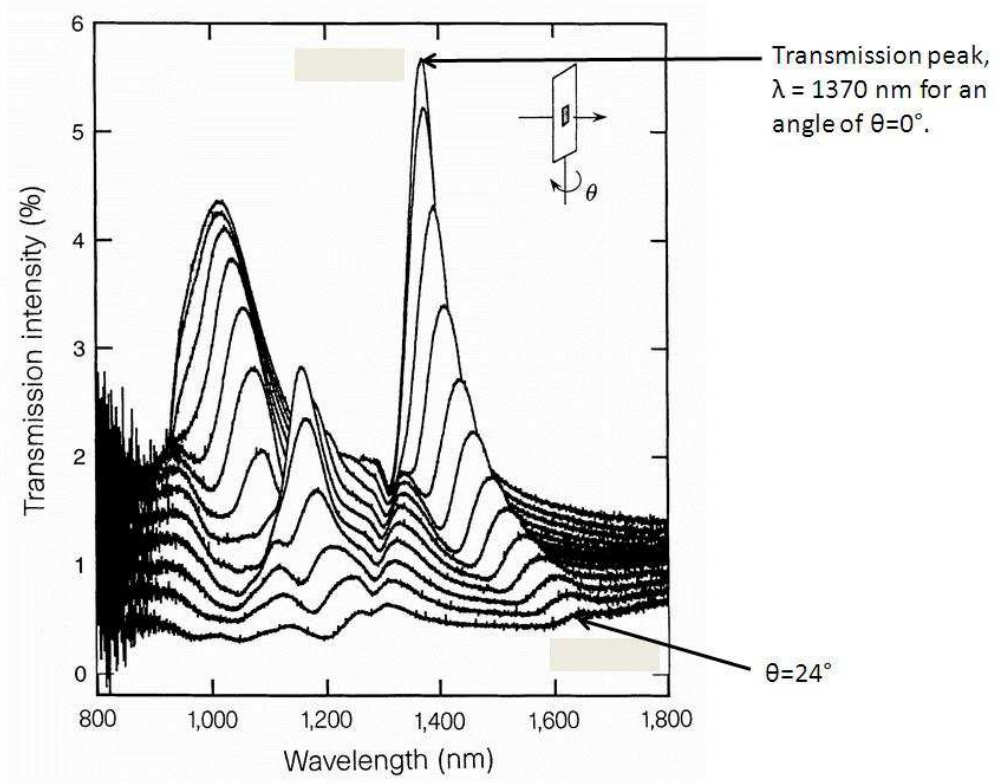

Figure 2.2: This image is taken from Ebbesen *et al* [1]. Transmission spectrum for the same array of holes in Fig. 2.1 , but showing the effect of changing angle of incidence from $\theta = 0°$ at normal incidence to $\theta = 24°$ in increments of $\theta = 2°$. The intensity decreases with increasing θ and two further peaks appear, splitting from the two main peaks, and the wavelength of their maximum transmission moves in opposite directions as θ increases.

In general SPPs can be divided into two distinct types: Propagating surface plasmons, which occur across the surface of the array and are influenced by the periodicity of the array apertures, and localised surface plasmons (LSPs) [36, 37, 38], which occur at bounded geometries. LSPs not only occur in subwavelength cavities but can also form at the surface of metallic nanoparticles, such as disks, spheres, rods and rings.

The theory that describes these interactions in subwavelength holes is still under development, but much research has been carried out to clarify the nature of these interactions. The first fully three-dimensional study of this phenomenon was described by Martín-Moreno *et al* in 2000 [7] for a metal film with a periodic array of square holes. In accordance with Babinet's principle, this phenomenon is also observed for arrays that are the inverse of hole apertures such that solid regions become apertures and apertures become solid regions [39, 40]. Since the discovery of EOT, this phenomenon has also been found to exist in single subwavelength holes that are surrounded by a pattern of indentations [41], and experiments have been carried out over a range of frequencies to ascertain the conditions under which EOT can occur.

2.2 EOT in the Terahertz, Infrared, Visible and Ultraviolet Regions

Extensive research has enabled us to produce EOT at a wide range of different wavelengths, opening the possibility of exploiting this phenomenon for many applications.

In 2003 Gomez-Rivas *et al* [29] demonstrated EOT in the terahertz region using periodic arrays of holes made in silicon wafers that were highly doped with phosphorous. For holes of size 70 x 70 μm, transmission two orders of magnitude larger than the expected classical diffraction transmission was observed. This transmission was attributed to resonant tunneling of surface-plasmon polaritons that can be excited on doped semiconductors at terahertz frequencies.

In 2006 EOT in the infrared regime was demonstrated [42] using silver films 100 nm thick, which were deposited on substrates of fused silica and zinc selenide. Nine different hole arrays were fabricated using electron beam lithography. The arrays showed a correlation between periodicity and transmission peaks with the smaller lattice constants producing transmission peaks at smaller wavelengths.

In 2007 EOT was demonstrated for ultraviolet [43]. Hole arrays were fabricated using extreme UV interference lithography and shadow thermal evaporation to produce free-standing aluminum hole arrays. Aluminium was chosen for these structures as it is considered the best metal to obtain plasmonic response in the UV region owing to its high plasmon frequency ($\omega_{p,bulk}$ = 15eV) and negligible interband transitions. Similar aluminium arrays were also fabricated on a quartz substrate. The maximum absolute transmission achieved at the resonant peak position was 38%.

Przybilla et al [44] systematically measured optical transmission spectra for the noble metals gold, silver and copper, and the transition metals Cobalt, Nickel and Tungsten. Using wavelengths between 400 and 850 nm, this research showed that those metals that could sustain surface plasmons with

low dissipation and high surface energy densities (ie. the noble metals, Ag, Au and Cu) produced the largest transmissions in the visible regime. The effect of extraordinary transmission in Cobalt and Nickel was heavily damped by the high imaginary part of their dielectric constants, while tungsten does not support SPPs in the optical regime.

2.3 The Effects of Geometry and Hole Shape on EOT

Many researchers have investigated the role of array symmetry in EOT. For example, in 2006 Sun *et al* [45] examined the role of periodicity in EOT by fabricating and characterising the transmission spectra for arrays of holes with quasiperiodicity and arrays with an amorphous arrangement of holes. The quasiperiodic arrays exhibited an enhanced transmission of around 20 percent while no enhanced transmission was observed in the amorphous arrays, indicating that long-range structural order is important for the coupling of incident light with surface plasmon modes.

The effects of geometry and hole shape have also been explored and shown to be important in EOT. In 2004, Elliot *et al* [46] examined arrays of elliptical holes and found that their transmission wavelengths had a polarisation dependence. Also in 2004 Gordon *et al* [47] examined holes of elliptical arrays by varying their orientation and aspect ratio, and found that the degree of polarisation was determined by the ellipticity and the orientation of the holes. The depolarisation ratio (i.e. the ratio of the parallel polarised trans-

mission to the perpendicular polarised transmission) was also found to have a squared dependence on the aspect ratio.

In 2004 Koerkamp *et al* [48] investigated the effects of changing the shape of the apertures (Fig. 2.3). Arrays of circular apertures, each with an area of 28353 nm^2, and arrays of rectangular apertures, each with an area of 33750 nm^2, were fabricated, each with the same periodicity and the same number of apertures. Their transmissivity was tested and the arrays of rectangular holes were found to have a transmissivity 7.3 times greater than that of the arrays of circular holes. This cannot be accounted for alone by the rectangles being 19 percent larger than the holes. They also found that reducing the area of the rectangles to 16875 nm^2 further increased the transmissivity such that their transmissivity was 9.5 times greater than the arrays of circular holes. In addition, the position of the peaks were seen to shift to longer wavelengths when the aspect ratio of the holes was increased. These effects were attributed to the existence of shape resonances in the rectangular holes.

The transmissivity of single C-shaped apertures compared to single square apertures of the same area were examined in the optical regime in Au films by Matteo [49] (2004). The C-shaped apertures were found to exhibit between 13 and 22 times transmission enhancement over the square apertures.

SPPs have also been utilized in metamaterials: materials which gain their properties from the combined effect of subwavelength structures. The individual structures may be regarded as artificial atoms [50]. These devices include perfect absorbers [51, 52], bi-anisotropic metamaterials [53], negative-index metamaterials [54, 14, 55], and chiral metamaterials [56].

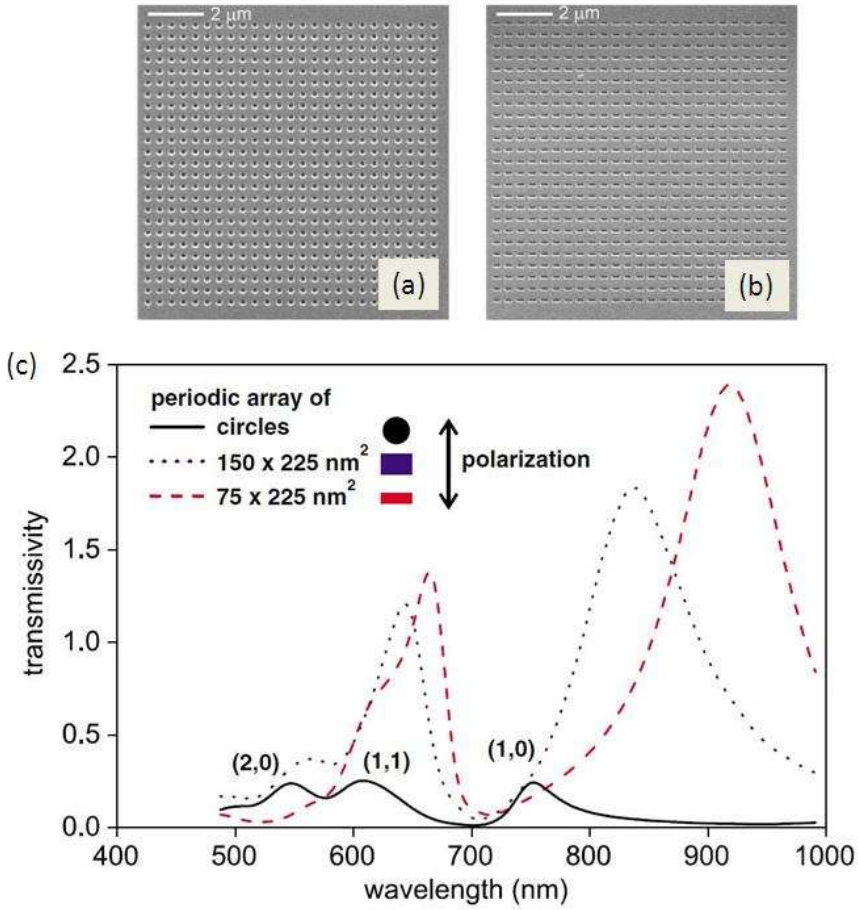

Figure 2.3: Image taken from Klein Koerkamp *et al* [48]. The scanning electron micrograph image (a) shows an array of circular holes each of diameter 190 nm and lattice constant 425 nm. Image (b) has the same lattice constant but the holes are rectangular each with dimensions 75 x 225 nm. The graph (c) shows that rectangular holes produce larger transmission peaks the positions of which red shift with increasing aspect ratio. Transmission also increases as the area of the rectangles is reduced .

2.4 Tunable Plasmonic Devices

An active area of research in plasmonic devices is in the design and fabrication of arrays that enable the transmission characteristics to be tuned. Many different approaches have been explored for controlling the transmission properties of plasmonic devices. These include optical control, in which radiation incident upon the plasmonic device affects the dielectric properties of the device and thus the transmission characteristics[57]; electrical control, in which, for example, the unit cells of an array of structures each include within their design an electrical device, each of which can be connected to a potential difference, enabling a change in voltage bias. This change can affect, for example, the carrier density of the substrate, and thus change the transmission characteristics of the plasmonic device [16]. Another method of controlling transmission is by changing the temperature of the device. In such instances a material, such as a nematic crystal, the characteristics of which are affected by temperature change, is included within the device [17]. A further method of control is by mechanical deformation of the plasmonic device, which has the effect of altering the dimensions of, for example, subwavelength structure, and thus affects the transmission resonances [18].

In 2006 Chen [16] proposed an active metamaterial device consisting of an array of gold electric resonator elements fabricated on a semiconductor substrate, together forming a Schottky diode (Fig. 2.4). This enables modulation of THz transmission by 50 percent by changing the gate voltage bias.

Tunable devices have also been made that use temperature change to affect transmission. In 2009 Xiao *et al* [17] demonstrated a device that

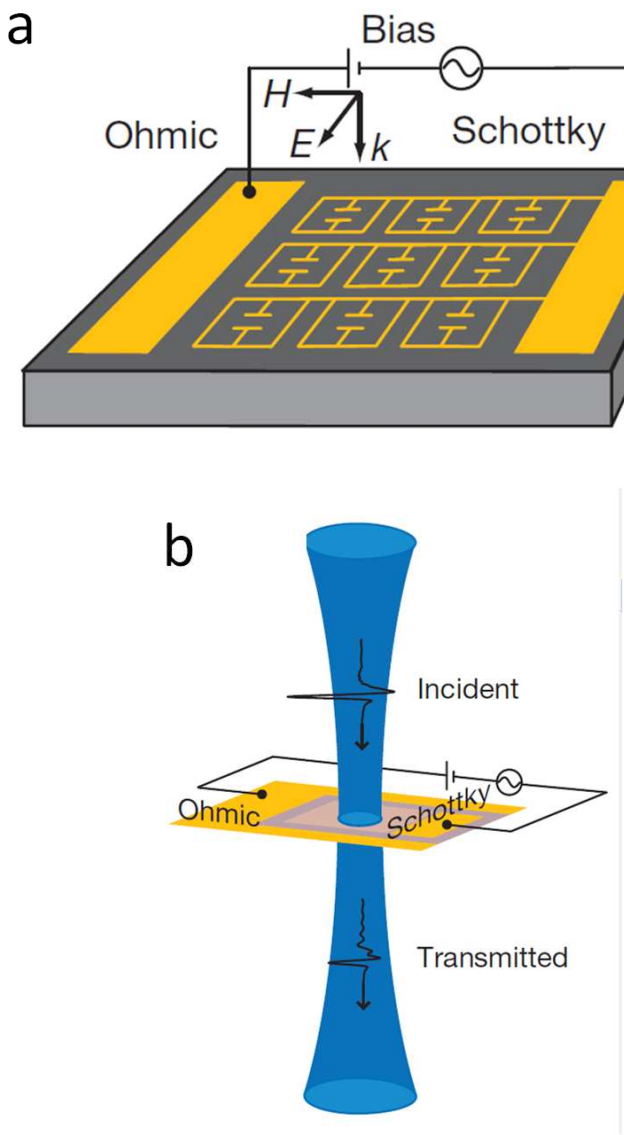

Figure 2.4: This active metamaterial functions as a Schottky diode [16]. Changing the bias at the gate affects the transmission characteristics. a)The unit cells are patterned with a period of 50 μm forming a planar array of 5 x 5 mm^2. These elements are connected together and function as a Schottky gate. A voltage bias applied between the Schottky and homic contacts changes the charge carrier density in the substrate near the split gaps, thus tuning the strength of the resonance. b) Experimental configuration for THz transmission measurements.

incorporated nematic liquid crystals. Using a glass substrate a series of coupled nanostrips was fabricated from layers of silver and alumina forming a trapezoid cross section (see Fig. 2.5). These strips were then coated with a liquid crystal layer of C_18H_19N (5CB) followed by a layer of PMMA and a top layer of glass. The refractive index of the 5CB was altered via phase transitions that occur as the ambient temperature is changed. By changing the temperature from 20° to 50° the transmission resonance shifted from 650 to 632 nm.

High temperature superconducting materials have also been used to tune transmission characteristics using temperature change. In 2010 Chen *et al* [60] demonstrated a plasmonic device using an array of split-ring resonators made of $YBa_2Cu_3O_{7-\delta}$ (YCBO) films with δ=0.5. As the temperature was changed from 82K to 20K, sharper resonances were observed beginning at around 0.25 THz at 82K and reaching a maximum absorption at round 0.48 THz at 20K.

Tunable devices that depend on the polarisation of the incident beam have also been explored. As previously mentioned, polarisation dependence has been demonstrated in arrays of elliptical holes [46]. These holes had major and minor axes of dimension 500 nm and 250 nm respectively and their major axis was oriented at 45° relative to the y-axis (see Fig. 2.6). In this research the polarisation effect was primarily a single transmission wavelength around 675 nm, the amount of light transmitted at this wavelength was dependent on polarisation of the incident beam.

Another method for achieving tunability is to use high-strain mechanical deformation of an elastomeric substrate. This method was demonstrated

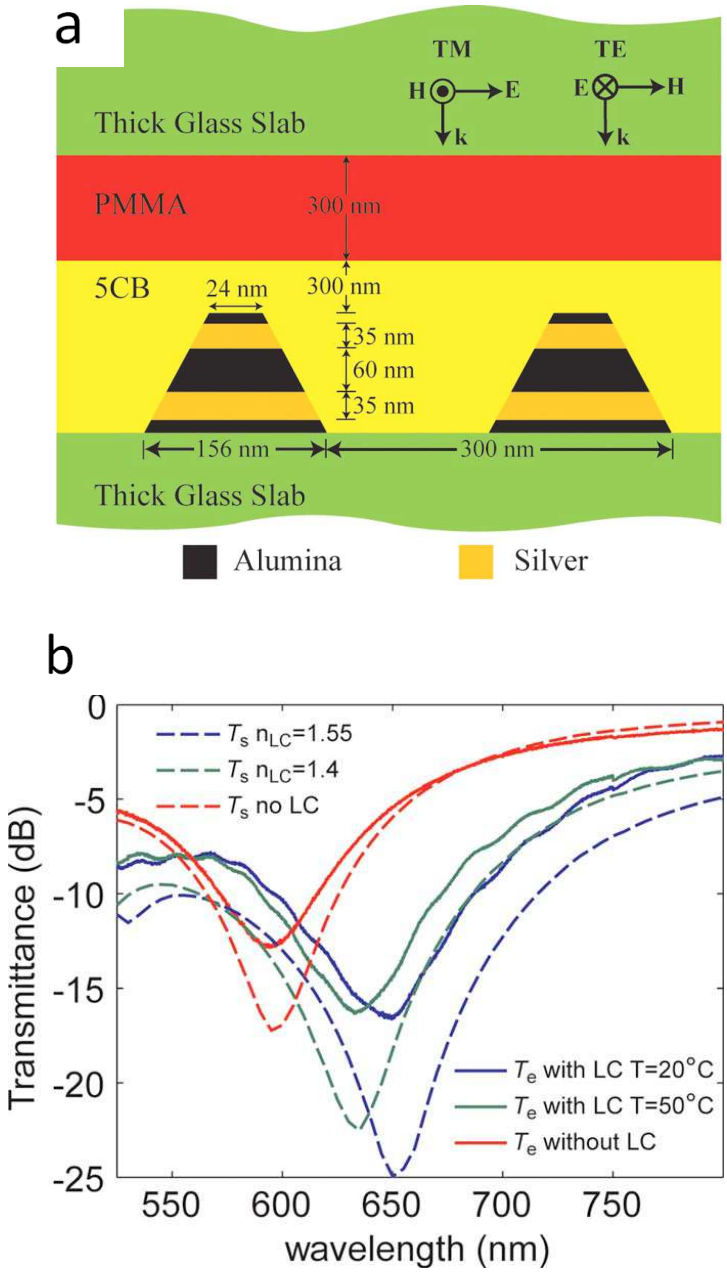

Figure 2.5: Image taken from Xiao *et al* [17]. A tunable liquid-crystal device. a) Cross section of the structure of the nanostrip sample. b) Transmission data with solid lines representing experimental data and dotted lines representing simulation data. As the temperature decreases the transmission minima lowers and is red shifted.

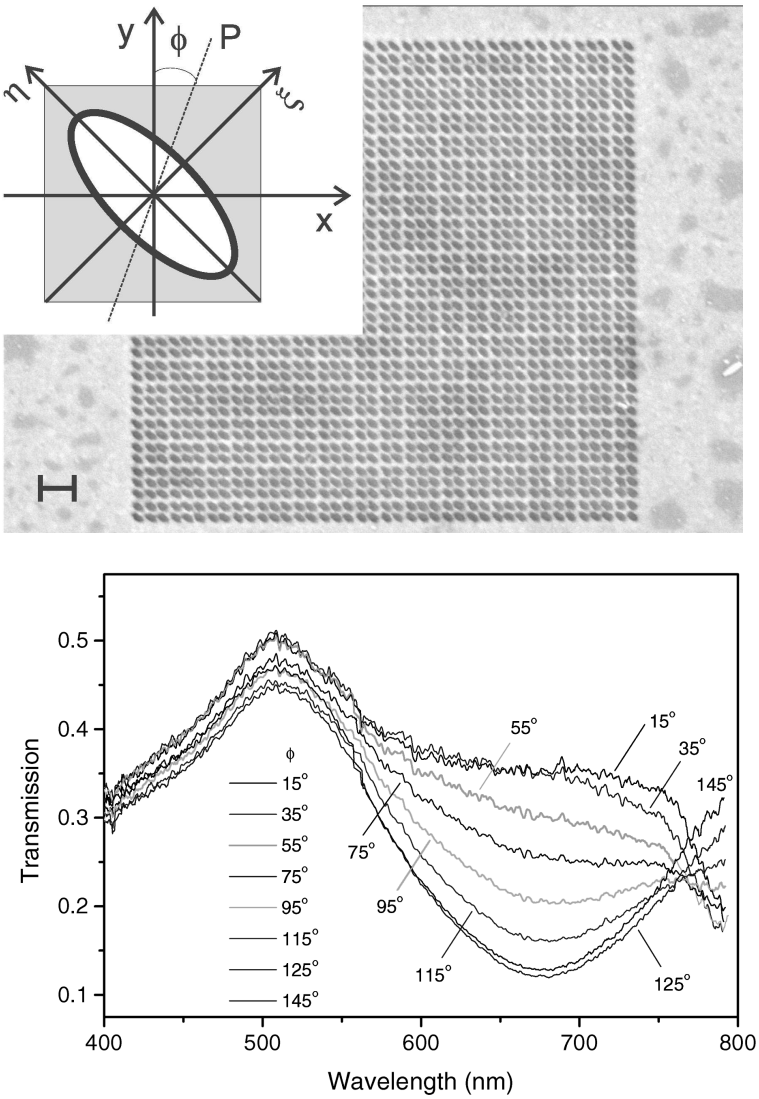

Figure 2.6: Image taken from Elliot *et al* [46]. a) An array of elliptical apertures with an inset showing a schematic of the unit cell and the angle of polarisation of the incoming E-field relative to the y-axis . b) Normal incidence transmission spectra for different polarisations of the incident light.

in 2010 by Pryce *et al* [18]. Using high-strain mechanical deformation of an elastomeric substrate the distances between the resonator elements was increased and thus the coupling strength between pairs of resonator elements was changed (Fig. 2.12). This technique enabled the tuning of transmission in the near infrared.

2.5 Cruciform Aperture Arrays

In 2007 Panoiu *et al* [61] demonstrated theoretically that arrays of asymmetric cruciform apertures display a polarisation dependence that could be tuned to different wavelengths by adjusting the length of the cruciform aperture arms. An example of the unit cell used in these arrays is shown in Fig. 2.8 a. The width of the cross gaps was $g_x = 40$ nm and $g_y = 20$nm, and the lengths of the arms was $L_x = 390$nm and $L_y = 370$nm. The periodicity in both the x and y directions was $\Lambda = 600$ nm.

Simulations were carried out using RSoft DiffractMOD software, which implements the rigorous coupled-wave analysis method. These simulations were carried out for an SiO_2 substrate with a 100 nm thick Au layer. The results showed that two transmission peaks occurred due to LSP resonances at $\lambda = 1.56$ μm and $\lambda = 2.07$ μm (Fig. 2.8 a) and that there existed a wavelength between these two peaks at which transmission intensity was invariant, referred to as the isosbestic point (a term taken from physical chemistry).

These simulations showed that sharp transmission peaks also existed for propagating plasmon resonances (Fig. 2.8 b). However, only those peaks

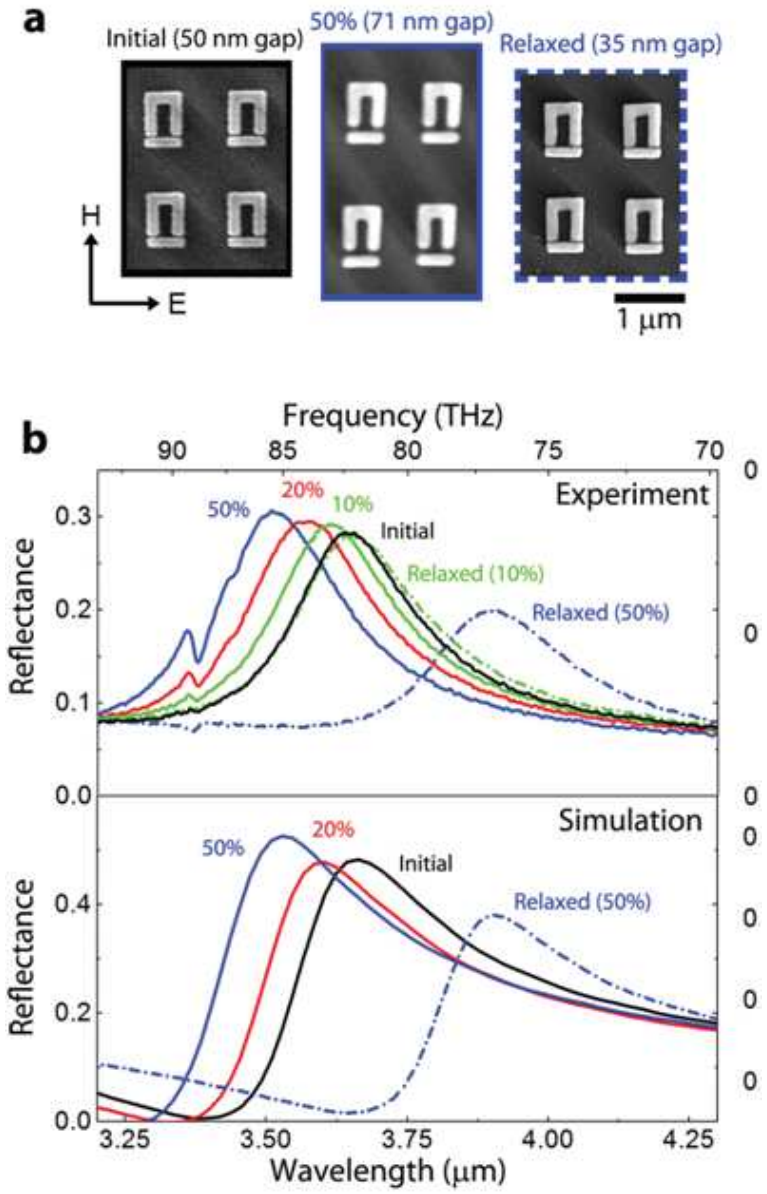

Figure 2.7: Image taken from Pryce *et al* [18]. a) Arrays of nanoscale resonators before, during and after an imposed strain. b) Transmission characteristics for the arrays different percentages of strain show a change in transmission wavelength.

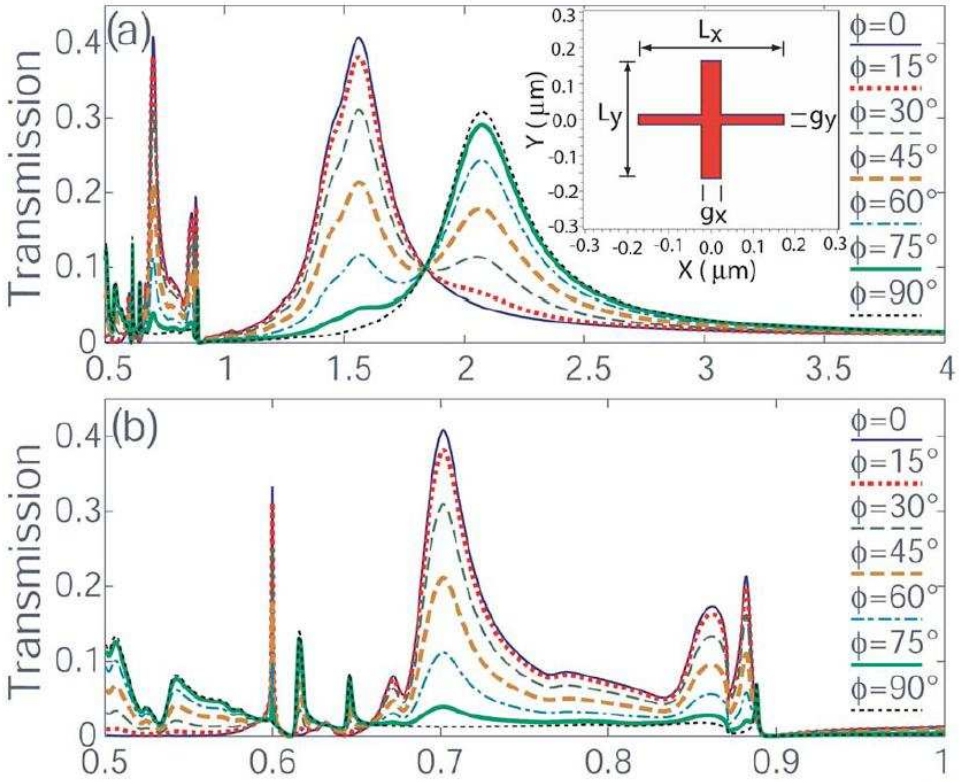

Figure 2.8: Image taken from Panoiu *et al* [61]. Transmission simulations for asymmetric cruciform apertures. The peaks in (a) occur at λ=1.56μm and λ=2.07μm and are a result of figure in the horizontal and vertical arms of the asymmetric cruciform apertures. The peaks in (b) are a consequence of extended surface plasmon resonances.

resulting from LSPs display a transmission wavelength that is dependent on polarisation. These figures also show minima at λ =615 nm and 870 nm, which are the result of the Wood's anomaly [62, 63]. This phenomenon occurs in diffraction gratings when a diffracted order becomes tangent to the plane of the grating.

In 2009, Lin *et al* [64] examined the transmission characteristics of symmetric cruciform apertures. Arrays of such apertures were fabricated by using FIB to mill a 140 nm thick layer of Au that had been deposited on a glass (BK7) substrate. Three arrays were fabricated with nominal arm lengths 250 nm, 300 nm and 350 nm respectively, each having the same lattice constant of Λ = 600 nm. They demonstrated that all three arrays had a minimum occurring at the predicted SPP resonance around 980 to 986 nm. For each array transmission peaks were also observed at wavelengths longer than 986 nm. The wavelengths of these resonances were shortest for the array with the shortest arm length and longest for the array with the longest arm length. These resonances were associated with the fundamental TE_{10}-like mode, which is an LSP resonance of the cruciform aperture. In 2010, Lin et al [69] further investigated the transmission characteristics of arrays of cruciform apertures by examining the effect of changing the angle of incidence of the IR beam. Arrays of cruciform apertures were fabricated in a Ag film deposited on a BK7 substrate. These arrays were mounted on a rotation stage and the angle of incidence was changed from θ =0 $^\circ$ to θ = 50° in 5° increments (see Fig 2.9). It was found that for TE modes the wavelengths of the resonance peaks remained unchanged, but for TM modes the peaks are redshifted for angles greater than 20° (see Fig 2.10).

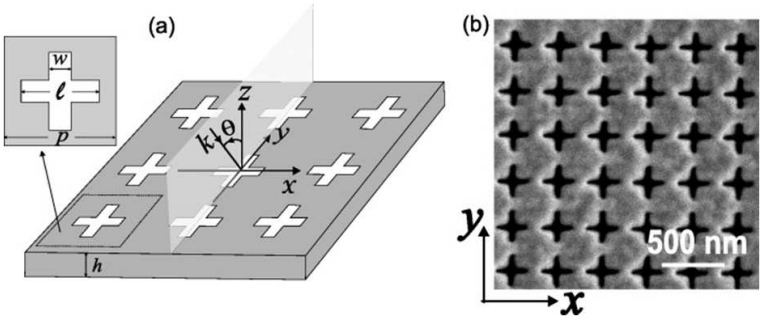

Figure 2.9: Image taken from Lin *et al* [69]. (a) A schematic of the structure used to test the effects of changing the angle of the incident transmission; (b) a SEM image of the fabricated aperture arrays. The structure was illuminated using a linearly polarized broadband light source and the transmitted light was recorded using a fiber optical spectrometer.

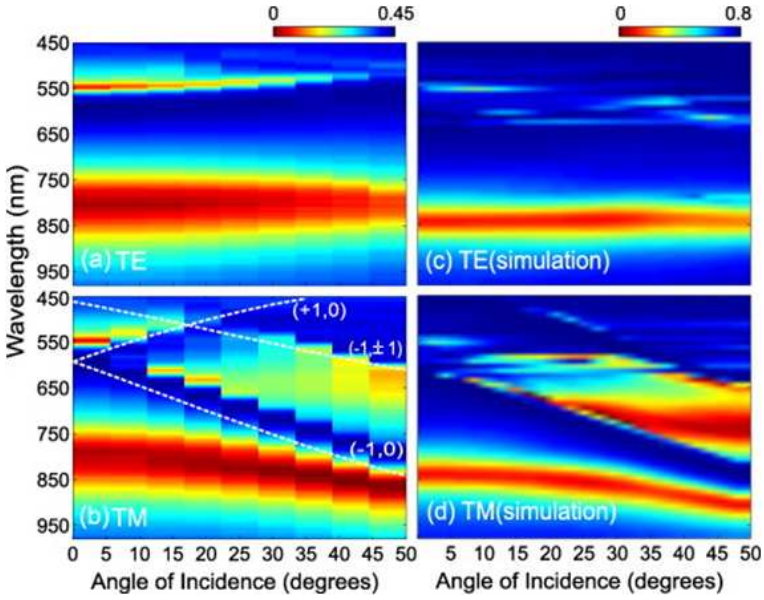

Figure 2.10: Image taken from Lin *et al* [69]. Angle-dependent light transmission through an array of cruciform apertures. (a) Measurement results for TE illumination; (b) measurement results for TM illumination; (c) simulation results for TE illumination; (d) simulation results for TM illumination. The white dotted lines shown in (b) are calculated dispersion curves of SPPs on Ag/glass interface.

2.6 Applications of EOT Devices

2.6.1 Biosensors

Many applications have been proposed for EOT devices and one of the most promising is the exploitation of this phenomenon in biosensors. Surface plasmons are highly sensitive to any change of the refractive index around the interface of metallic and dielectric materials. Such changes can occur as a consequence of adsorption of biomolecules to the metal surface. This phenomenon has been extensively explored to probe chemical and biochemical interactions. Plasmonic sensors could have many potential applications such as in medical diagnostics, biotechnology, drug screening, security, environmental protection and food safety. Many nonplasmonic sensors employ fluorescent labels that indicate the binding of a ligand to a receptor. Such fluorescent labels can interfere with the molecular interaction resulting in a change in the binding properties and thus obscuring the results. The main advantage of plasmonic sensing is that it dispenses with the need for fluorescent labels.

Such arrays can be tailored to provide sensitivity to particular target molecules. In 2004 Brolo *et al* [70] fabricated an array of subwavelength holes using focused ion beam. The holes had a diameter of around 200 nm and a periodicity of 590 nm (see Fig. 2.11). Transmission spectra were obtained for the bare holes and the arrays were then immersed in a 2 mM ethanoic solution of 11-mercaptoundecanoic acid (MUA). Spectra were once more taken and a redshift in transmission peak was observed. The MUA coated surface was then immersed in bovine serum albumin (BSA) and further spectra were

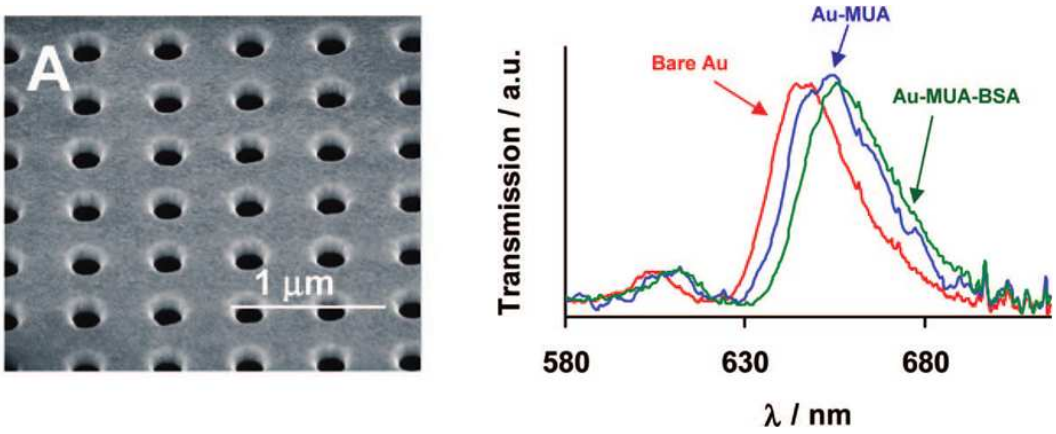

Figure 2.11: Image taken from Brolo *et al* [70]. A sensor based on extraordinary transmission. a)A micrograph of an array of circular apertures in a gold film to be used as a sensor. b) Transmission spectra are obtained for the bare gold film and also for the addition of MUA to the films surface and then the further addition of BSA. These two additional spectra show a redshift in transmission wavelength and thus can be used to detect whether MUA and BSA are present.

obtained. A further redshift was observed. The surface was then cleaned of the MUA and BSA and another spectrum was obtained, the results of which coincided with the spectra obtained at the beginning of the experiment for bare holes.

In 2009 Yang *et al* [8] demonstrated multiplexed biosensing in plasmonic arrays. Within an area of 65 μm x 50 μm 25 arrays were fabricated that provided real-time information on the local surface environment. These arrays, each with slightly different hole diameters, were included within a microfluidic device (Fig. 2.12). The different hole diameters transmit different wavelengths and are therefore sensitive to different changes in refractive index caused by molecules on the surface of the array, thus allowing for simultaneous detection of a wide range of molecules.

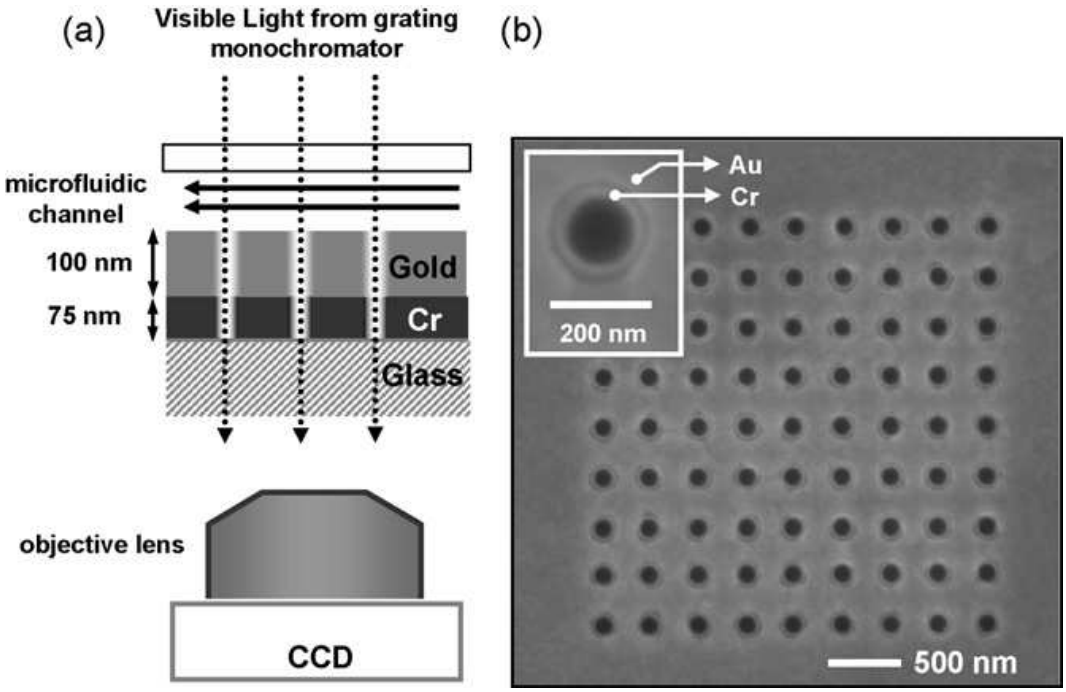

Figure 2.12: Image taken from Yang *et al.* Multiplexed biosensor [8]. a) Schematic of the arrangement of a nanohole sensor array and experimental set up. b) SEM micrograph of the 9 x 9 hole array.

2.6.2 Other Applications of Surface Plasmons

A wide range of applications have been suggested or demonstrated for devices exploiting the behaviour of surface plasmons. These include second harmonic generation, colour sorting, enhanced fluorescence spectroscopy, beaming, enhance light-matter interaction, the Purcell effect and nanolasers. These applications will be further outlined here.

In 2002 Lezec *et al* ([65] demonstrated plasmonic lensing using a subwavelength aperture milled using focused ion beam through a 300-nm-thick free standing Ag film (see Fig 2.13). Rings of concentric grooves were also milled on both input and exit sides with focused ion beam. The apertures were 300 nm thick and the wavelength range used to examine the transmission was 400-900 nm. With the incident beam at normal incidence a transmission peak is observed around 660 nm. By recording the transmission spectra at various angles on the exit side a strong angular dependence was observed.

Subwavelength plasmonic aperture devices can also be fabricated that operate as plasmonic lenses for Fresnel-region focusing [15] (see Fig 2.14). Lin *et al* fabricated two dimensional lenses that consisted of spatially varying cross-shaped apertures in a metallic film. Lensing is achieved by the combination of localised surface plasmon resonances within the apertures combined with an aperture geometry dependent phase shift. Similar compact plasmonic devices have been fabricated that operate as plasmonic wave plates, mirrors, and waveguides [73, 74, 75]

Second-harmonic generation (SHG) is a process in which photons enter a nonlinear material where the energy of two photons is combined resulting in

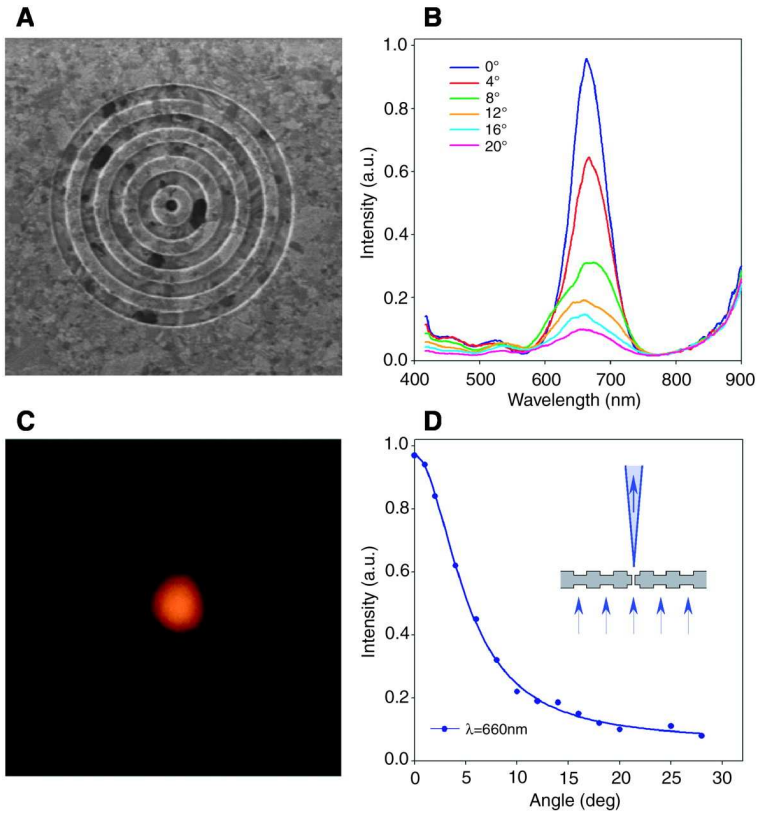

Figure 2.13: From Lezec *et al* [65].(A) FIB micrograph image of a bull's eye structure surrounding a cylindrical hole in a suspended Ag film (groove periodicity, 500 nm; groove depth, 60 nm; hole diameter, 250 nm; film thickness, 300 nm). (B) Transmission spectra recorded at various collection angles for a bull's eye structure on both sides of a suspended Ag film (groove periodicity, 600 nm; groove depth, 60 nm; hole diameter, 300nm; film thickness, 300 nm). (C) Optical image of the sample of (A) illuminated from the back at its wavelength of peak transmission (λ max = 660 nm) using a 50-nm bandpass filter. (D) Angular transmission-intensity distribution derived from the spectra of (B) at λ max. (Inset) Schematic diagram of the structure and the beam divergence and directionality of the transmitted light at λmax in the far field.

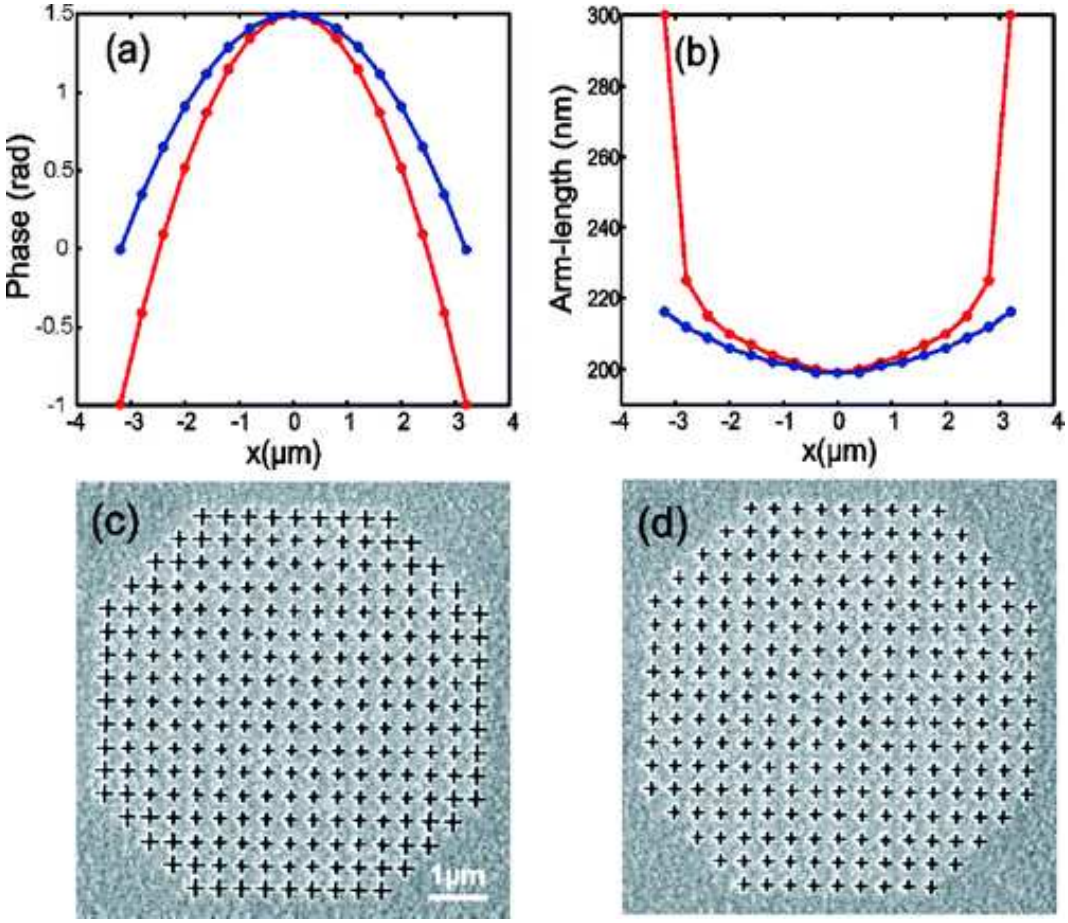

Figure 2.14: From Lin *et al* [15]. (a) The calculated phase and (b) arm length along one of the symmetric axes (x axis) of the 2-D aperture array lenses operating at 850 nm wavelength: red line, fd = 15 ?m; blue line, fd = 25 ?m. (c) and (d) SEM images of the fabricated devices with fd = 15 ?m and fd = 25 ?m, respectively.

new photons with twice the energy and thus double the frequency and half the wavelength. Enhanced second harmonic generation using GaAs embedded in plasmonic arrays was demonstrated in 2006 [71]. GaAs has a large second-order nonlinear susceptibility which means that given a sufficiently intense beam of light, it is possible to achieve frequency doubling. The researchers fabricated an array of pillars made of GaAs on a GaAs substrate. These pillars were surrounded in a layer of Au, the thickness of which matched the height of the pillars. Another similar array was fabricated with the same periodicity as the GaAs array but without the GaAs pillars, thus resulting in an Au hole array on a GaAs substrate. The transmission characteristics of these arrays were obtained and the results showed a fundamental transmission wavelength at around 3.2 μm and also the expected SHG wavelength at around 1.6μm (see Fig 2.15). However, there was a 10 fold increase in SHG in the array that included GaAs pillars. This occurs as a consequence of the enhanced electromagnetic field inside the hole apertures. Second-harmonic generation has applications in the laser industry, which uses this phenomenon to generate green 532 nm light from 1064 nm lasers.

In 2008, Ebbeson *et al* [72] produced a device that was able to sort photons of various different colours illuminating a nanostructured metal film, by combining the science of nanoholes with colour-specific surface-plasmon generation (see Fig 2.16). By patterning metal surfaces with nanometre scale structures this enables incoming light to be converted to surface plasmons. These can then be separated according to wavelength and polarisation, before being recoupled to light through subwavelength apertures. This photon-sorting capability provides a new approach for spectral and

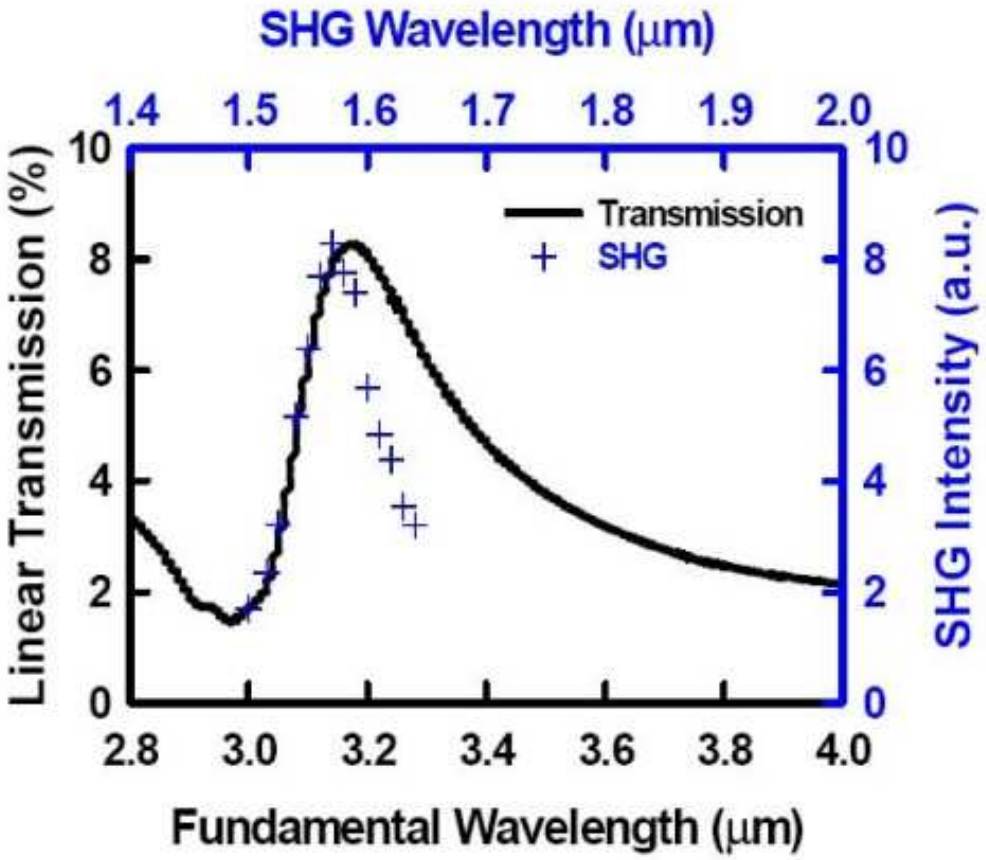

Figure 2.15: From Fan *et al* [71]. Embedding GaAs within plasmonic arrays results in a 10 fold increase in second-harmonic generation.

polarimetric imaging with extremely compact device architectures.

Another application for surface plasmons is nanoscale lasers (see Fig 2.17). Zhang et al [66] showed that it is possible to fabricate lasers that take advantage of the properties of surface plasmons to make a laser with dimensions on below that of the diffraction limit. These lasers used a hybrid plasmonic waveguide consisting of a high-gain cadmium sulphide semiconductor nanowire, separated from a silver surface by a nanometre scale MgF_2 insulating layer. Such laser have possible applications in biosensing, photonic circuits and quantum information technology.

Surface plasmons have also been used to enhance fluorescence spectroscopy such as in the work carried out by Stengel and Knoll [67] on primer extension reactions. The technique used here was Surface plasmon field-enhanced fluorescence spectroscopy in which plasmons were used to excite chromophors. This technique provides a channel for the read-out of fluorescence changes. This allows for the detection limit for low mass compounds, whose adsorption is only accompanied by small refractive index changes, to be substantially improved by fluorescent labeling.

The Purcell effect can also be enhanced by the application of surface plasmons. The Purcell effect is the enhanced spontaneous emission rates that occur when accompanied by a resonant cavity.

For example, Canneson *et al* [68] demonstrated that the coupling, at room temperature, between thick-shell CdSe/CdS nanocrystals coupled to localised surface plasmons produced optical modes confined at the nanoscale resulting in a strongly enhanced emission rate.

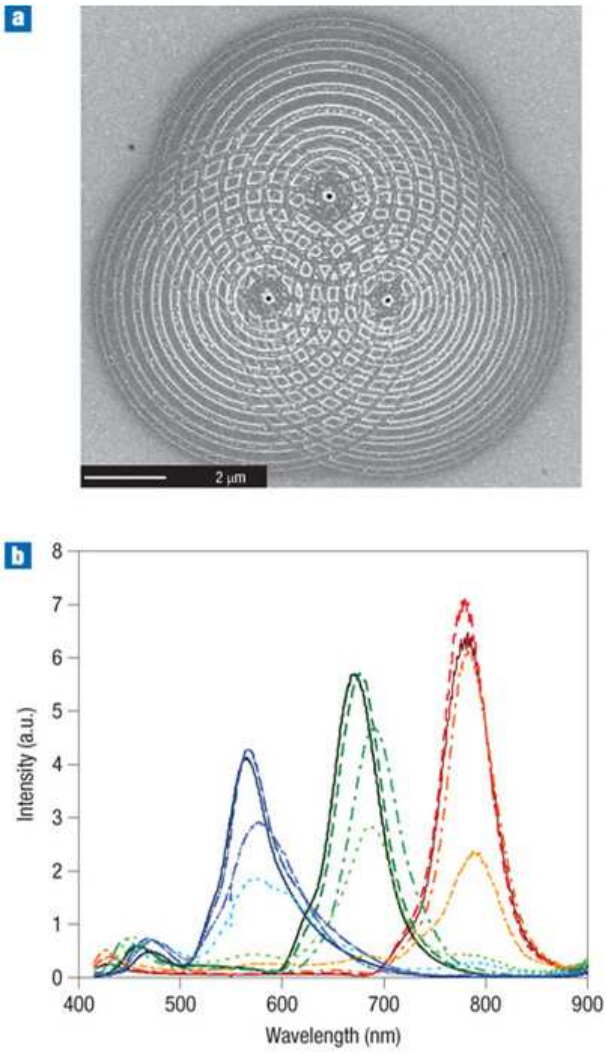

Figure 2.16: **a**, Triple bull's eye structures milled by FIB in a 300-nm-thick Ag film on a glass substrate. Dimensions: central hole diameter d = 170 nm, with circular grooves of 150 nm width,with depths varying linearly from 150 nm (central ring) to 10 nm (outer ring).Top structure: seven grooves of period 730 nm; left structure: eight grooves of period 630 nm; right structure: ten grooves of period 530 nm. **b**, Transmission spectra measured at each hole as a function of structural overlap. Bold lines 3 correspond to separated bull's eye structures. Dashed lines correspond to an overlap of 44, dasheddotted to 77 overlap and dotted lines to 88 overlap.

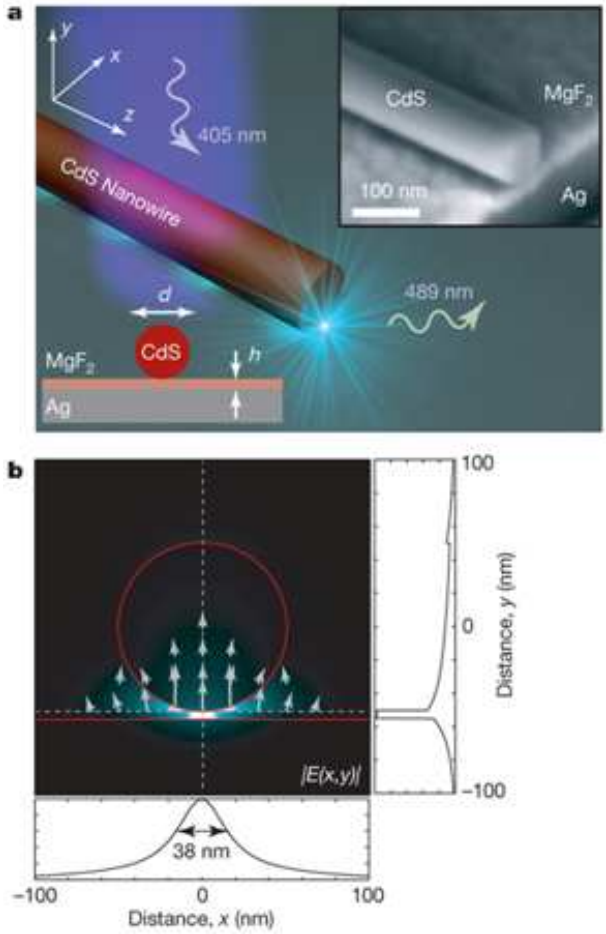

Figure 2.17: Imgage taken from Zhang et al ([66] a) The plasmonic laser consists of a CdS semiconductor nanowire on top of a silver substrate, separated by a nanometre-scale MgF2 layer of thickness h. The inset shows a scanning electron microscope image of a slice through the laser. b) The stimulated electric field distribution and direction —E(x, y)— of a hybrid plasmonic mode at a wavelength of = 489 nm. The cross-sectional field plots (along the broken lines in the field map) illustrate the strong overall confinement in the gap region between the nanowire and metal surface with sufficient modal overlap in the semiconductor to facilitate gain.

Chapter 3

Theoretical Background

3.1 Surface Plasmons

For all of the phenomena previously discussed, the underlying processes can be understood in light of the Drude model and the theory of surface plasmon polaritons. EOT is a consequence of the electric field of the incident electromagnetic wave interacting with surface electrons resulting in surface plasmon polaritons. Although the theory that describes this interaction is still under development, much research has been carried out to clarify the nature of these interactions. The first fully three-dimensional study of this phenomenon was described by Martín-Moreno *et al* in 2000 [7] for a metal film with a periodic array of square holes. The phenomena associated with SPPs have led to many applications, including surface-enhanced Raman excitation spectroscopy [78, 79, 80], metallic nanotips for near-field optical microscopy [81, 82, 83], chemical and biosensing [84, 85, 86, 87], and optical nanoantennae [88, 89, 90].

Surface plasmons are quasi-particles and may be defined as "quanta of surface-charge-density oscillations" [76]. In general surface plasmons can occur in two forms: extended surface plasmons, which are propagating surface modes; and localised surface plasmons, which are non-propagating modes and are the result of bounded geometries.

3.1.1 Propagating Surface Plasmons

In metals the plasma of free electrons can be displaced by an electric field, such as that of an incident photon, thus inducing quantised oscillations in the plasma. Since these surface charge oscillations couple to electromagnetic

waves and have a polarisation they are, at the interface of a metal and a dielectric, referred to as plasmon polaritons [38].

The negative dielectric constant that can exist in metals results in the propagation of waves confined to the metal surface. At the interface of a metal and a dielectric there are bound solutions to the wave equation. For this to be the case, values of the k vector perpendicular to the interface must be imaginary, ie. the wave must decay exponentially thus preventing radiation away from the interface. In the case of a flat metal surface, in order to produce surface plasmons the E-field must have a component that is perpendicular to the metal surface. As this component oscillates, it alternately draws and repels electrons to and from the surface. Since s-polarised (TE) waves have an electric field component that is only tangential to the interface, they do not contribute to the production of surface plasmons and therefore we need consider only p-polarised (TM) waves (see Fig. 3.1). A solution requires that boundary conditions are satisfied at the interface (see Fig. 3.2). The following solution is valid for for the dielectric function of the metal, ϵ_m, when it is either real or has a complex value, i.e. for cases without and with attenuation. The dielectric function of the dielectric is considered to be real and positive.

If we consider a wave whose plane of incidence is entirely within a plane defined by the z axis and y=0, then the boundary conditions require that

$$k_{m,x} = k_{d,x} = k_x \tag{3.1}$$

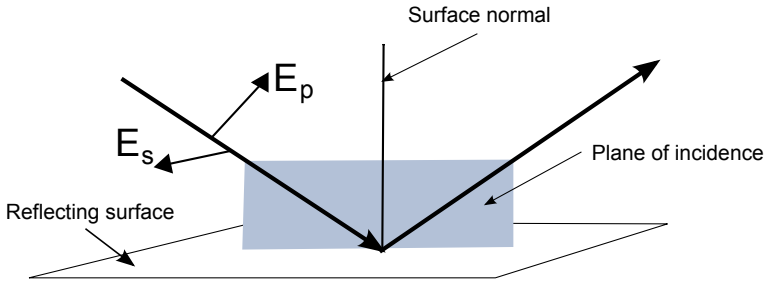

Figure 3.1: P-polarised waves have a component of their electric field perpendicular to the plane of incidence and hence, as the electric field oscillates, alternately draw and repel electrons to and from the surface. The electric field of s-polarised waves, however, is entirely tangential to the reflecting surface and so have no perpendicular component. Therefore they do not contribute toward the production of surface plasmons.

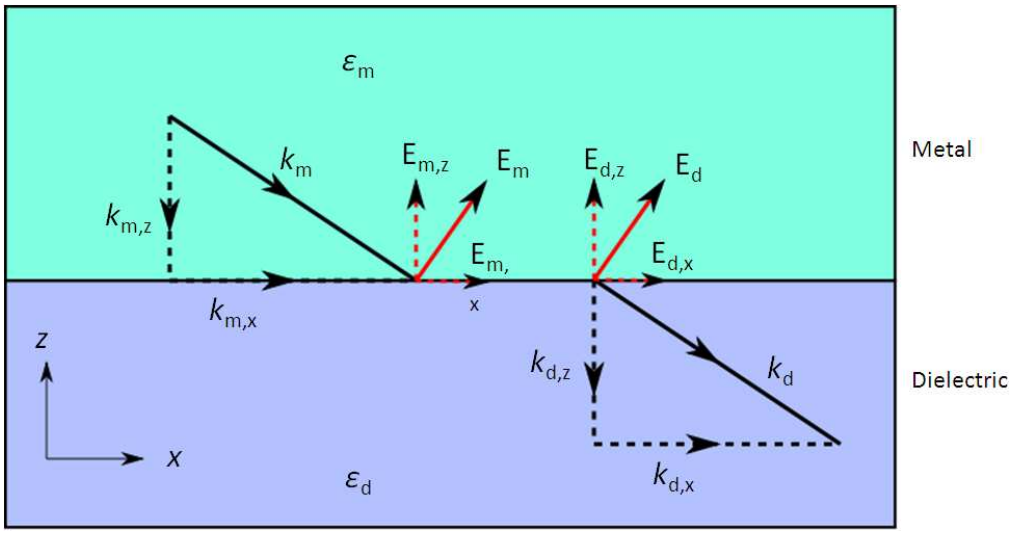

Figure 3.2: The k and E vectors for the incident and transmitted waves for a wave whose plane of incidence is defined by the z axis and y = 0.

$$E_{m,x} = E_{d,x} \tag{3.2}$$

and

$$\epsilon_m E_{m,z} = \epsilon_d E_{d,z} \tag{3.3}$$

The wave vectors can also be expressed in terms of two orthogonal components

$$k_x^2 + k_{m,z}^2 = k_0^2 \epsilon_m \tag{3.4}$$

$$k_x^2 + k_{d,z}^2 = k_0^2 \epsilon_d \tag{3.5}$$

where $k_{1,z}$ and $k_{2,z}$ represent the z components of the k vector for the incident and transmitted waves respectively, and $k_0 = 2\pi/\lambda$, where λ is the vacuum wavelength. It is also the case that the displacement field in both materials must be source free [76], therefore $\nabla \cdot \mathbf{D} = 0$. Thus,

$$-\frac{E_{m,z}}{E_{m,x}} = \frac{k_{m,x}}{k_{m,z}} \tag{3.6}$$

$$-\frac{E_{d,z}}{E_{d,x}} = \frac{k_{d,x}}{k_{d,z}} \tag{3.7}$$

combining 3.3, 3.6 and 3.7 gives

$$-\epsilon_m \frac{k_{m,x}}{k_{m,z}} E_{m,x} = -\epsilon_d \frac{k_{d,x}}{k_{d,z}} E_{d,x} \tag{3.8}$$

However, given the equalities expressed in equations 3.1 and 3.2, equation

3.8 simplifies to

$$\epsilon_m k_{d,z} - \epsilon_d k_{m,z} = 0 \tag{3.9}$$

using 3.4 and 3.5 we can replace the k_z values, which gives

$$\epsilon_m[\epsilon_d k_0^2 - k_x^2]^{1/2} - \epsilon_d[\epsilon_m k_0^2 - k_x^2]^{1/2} = 0 \tag{3.10}$$

This can be rearranged to form a dispersion relationship between the wavevector in the direction of propagation and the angular frequency ω

$$k_x^2 = k_0^2 \frac{\epsilon_m \epsilon_d}{\epsilon_m + \epsilon_d} = \frac{\omega^2}{c^2} \frac{\epsilon_m \epsilon_d}{\epsilon_m + \epsilon_d} \tag{3.11}$$

Combining 3.4 and 3.5 and inserting into 3.9 gives the normal components of the wavevector

$$k_{j,z}^2 = k_0^2 \frac{\epsilon_j^2}{\epsilon_m + \epsilon_d}, \qquad j = m, d \tag{3.12}$$

From the Drude model we can take

$$\epsilon = 1 - \frac{\omega_p^2}{\omega^2 + i\Gamma\omega} \tag{3.13}$$

and combine it with equation 3.11 to obtain:

$$\omega_{sp} = \frac{\omega_p}{\sqrt{1 + \epsilon_d}} \tag{3.14}$$

which is the characteristic surface plasmon frequency

For an interface mode to exist, k_x^2 must be real, while, for a bound solu-

tion, the normal components must be purely imaginary. Looking at equation 3.11 the former can be satisfied if the sum and product of the dielectric functions are either both positive or both negative. From equation 3.12, the latter can be satisfied if the sum in the denominator is negative. Thus

$$\epsilon_m(\omega)\epsilon_d(\omega) < 0 \tag{3.15}$$

$$\epsilon_m(\omega) + \epsilon_d(\omega) < 0 \tag{3.16}$$

This requires that one of the dielectric functions must be negative, with a modulus that exceeds that of the other dielectric function. Metals such as gold and silver have a large negative real part of the dielectric function and a small imaginary part. Therefore at the interface of a noble metal with a dielectric such as CaF_2, silicon or air localised modes can exist.

To obtain the dispersion relation we assume that ϵ_d is real and positive and is independent of ω (Fig. 3.3). This is the case for air where ϵ_d=1. Thus

$$\omega_{sp} - \frac{\omega_p}{\sqrt{2}} \tag{3.17}$$

The dispersion relation clearly shows that the wavevector k_x for surface plasmons is always larger than the wavevector of light in free space. Therefore, in order to excite surface plasmons it is necessary to increase the wavevector of the exciting light above its free space value. One way that this phase matching can be achieved is with a grating, which may consist of an series of holes or grooves with lattice constant Λ (Fig. 3.5). Phase matching is possible when the momentum of the plasmons, k_x is equal to that of the

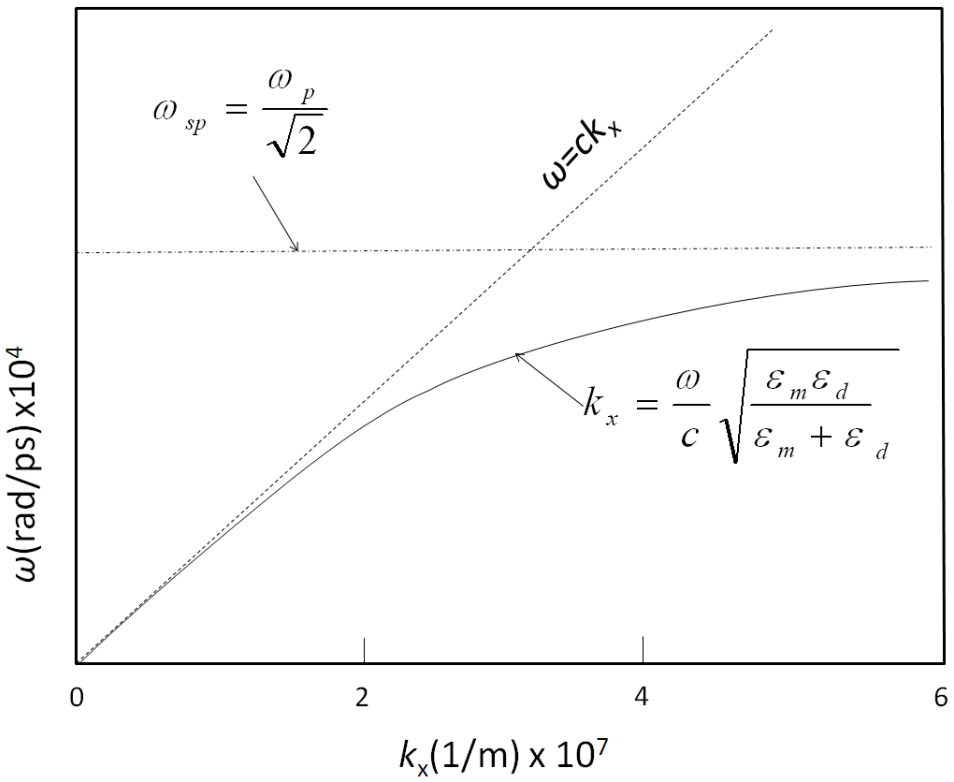

Figure 3.3: Image adapted from Novotny and Hecht [76]. This graph shows the dispersion relation for the interface between air and Au. The wavevector of the dispersion curve (k_x) is always larger than that of light in air (ω=ck_x). Therefore plasmons cannot directly be excited at a metal dielectric interface.

momentum of the in-plane component of the impinging photons, k_e. This occurs when $k_x = k \sin\theta \pm \nu g$, where $g = \frac{2\pi}{\Lambda}$ is the reciprocal lattice vector of the grating, and ν= (1,2,3...). It is clear from these equations that when the incident wave is normal to the surface it is still possible to excite plasmons.

3.1.2 Localised Surface Plasmons

Localised surface plasmon polaritons are nonpropagating and are bound to the surface of a particle or an aperture. These plasmons are responsible for a transmission peak that is directly related to the Bloch waves in the apertures [91], which are oscillations in a periodic potential. In contrast to extended surface plasmons on a smooth surface, LSPs can be resonantly excited with light of appropriate frequency without the requirement of phase matching the frequency and wavevector of the impinging source and the surface plasmon. Also, the incident beam can be normal to the array surface since the E field will be perpendicular to the walls of the aperture and can therefore excite plasmons at the interfaces between the metal and the dielectric in the aperture. For simple cases, such as a sphere shaped particle, if the wavelength of the LSP is larger than the characteristic size of the system (in the case of crosses, the unit cell), then the electrostatic approximation can be made. In such a case the phase of the electromagnetic field is approximately constant over the volume of the particle. LSPs occur only at frequencies smaller than a threshold frequency ω_{lsp} which can be determined in the electrostatic regime by solving the Laplace equations for an appropriate set of boundary conditions.

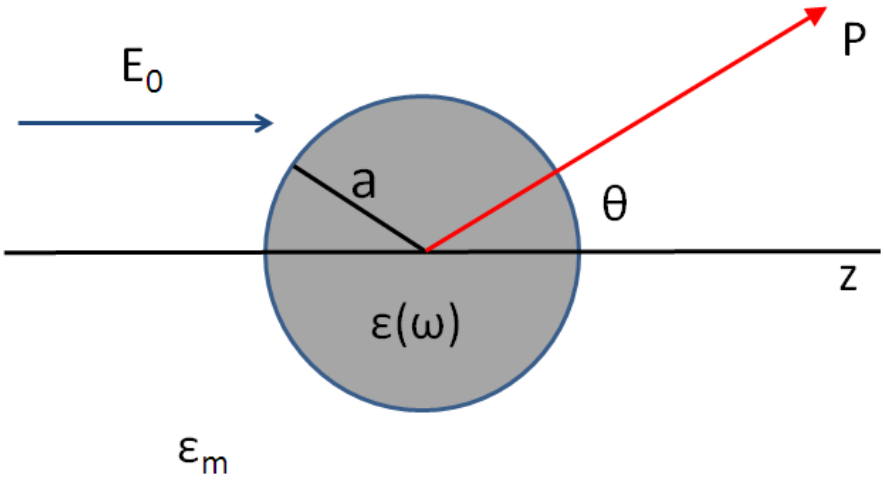

Figure 3.4: A representation of a homegenous sphere in an electrostatic field

As an example of how LSP resonances may be determined, it is useful to begin with a convenient geometry for analysis, namely that of a homogeneous sphere (see Fig. 3.4) [38]. This sphere has a radius a and is centred at the origin in a uniform static electric field defined by:

$$\boldsymbol{E} = E_0 \hat{z} \tag{3.18}$$

The medium surrounding the sphere is isotropic, non-absorbing and has a dielectric constant ϵ_m. The electric field lines run parallel to the z axis. The dielectric response of the sphere is $\epsilon(\omega)$.

First it is necessary to find a solution to the Laplace equation for the potential, $\nabla^2 V = 0$, which can then be used to calculate the electric field $E = -\nabla V$. The general solution of this problem takes the following form

$$(r, \theta) = \sum_{l=0}^{\infty} [A_r^l + B_l r^{-(l+1)}] P_l(\cos\theta) \tag{3.19}$$

where $P_l(\cos\theta)$ are the Legendre Polynomials of order l, and θ is the angle between the position vector $\hat{r}$ at a point P and the z-axis. The potentials must remain finite at the origin, which leads to the following two equations for the potential within the sphere, V_{in}, and the potential outside the sphere, V_{out}:

$$V_{in}(r,\theta) = \sum_{l=0}^{\infty} A_l r^l P_l(\cos\theta) \tag{3.20}$$

$$V_{out}(r,\theta) = \sum_{l=0}^{\infty} [B_l r^l + C_l r^{-(l+1)}] P_l(\cos\theta) \tag{3.21}$$

To determine the coefficients A_l, B_l and C_l, the boundary conditions require that $V = 0$ when $r = R$ and $V \to -E_0 r\cos\theta$ when $r \to \infty$. Therefore $B_1 = -E_0$ and $B_l = 0$ for $l \neq 1$.

To obtain the remaining coefficients, the boundary conditions at $r = a$ are required. At this boundary the tangential components of the electric field must be equal, such that

$$-\frac{1}{a}\frac{\partial V_{in}}{\partial\theta} = -\frac{1}{a}\frac{\partial V_{out}}{\partial\theta} \tag{3.22}$$

The normal components of the displacement field must also be equal

$$-\epsilon_0\epsilon\frac{\partial V_{in}}{\partial r} = -\epsilon_0\epsilon_m\frac{\partial V_{out}}{\partial r} \tag{3.23}$$

Using these boundary conditions the values for A and C are obtained: $A_l = C_l = 0$ for $l \neq 1$. When $l = 1$ the values of A_1 and C_1 can be used to describe the potentials such that

$$V_{in} = -\frac{3\epsilon_m}{\epsilon + 2\epsilon_m} E_0 r \cos\theta \tag{3.24}$$

$$V_{out} = -E_0 r \cos\theta + \frac{\epsilon - \epsilon_m}{\epsilon + 2\epsilon_m} E_0 a^3 \frac{\cos\theta}{r^2} \tag{3.25}$$

Examining equation 3.25 reveals that it describes the superposition of an applied field and a dipole which is located at the centre of the sphere. Rewriting 3.25 it is possible to introduce the dipole moment $\mathbf{p}$

$$V_{out} = -E_0 r \cos\theta + \frac{\mathbf{p.r}}{4\pi\epsilon_0\epsilon_m r^3} \tag{3.26}$$

$$\mathbf{p} = 4\pi\epsilon_0\epsilon_m a^3 \frac{\epsilon - \epsilon_m}{\epsilon + 2\epsilon_m} \mathbf{E}_0 \tag{3.27}$$

It is therefore clear that the application of the applied field results in a dipole moment within the sphere and that this is proportional to the modulus of $\mathbf{E}_0$. The polarisability, α, which is defined by

$$\mathbf{p} = \epsilon_0\epsilon_m \alpha \mathbf{E}_0 \tag{3.28}$$

can thus be expressed as

$$\alpha = 4\pi a^3 \frac{\epsilon - \epsilon_m}{\epsilon + 2\epsilon} \tag{3.29}$$

Examining this equation it is clear that there is a resonant enhancement in polarisability when $|\epsilon + 2\epsilon_m|$.

If the imaginary part of ϵ is small or is varying slowly around the resonance

this condition simplifies to

$$\mathrm{Re}[\epsilon(\omega)] = -2\epsilon_m \tag{3.30}$$

In the case of a lightly damped system following equation from the Drude model can be used to obtain the resonance condition:

$$\epsilon = 1 - \frac{\omega_p^2}{\omega^2} \tag{3.31}$$

which leads to

$$\omega_0 = \frac{\omega_p}{\sqrt{3}} \tag{3.32}$$

Rectangular wave guide

Other geometries require different treatments. In the case of rectangular apertures, for example, the resonances can be obtained by treating the aperture as a waveguide. Solutions are obtained using the Maxwell equations with appropriate boundary conditions. If we assume that the the wave guide is a perfect conductor then $\mathbf{E} = 0$ and $\mathbf{B} = 0$ within the boundary material [92]. Therefore the boundary conditions are:

$$E^{\parallel} = 0 \tag{3.33}$$

$$B^{\perp} = 0 \tag{3.34}$$

The free charges and currents induced on the surface will enforce these

conditions. The electric and magnetic fields must satisfy the Maxwell equations in the interior of the waveguide. Therefore waves propagating through the tube must satisfy both the boundary conditions and the Maxwell equations.

The resulting equations for E_z and B_z are

$$\left[\frac{\delta^2}{\delta x^2} + \frac{\delta^2}{\delta y^2} + (\omega/c)^2 - k^2\right] E_z = 0 \tag{3.35}$$

$$\left[\frac{\delta^2}{\delta x^2} + \frac{\delta^2}{\delta y^2} + (\omega/c)^2 - k^2\right] B_z = 0 \tag{3.36}$$

For TE waves (i.e. for $E_z = 0$) in a rectangular aperture height a and width b it is necessary to solve equation 3.36 subject to boundary condition 3.34.

This can be done by separation of variables such that

$$B_z(x, y) = X(x)Y(y) \tag{3.37}$$

which leads to

$$Y\frac{d^2X}{dx^2} + X\frac{d^2Y}{dy^2} + [(\omega/c)^2 - k^2]XY = 0 \tag{3.38}$$

Dividing by XY and also noting that the x and y terms must be constant we obtain

$$\frac{1}{X}\frac{d^2X}{dx^2} = -k_x^2 \tag{3.39}$$

$$\frac{1}{Y}\frac{d^2Y}{dy^2} = -k_y^2 \tag{3.40}$$

where

$$-k_x^2 - k_y^2 + (\omega/c)^2 - k^2 = 0 \tag{3.41}$$

The general solution for equation 3.39 is

$$X(x) = Asin(k_x x) + Bcos(k_x x) \tag{3.42}$$

The boundary conditions, however, require that B_x vanishes at $x = 0$ and $x = a$. Therefore $A = 0$ and

$$k_x = m\pi/a \tag{3.43}$$

where

$$m = 0, 1, 2, ... \tag{3.44}$$

Similarly for Y

$$k_y = m\pi/b \tag{3.45}$$

$$n = 0, 1, 2, ... \tag{3.46}$$

Thus

$$B_z = B_0 cos(m\pi x/a) cos(n\pi y/b) \tag{3.47}$$

By substituting 3.43 and 3.45 in 3.41 we obtain

$$k = \sqrt{(\omega/c)^2 = \pi^2[(m/a)^2 + (n/b)^2]} \tag{3.48}$$

and if

$$\omega c\pi \sqrt{(m/a)^2 + (n/b)^2]} \equiv \omega_{mn} \tag{3.49}$$

the wave number is then imaginary. In such a case the field is exponentially attenuated and ω_{mn} is referred to as the cutoff frequency. The lowest cutoff frequency is given by TE_{10} and is

$$\omega_{10} = c\pi/a \tag{3.50}$$

In terms of the wavenumber this is

$$k = \frac{1}{c}\sqrt{\omega^2 - \omega_{mn}^2} \tag{3.51}$$

Such that when the frequency is equal to the cutoff frequency the wavenumber is zero.

In waveguides at the cutoff frequency the interaction of the electric field at the surface of the conductor results in variable electric charge density, and thus localised surface plasmons.

3.2 The Effect of Ohmic Losses in the Metal

To accommodate ohmic losses due to electron scattering it is necessary to consider the imaginary part of the metal's dielectric function with the values of ϵ'_m and ϵ''_m being real. We also assume that the dielectric has negligible losses, and thus ϵ_d is real. Similarly there is a complex wavenumber

$$k_x = k'_x + ik''_x \tag{3.52}$$

The real part of this wavenumber, k'_x, determines the wavelength of the surface plasmon polariton, while the damping of the SPP as it propagates along the surface is accounted for by the imaginary part, k''_x. From equation 3.11, and assuming that the imaginary part of the metal's dielectric constant is much smaller than the real part ($|\epsilon''_m| \ll |\epsilon'_m|$), the real and imaginary parts of k_x can be determined.

$$k'_x \approx \sqrt{\frac{\epsilon'_m \epsilon_d}{\epsilon'_m + \epsilon_d}} \frac{\omega}{c} \tag{3.53}$$

$$k''_x \approx \sqrt{\frac{\epsilon'_m \epsilon_d}{\epsilon'_m + \epsilon_d}} \frac{\epsilon''_m \epsilon_d}{2\epsilon'_m(\epsilon'_m + \epsilon_d)} \frac{\omega}{c} \tag{3.54}$$

It follows that the SPP wavelength is

$$\lambda_{SPP} = \frac{2\pi}{k'_x} \approx \sqrt{\frac{\epsilon'_m + \epsilon_d}{\epsilon'_m \epsilon_d}} \lambda \tag{3.55}$$

where λ is the wavelength of the excitation light in vacuum.

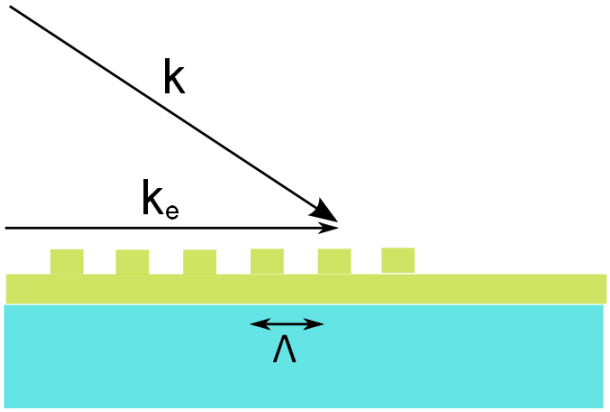

Figure 3.5: Gratings can be used to phase match the in-plane momentum k_e of the impinging photons on a metal surface with the momentum of the plasmons.

3.3 Rigorous Coupled-Wave Analysis Method

To simulate the transmission and reflection characteristics of the devices fabricated here, the rigorous coupled-wave analysis method [93, 94, 95] was employed using RSoft DiffractMod software. This method can be used to produce transmission amplitude data or of 2D layers showing field profiles in the x and y directions. It is commonly employed for modeling scattering from periodic structures and is a semi-analytical method, meaning that the wave equations are solved analytically in the longitudinal direction. It is rigorous in that it does not require approximations of the Maxwell equations. This approach was developed by Moharam and Gaylord [1986] for analyzing the electromagnetic characteristics of metallic surface-relief gratings. To find a solution, boundary conditions are obtained for the material interfaces by matching tangential electric and magnetic fields.

Moharam and Gaylord begin by defining the geometry of the grating they intend to analyze (Fig. 3.6) [96]. Region I is a lossless homogeneous dielectric

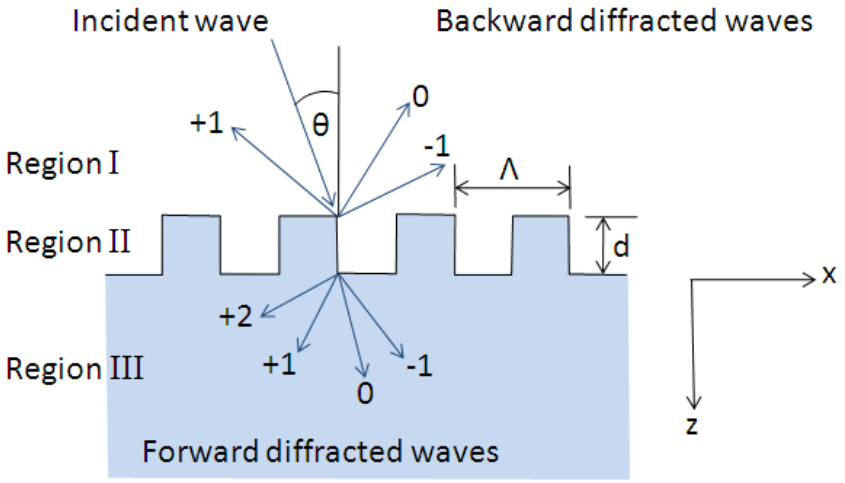

Figure 3.6: Geometry of the metallic grooved surface used in the rigorous coupled-wave analysis method.

with a relative permittivity of ϵ_I. Region III is a lossy homogeneous metal with a complex permittivity ϵ_{III}. Region II is a periodic structure consisting of both materials. The permittivity of this region may be expanded in a Fourier series,

$$\epsilon(x,z) = \epsilon(x+\Lambda,z) = \sum_p \epsilon_p(z) exp(jpgx) \tag{3.56}$$

where ϵ_p is the Fourier component of the grating permittivity, Λ is the periodicity of the grating, g is the magnitude of the grating reciprocal lattice vector ($g = \frac{2\pi}{\Lambda}$), and $j = (-1)^{\frac{1}{2}}$.

For simplicity the analysis provided here deals only with TE polarisation. The case for TM can be found at [97]. Since the total electric field in region I is the sum of the incident wave and the backward diffracted wave, the electric field in this region may be expressed as

$$E_I = exp[-j(k_{x0}x + k_{z0}z)] + \sum_i R_i exp[-j(k_{xi}x - k_{ziI}z] \tag{3.57}$$

where $k_{x0} = k\epsilon_I^{1/2}\sin\theta$, $k_{z0} = k\epsilon_I^{1/2}\cos\theta$, $k = 2\pi/\lambda$, θ is the angle of incidence, λ is the wavelength in free space, and R_i is the amplitude of the ith-order backward-diffracted wave. In addition, k_{xi}= $k_{x0} - ig$, a term often referred to as the Floquet condition [98]. In region I, the wave vectors of the backward-diffracted waves have magnitude $k_{iI} = k\epsilon_I^{1/2}$. It therefore follows that $k_{ziI} = (k^2\epsilon_I - k_{xi}^2)^{1/2}$.

In region III the E-field is

$$E_{III} = \sum_i T_i exp[-j[k_{xi}x + k_{ziIII}(z - d)]] \tag{3.58}$$

where, analogous to the case in region I, $k_{ziIII} = (k^2\epsilon_{III} - k_{xi}^2)^{1/2}$, T_i is the ith-order forward-diffracted wave, and d is the depth of the grating.

In region II, the electric field may be expressed as

$$E_{II} = \sum_i S_i(z) exp[-j(k_{xi}x + k_{z0}z)] \tag{3.59}$$

where $S_i(z)$ are the space-harmonic field amplitudes. For TE polarisation, the total field in region II satisfies the wave equation

$$\nabla^2 E_{II} + k^2\epsilon(x,z)E_{II} = 0 \tag{3.60}$$

Substituting $S_i(z)$ into this equation results in

$$\frac{d^2S_i(z)}{dz^2} - j2k_{z0}\frac{dS_i(z)}{dz} = (k_{xi}^2 + k_{x0}^2)S_i(z) - k^2\sum_p \epsilon_p(z)S_{i-p}(z) \qquad (3.61)$$

These are the coupled-wave equations and they form an infinite set of second-order differential equations which may be solved using a state-variables method from linear systems analysis [99].

In this case the state variables in region II are defined as follows:

$$S_{1,i}(z) = S_i(z) \qquad (3.62)$$

and

$$S_{2,i}(z) = dS_i(z)/dz \qquad (3.63)$$

This has the effect of transforming the infinite set of second-order equations into two infinites sets of first-order differential equations.

The state equation that results from this forms a matrix consisting of four submatrices, the elements of which are defined by equation 3.61. This may be expressed as

$$\dot{S} = AS \qquad (3.64)$$

where A is the total coefficient matrix and $\dot{S} = \frac{\delta S}{\delta z}$, and $\dot{S}$ and S are column vectors. A is an infinite matrix and so results must be found using a truncated matrix. This can be done by truncating each of the four submatrices into an n x n matrix. As the value of n increases the solution rapidly converges

to the exact result. The quantity n corresponds to the number of space harmonics employed and is a value that can be determined in the RSoft software. Equation [3.64] may therefore be written as

$$\begin{pmatrix} \vdots \\ \dot{S}_{1,-1} \\ \dot{S}_{1,0} \\ \dot{S}_{1,1} \\ \vdots \\ \dot{S}_{2,-1} \\ \dot{S}_{2,0} \\ \dot{S}_{2,1} \\ \vdots \end{pmatrix} = \begin{pmatrix} & & \vdots & & & & \vdots & & \\ & 0 & 0 & 0 & & 1 & 0 & 0 & \\ \cdots & 0 & 0 & 0 & \cdots & 0 & 1 & 0 & \cdots \\ & 0 & 0 & 0 & & 0 & 0 & 1 & \\ & & \vdots & & & & \vdots & & \\ & b_{-1} & a & 0 & & c_{-1} & 0 & 0 & \\ \cdots & a & b_0 & a & \cdots & 0 & c_0 & 0 & \cdots \\ & 0 & a & b_1 & & 0 & 0 & C_1 & \\ & & \vdots & & & & \vdots & & \end{pmatrix} \begin{pmatrix} \vdots \\ S_{1,-1} \\ S_{1,0} \\ S_{1,1} \\ \vdots \\ S_{2,-1} \\ S_{2,0} \\ S_{2,1} \\ \vdots \end{pmatrix}$$

where $a = -2\pi^2\epsilon_m/\lambda^2$, $b_i = 4\pi^2 i(i-m)/\Lambda^2$ and $c_i = j4\pi[(\epsilon_0)^{1/2}\cos\theta/\lambda - i\cos\phi/\Lambda]$. To find the solution for the state variables $S_{1,i}(z)$ and $S_{2,i}(z)$ we use the following expression

$$S_i(z) = \sum_m C_m w_{im} exp(\lambda_m z) \tag{3.65}$$

λ_m and ω_{im} are the eigenvalues and eigenvectors of matrix A. C_m represents unknown constants that can be determined from the boundary conditions.

The boundary conditions require that at the boundaries of $z = 0$ and $z = d$ the tangential components of the electric and magnetic fields are

continuous. The details of this derivation can be found in [100]. For the boundary between region I and II, where z=0, the boundary condition for tangential E is

$$\delta_{i0} + R_i = \sum_m C_m w_{im} \tag{3.66}$$

and for tangential H

$$(\delta_{i0} - R_i)k_{zi} = \sum_m C_{im}(k_{z0} + j\lambda_m) \tag{3.67}$$

where δ_{i0}, the Kronecker delta, has the following values: $\delta_{i0} = 1$ for $i = 0$ and $\delta_{io} = 0$ for $i \neq 0$. For the boundary between region II and region III ($z = d$), the boundary condition for tangential E is

$$T_i = \sum_m C_m w_{im} exp(\lambda_m d) \tag{3.68}$$

and for H

$$T_i k_{zi} = \sum_m C_m w(k_z + j\lambda_m) exp(\lambda_m d) \tag{3.69}$$

If there are N values of i retained in the analysis then equations 3.66, 3.67, 3.68 and 3.69 can be solved simultaneously for the N values of R_i and T_i [96].

3.4 Calculating Transmitted Intensity

In order to investigate the polarisation characteristics of the waves transmitted through arrays of subwavelength asymmetric cruciform apertures, it was necessary to obtain spectra using an analyser as well as a polariser (see Fig. 6.17). With the polariser fixed at a given angle transmission spectra are obtained for different angles of the analyser (this process will be discussed in detail later). It was also necessary to compare this experimental data with simulation data. However, simulations provide only information on the strength of the E-field in the x and y direction and their phase difference. Therefore the mathematical formula derived below was used with E-field data derived from RSoft to simulate the effect of an analyser.

In the following derivation a wave has passed through an array and is now elliptically polarised. This wave is propagating in the z direction and is normally incident upon a polariser (the equivalent of the analyser in the experimental setup). The polariser is oriented at an angle α to the x-axis (see Fig. 3.7). The phase difference between the x and y components is θ. We wish to calculate the dependence of the transmitted intensity upon α:

$$\mathbf{E}_{out} = (\mathbf{E}_{in}.\hat{\mathbf{r}}_p)\hat{\mathbf{r}_p} \tag{3.70}$$

Here

$$\mathbf{E}_{in} = \hat{\mathbf{x}}E_y \cos(\omega t - kz) + \hat{y}E_y \cos(\omega t - kz + \theta) \tag{3.71}$$

$$\hat{r}_p = \hat{x}\cos\alpha + \hat{y}\sin\alpha \tag{3.72}$$

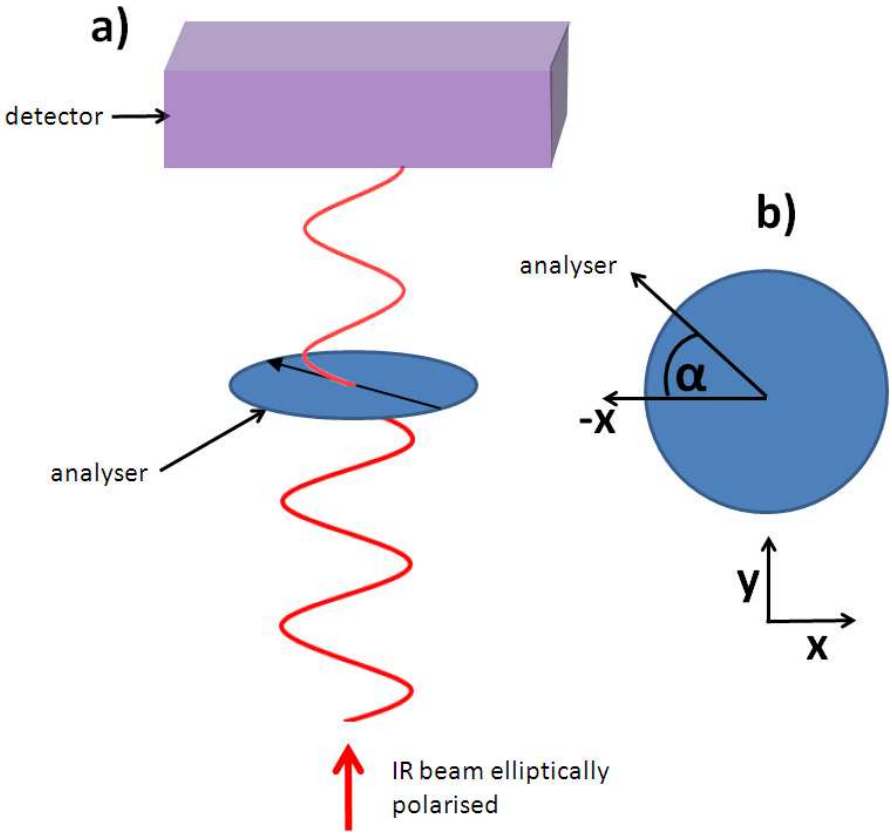

Figure 3.7: a) Perspective diagram of the arrangement of the analyser and detector. The IR beam that exits the array is normally incident upon an analyser oriented at an angle of α to the negative axis. b) Plan view of the analyser orientation showing that the angle of the analyser is measured relative to the negative x-axis.

Hence

$$E_{out} = E_x \cos(\alpha)\cos(\omega t - kz) + E_y \sin(\alpha)\cos(\omega t - kz + \theta) \tag{3.73}$$

We can simplify the equation, without loss of generality, by choosing z=0:

$$E_{out} = E_x \cos(\alpha)\cos(\omega t) + E_y \sin(\alpha)\cos(\omega t + \theta) \tag{3.74}$$

The intensity of the ouput, I_{out}, is proportional to the time average of E_{out}, so

$$E_{out}^2 = E_x^2 \cos^2(\alpha)\cos^2(\omega t)\cos(\omega t{+}\theta){+}2E_xE_y\cos(\alpha)\sin(\alpha)\cos(\omega t)\cos(\omega t{+}\theta) \tag{3.75}$$

The time average of $\cos^2(\phi)$ is equal to 1/2. To find the time average of the last term in equation 3.75 we note that

$$\cos(\omega t)\cos(\omega t + \theta) = (1/2)[\cos\theta + \cos(2\omega t + \theta)] \tag{3.76}$$

the time average of which is $1/\cos\theta$. Hence we obtain the result

$$I_{out} \sim < E_{out}^2 > = \frac{1}{2}(E_x^2\cos^2(\alpha) + E_y^2\sin^2(\alpha) + E_xE_y\cos\theta\sin(2\alpha)) \tag{3.77}$$

Now we wish to calculate the fraction of the elliptically polarised wave that passed through an analyser. To determine this value it is necessary to

perform a normalisation. Therefore the value of I_{out} must be divided by the total amount of light that was transmitted through the array, I_{total}.

The modulus of the total E-field can be obtained from

$$E_{total} = \sqrt{E_x^2 \cos^2(\omega t) + E_y^2 \cos^2(\omega t + \theta)} \tag{3.78}$$

However, the total transmission, I_{total}, is proportional to the time average of E_{total}^2, so

$$I_{total} \ < E_{total}^2 >= E_x^2 \cos^2(\omega t) + E_y^2 \cos^2(\omega t + \theta) \tag{3.79}$$

Which simplifies to

$$I_{total} \ < E_{total}^2 >= \frac{1}{2}(E_x^2 + E_y^2) \tag{3.80}$$

So the normalised transmission is

$$\frac{I_{out}}{I_{total}} = \frac{(E_x^2 \cos^2(\alpha) + E_y^2 \sin^2(\alpha) + E_x E_y \cos\theta \sin(2\alpha)}{E_x^2 + E_y^2} \tag{3.81}$$

3.5 Polarisation Ellipse

An important tool for understanding the polarisation of electromagnetic radiation is the polarisation ellipse. This provides information on whether the beam is linear, circular or elliptically polarized and also describes the angle of the polarisation (Fig. 3.8). The polarisation ellipse is derived as follows [101].

Sinusoidal oscillations in the x-z and y-z planes can be represented by

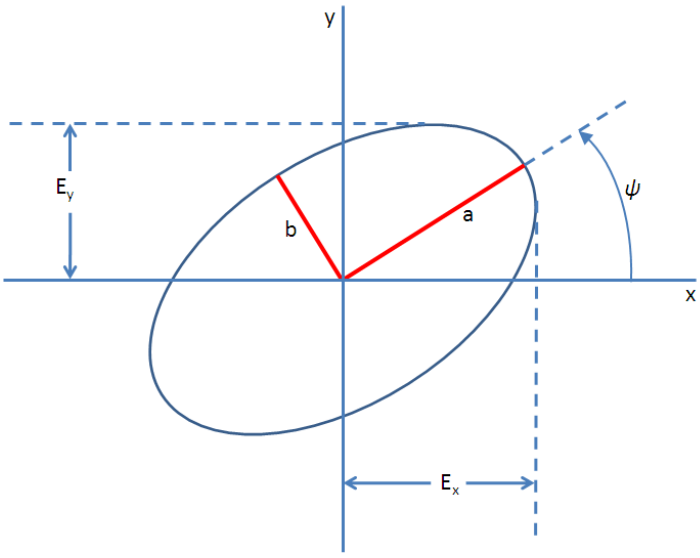

Figure 3.8: The polarisation ellipse defines the relative sizes of the major and minor axes and the angle at which the major axis is rotated from the horizontal.

$$E_x(z,t) = E_{0x}\cos(\omega t - \kappa z + \delta_x) \tag{3.82}$$

$$E_y(z,t) = E_{0y}\cos(\omega t - \kappa z + \delta_y) \tag{3.83}$$

where the terms δ_x and δ_y represent the phase of the E_x and E_y components respectively. These phase values are important for determining whether electromagnetic radiation is linearly polarised or elliptically/circularly polarised.

As the resultant field propagates it describes a curve in space. To derive the values for this curve, first write $\tau = \omega t - \kappa z$ and use trig identities to rewrite 3.82 and 3.83 such that

$$\frac{E_x}{E_{0x}} = \cos\tau\cos\delta_x - \sin\tau sin\delta_x \tag{3.84}$$

$$\frac{E_y}{E_{0y}} = \cos\tau\cos\delta_y - \sin\tau\sin\delta_y \tag{3.85}$$

multiplying 3.84 by $\sin\delta_y$ and 3.85 by $\sin\delta_x$ and combining the results

$$\frac{E_x}{E_{0x}}\sin\delta_y - \frac{E_y}{E_{0y}}\sin\delta_x = \cos\tau\sin(\delta_y - \delta_x) \tag{3.86}$$

then multiplying 3.84 by $\cos\delta_y$ and 3.85 by $\cos\delta_x$ and combining the results gives

$$\frac{E_x}{E_{0x}}\cos\delta_y - \frac{E_y}{E_{0y}}\cos\delta_x = \sin\tau\sin(\delta_y - \delta_x) \tag{3.87}$$

If we square 3.86 and 3.87 and add them together we obtain

$$\frac{E_x^2}{E_{0x}^2} + \frac{E_y^2}{E_{0y}^2} - \frac{2E_xE_y\cos\delta}{E_{0x}E_{0y}} = \sin^2\delta \tag{3.88}$$

where $\delta = \delta_y - \delta_x$

Equation 3.88 is known as the polarisation ellipse, and the E_xE_y term shows that the ellipse is a rotated ellipse. From this equation the angle ψ, which the major axis of the ellipse makes with the x axis, can be be derived [101]:

$$tan2\psi = \frac{2E_{0x}E_{0y}\cos\delta}{E_{0x}^2 - E_{0y}^2} \tag{3.89}$$

If we obtain the analyser angle at which there is peak transmission for a

given incident polarisation angle, this corresponds to the angle of the transmitted major axis. We can compare this angle to the angle of the input polarisation to determine a shift in polarisation angle. To use the simulation data to obtain full information regarding the polarisation state of the transmitted beam, we must also employ the Stokes parameters.

3.6 The Stokes Parameters

The Stokes Parameters are a set of equations that can be used to determine the polarisation state of a wave in terms of the angle of its major axis, the relative size of the major and minor axes, and the sense of the polarisation, i.e, whether it is clockwise or anticlockwise. These equations can be used in conjunction with data obtained either experimentally or through simulations. For this research only appropriate simulation data was obtainable owing to the limitations of the experimental set up. However, it was still possible to make useful comparisons between simulation data used with the Stokes Parameters and data derived from experiments.

The Stokes parameter can be derived as follows [101]: Consider a pair of orthogonal plane waves at a point in space z=0.

$$E_x(t) = E_{0x}(t)\cos[\omega t + \delta_x(t)] \tag{3.90}$$

$$E_y(t) = E_{0y}(t)\cos[\omega t + \delta_y(t)] \tag{3.91}$$

If we remove the term ωt from both equations, we obtain the equation of the polarisation ellipse, valid only at a given instant of time.

$$\frac{E_x^2(t)}{E_{0x}^2(t)} + \frac{E_y^2(t)}{E_{0y}^2(t)} - \frac{2E_x(t)E_y(t)\cos\delta(t)}{E_{0x}(t)E_{0y}(t)} = \sin^2\delta(t) \tag{3.92}$$

where

$$\delta(t) = \delta_y(t) - \delta_x(t) \tag{3.93}$$

For monochromatic radiation the amplitudes and the phases remain constant, so 3.92 can be simplified to

$$\frac{E_x^2(t)}{E_{0x}^2} + \frac{E_y^2(t)}{E_{0y}^2} - \frac{2E_x(t)E_y(t)}{E_{0x}E_{0y}}\cos\delta = \sin^2\delta \tag{3.94}$$

Since $E_x(t)$ and $E_y(t)$ vary over time it is necessary to take an average, which, in view of their periodicity, can be taken over the period of a single oscillation

$$\frac{\langle E_x^2(t)\rangle}{E_{0x}^2} + \frac{\langle E_y^2(t)\rangle}{E_{0y}^2} - \frac{2\langle E_x(t)E_y(t)\rangle}{E_{0x}E_{0y}}\cos\delta = \sin^2\delta \tag{3.95}$$

If we multiply equation 3.95 by $4E_{0x}^2E_{0y}^2$, we obtain

$$4E_{0y}^2\langle E_x^2(t)\rangle + 4E_{0x}^2\langle E_y^2(t)\rangle - 8E_{0x}E_{0y}\langle E_x(t)E_y(t)\rangle\cos\delta = (2E_{0x}E_{0y}\sin\delta)^2 \tag{3.96}$$

Using 3.90, 3.91, we can then obtain the values in 3.96 for which we wish to obtain an average

$$\langle E_x^2(t)\rangle = \frac{1}{2}E_{0x}^2 \tag{3.97}$$

$$\langle E_y^2(t)\rangle = \frac{1}{2}E_{0y}^2 \tag{3.98}$$

$$\langle E_x(t)E_y(t)\rangle = \frac{1}{2}E_{0x}E_{0y}\cos\delta \tag{3.99}$$

If we substitute these three equations into 3.96, we obtain:

$$2E_{0x}^2E_{0y}^2 + 2E_{0x}^2E_{0y}^2 - (2E_{0x}E_{0y}\cos\delta)^2 = (2E_{0x}E_{0y}\sin\delta)^2 \tag{3.100}$$

In order to express this result as an intensity we add and subtract $E_{0x}^4 + E_{0y}^4$ to the left-hand side, which leads to perfect squares. If we then group terms the following is obtained:

$$(E_{0x}^2 + E_{0y}^2)^2 - (E_{0x}^2 - E_{0y}^2)^2 - (2E_{0x}E_{0y}\cos\delta)^2 = (2E_{0x}E_{0y}\sin\delta)^2 \tag{3.101}$$

The quantities inside the parenthesis are now written as

$$S_0 = E_{0x}^2 + E_{0y}^2 \tag{3.102}$$

$$S_1 = E_{0x}^2 - E_{0y}^2 \tag{3.103}$$

$$S_2 = 2E_{0x}E_{0y}\cos\delta \tag{3.104}$$

$$S_3 = 2E_{0x}E_{0y}\sin\delta \tag{3.105}$$

3.101 can then be expressed as

$$S_0^2 = S_1^2 + S_2^2 + S_3^2 \tag{3.106}$$

The four equations 3.102, 3.103, 3.104 and 3.105 are known as the Stokes parameters and are the observables of the polarisation ellipse. S_0 is the total intensity of the light, S_1 represents the amount of linear horizontal or vertical polarisation. S_2 describes the amount of linear $+45°$ or $-45°$ polarisation. S_3 describes the amount of right or left circular polarisation contained within the beam, such that when $S_3 > 0$ the transmitted beam is anticlockwise polarised and when $S_3 < 0$ the beam is clockwise polarised.

Further analysis enables the values of the polarisation ellipse to be derived from the Stokes parameters, leading to

$$S_0 = a^2 + b^2 \tag{3.107}$$

$$S_1 = (a^2 - b^2)cos\psi \tag{3.108}$$

$$S_2 = (a^2 - b^2)sin\psi \tag{3.109}$$

$$S_3 = abh \tag{3.110}$$

where h is the sense of polarisation.

Thus the relative dimensions of the major and minor axis, a and b, of the polarisation ellipse can be obtained.

$$a = \sqrt{\frac{1}{2}(S_1 + \sqrt{S_2^2 + S_3^2})} \tag{3.111}$$

$$b = \sqrt{\frac{1}{2}(S_1 + \sqrt{S_2^2 - S_3^2})} \tag{3.112}$$

3.7 Wood's Anomaly

An observed phenomenon on diffraction gratings is a transmission minima termed the Wood's Anomaly [62][63]. This occurs because at certain critical wavelengths the diffracted light lies in the plane of the grating. For a periodic array in which transmission occurs owing to surface plasmons, the wavelengths at which Wood's anomalies occur can be determined as follows [102]. The following derivation will deal with p-polarised light. First it is necessary to determine the positions of zero order transmission maxima that result from excitations of extended surface plasmons. This interaction occurs via coupling with the grating momentum and obeys conservation of momentum

$$\overrightarrow{k}_{sp} = \overrightarrow{k}_x \pm i\overrightarrow{g}_x \pm j\overrightarrow{g}_y \tag{3.113}$$

where $\overrightarrow{k}_{sp}$ is the surface plasmon wave vector and $\overrightarrow{k}_x$ is the component of the wave vector that lies in the plane of the sample. The terms $\overrightarrow{g}_x$ and $\overrightarrow{g}_y$

are the reciprocal lattice vectors for a square lattice, where both are equal to $\frac{2\pi}{\Lambda}$, and i and j are integers.

Using the dispersion relation 3.11 and adapting it for a surface plasmon dispersion appropriate for a smooth film [31] we obtain:

$$|\overrightarrow{k}_{sp}| = \frac{\omega}{c} Re\left(\frac{\epsilon_1\epsilon_2}{\epsilon_1+\epsilon_2}\right)^{\frac{1}{2}} \tag{3.114}$$

where ω is the angular frequency, ϵ_1 is the permittivity of the dielectric and ϵ_2 is the permittivity of the metal.

When the beam is at normal incidence 3.113 and 3.114 simplify to

$$(i^2+j^2)^{\frac{1}{2}}\lambda_{SPP} = \Lambda Re\left(\frac{\epsilon_1\epsilon_2}{\epsilon_1+\epsilon_2}\right)^{\frac{1}{2}} \tag{3.115}$$

The condition for the Wood's anomaly is similar to that of equation 3.113 but instead of exciting a surface plasmon a diffracted wave that grazes off the surface is produced. This has wave vector

$$\overrightarrow{k}_{diff} = \frac{n\omega}{c} = \frac{2\pi n}{\lambda} \tag{3.116}$$

Where $n_d = Re\epsilon^{\frac{1}{2}}$ is the refractive index of the dielectric. Thus for the Wood's anomaly equation 3.114 becomes

$$(i^2+j^2)^{\frac{1}{2}}\lambda_W = n_d\Lambda \tag{3.117}$$

Chapter 4

Fabrication of Arrays

4.1 Arrays of Asymmetric Cruciform Apertures

The transmission characteristics of arrays of symmetric cruciform apertures have been studied both theoretically and experimentally [103, 104, 15, 69]. In such cases, the LSP resonances consist of two degenerate modes orthogonally polarized with respect to each other and thus the transmission is insensitive to polarisation. The work of Panoiu et al [61], however, determined theoretically that it should be possible to tailor the properties of LSPs in asymmetric cruciform apertures in metallic films. For asymmetric cruciform apertures the plasmonic resonances are then strongly dependent on the polarisation of the incoming mid-infrared beam. To test this theory a series of arrays was fabricated consisting of asymmetric cruciform apertures based on simulations carried out by Claudiu Biris under the supervision of Nicolae Panoiu. The dimensions of the fabricated apertures were partly dictated by the minimum dimensions that can be fabricated using the focused ion beam (FIB) but also by the wavelengths that can be observed using the Fourier transform infrared spectrometer (FTIR). The minimum feature size that was achieved using the FIB to create arrays of repeated structures was around 80 nm, while the FTIR, which operates in the mid-infrared range, can detect a minimum wavelength of around 2 μm owing to the limitation of the MCT detector.

4.2 Substrates

The substrates employed were silicon and CaF2. Silicon is transparent in the ranges 1.2 to 15 and has a refractive index of 3.4223 at 5 [105]. CaF2 is transparent between 0.2 and 9 and its refractive index ranges from 1.45 at 1 to 1.34 at 8.6 [106, 107]. The CaF2 was purchased as 22 mm diameter 0.5 mm thick IR single crystal polished windows. The silicon was a standard one side polished disk cut to smaller sizes of around 1 cm^2. The rough side of these was then ground and polished to produce a window of less than 200 μm thick. Initially both of these substrates were employed for their transparency in the Mid IR range. However, silicon's high refractive index results in high reflection so CaF_2 was preferred.

4.3 Deposition

A 5 nm layer of Chromium was thermally evaporated on the CaF_2 substrate as an adhesion layer. Gold was then thermally evaporated on the chromium. In early fabrication experiments the gold was 100nm thick, while in later experiments the gold was reduced to 30 nm to decrease the absorption of the IR signal (Fig. 4.1). The device used to deposit the Chromium and Gold was an Edwards 306BellJar. In this device the sample is placed in a vacuum and the materials to be deposited are heated until they melt and begin to evaporate. The evaporated atoms have a large mean free path owing to the high vacuum (of the order 10^{-7} mb) and so move without encountering gas particles. As a result, the surface of the substrate acquires an even thin layer

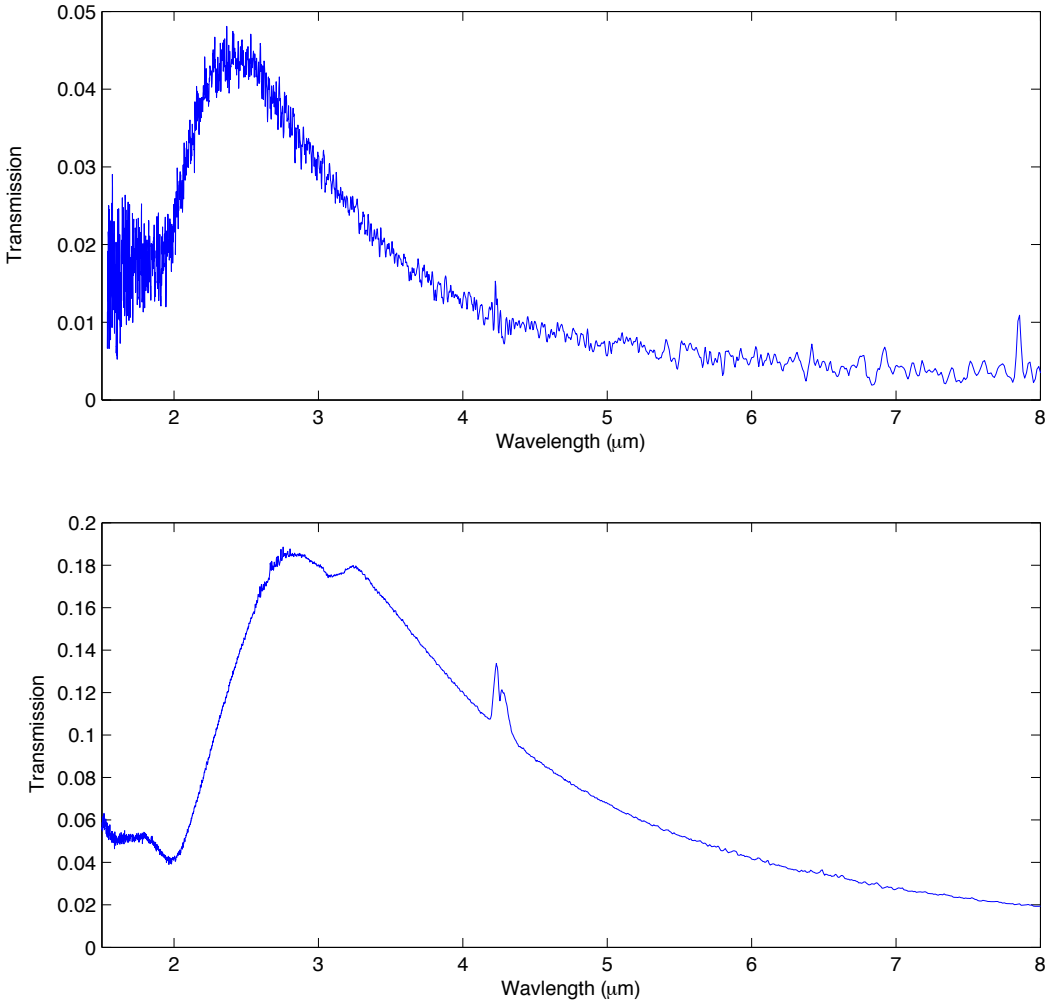

Figure 4.1: Transmission spectra for an unpolarised source incident on a cruciform aperture array. The top figure shows data for a sample with a 100nm layer of Au, while the bottom figure shows data for a sample with a 30nm layer of Au. The figure on the bottom has a substantially higher transmission owing to its thinner gold layer producing lower losses.

of the required metal. A crystal monitor detects the thickness of the metal layer deposited on the sample.

4.4 Crossbeam

The Crossbeam consists of a focused ion beam (FIB) and a field emission scanning electron microscope (FESEM), or SEM, both contained within a vacuum system and chamber. Together they enable the user to pattern and view a sample. The focused ion beam was developed as a consequence of research, carried out by Krohn in 1961 [108, 109], on liquid-metal ion sources for use in space. The first commercially available FIB systems were produced in the 1980s and were mostly used by the semiconductor industry. FIB systems consist of a liquid metal ion source, an ion column, a remotely manoeuvrable sample stage, detectors, gas inlets and a computer [110, 111] (Fig. 4.2). The ion source employed ionized atoms of a relatively heavy element (in this case gallium) that are accelerated and focused onto a sample using electric fields. The ion beam can be used to mill or image the surface of the sample and can also be used to deposit material onto a sample from a gaseous precursor. The force that ions impart when they impact on the sample surface causes surface atoms to be expelled. This process also produces secondary electrons, which can be used to image the surface. The rate at which surface atoms are removed depends on the time the beam remains at a particular position (the dwell time), the magnitude of the beam current (typically 50pA) and the spot size of the beam (typically around 25nm). Together these form the dose, measured in charge per unit area. The gallium ions are produced by first melting gallium in a reservoir until it almost evaporates. The liquid gallium then flows downwards onto a tungsten tip, the head of which is around 2-5μm in radius. The Ga is drawn to the tip by

an electric field produced by an annular electrode - the extractor - encircling the tip, using a combination of electrostatic and surface tension forces. An electric field of around 10^{10} V/m is produced between the tungsten tip and an aperture positioned directly below the tip. Energetic Ga atoms are drawn off the tip by the electric field and are ionized by field evaporation. They are then accelerated down the ion column by a potential of 30 keV. The beam is focused to a point using electrostatic fields, and the shape of the beam is optimised using stigmators.

Since the SEM uses electrons to image the sample rather than much heavier ions, the user can view the sample using SEM without causing damage to the viewed area. The beams are positioned at an angle of 54° to each other and the beams are focused to a coincident point, which allows the operator to view and mill the sample without having to change its position. The working distance is typically 5 mm.

4.4.1 Milling

The substrates employed for the fabrication of cruciform aperture arrays were silicon and CaF_2 with, initially, a 100 nm layer of Au with a 5nm layer of Cr to provide adhesion. The thickness of the Au layer was reduced to 30 nm to reduce ohmic losses during transmission measurements. The samples were attached to a conducting stub using either conducting tape or conducting silver paint. This is necessary to prevent charging of the Au by the SEM electrons (charging has the effect of deflecting the FIB beam). Both attaching methods have advantages and disadvantages. The tape is

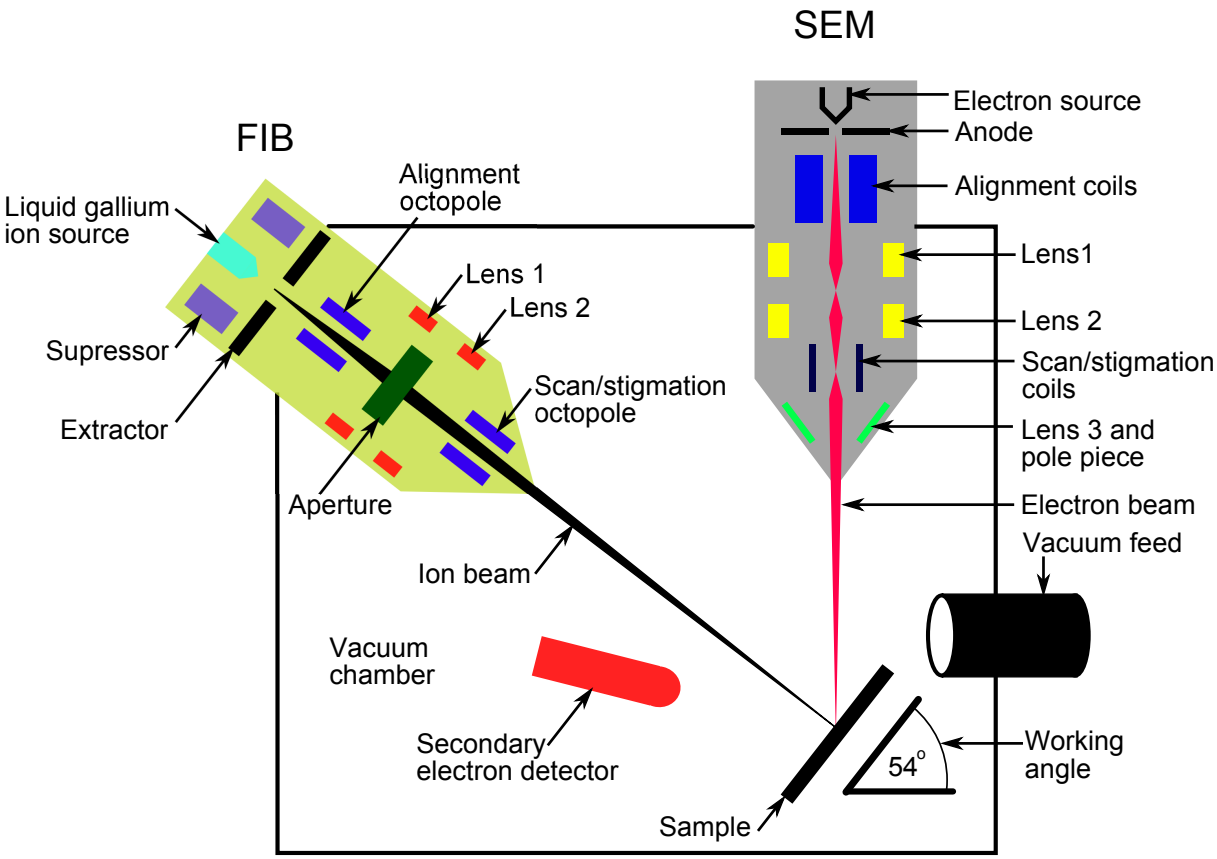

Figure 4.2: The crossbeam consists of two main components: the scanning electron microscope and the focused ion beam, both mounted so that their beams are contained within a vacuum chamber. Together these systems enable the milling and imaging of nanoscale structures.

easier to manipulate but is harder to remove. Removal sometimes leads to the shattering of the sample. Silver paint is easy to remove using solvent but during application there is a strong risk of splashing paint on the sample surface. Silver paint was ultimately preferred owing to the high number of shattered samples that occurred using tape. The sample and stub are placed on to a rotatable sample holder that can be manoeuvred in and out of the FIB vacuum chamber via an airlock and a manipulating arm.

Arrays of asymmetric cruciform apertures were milled into the surface of

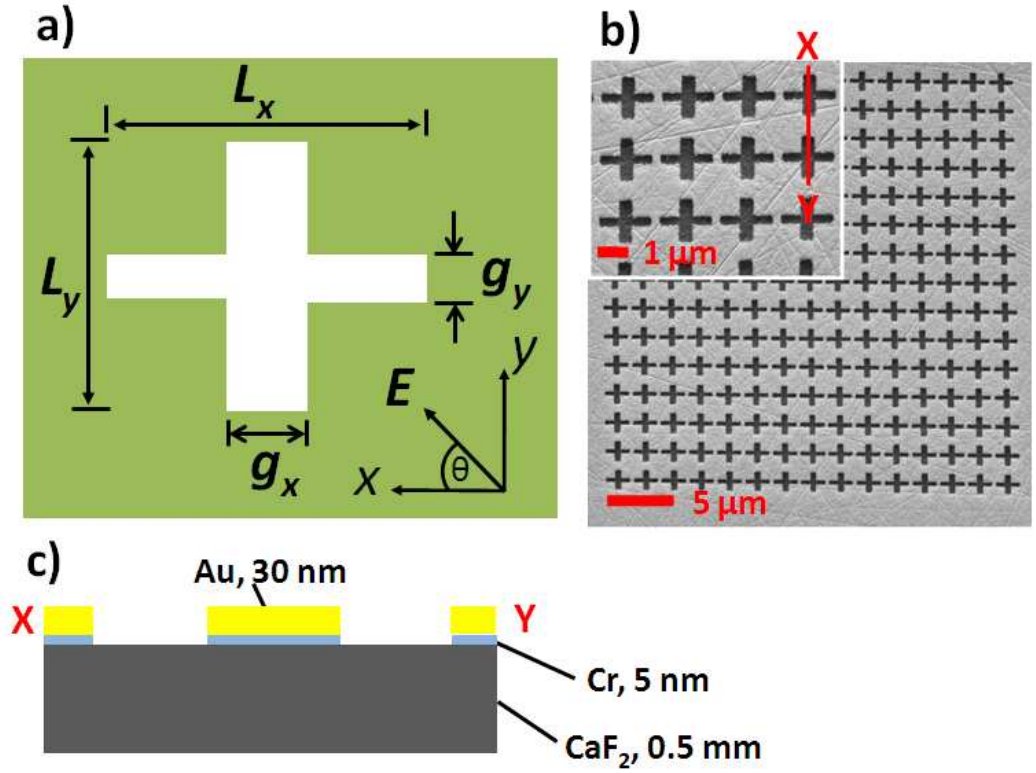

Figure 4.3: (a) Schematic of the unit cell also showing the definition of the in-plane electric-field polarisation angle, θ. (b) Scanning electron micrograph of an array with the inset showing magnified detail. (c) Schematic cross-section through the XY-segment, as shown in (b).

the Au using a 30 kV gallium focused-ion-beam. The beam current was 50 pA and the dose 50 pC/μm^2. The device structure and a fabricated array are shown in Fig. 4.3.

Each array had 15 x 15 unit cells and a lattice constant in both the x and y directions of $\Lambda = 2\mu$m. The arrays therefore had dimensions 30 x 30 μm^2. The size of the array is large enough so that size-dependent array effects are negligible [37]. Such effects are the result of coupling between apertures. For an increasing number of apertures, the transmission will increase until it

reaches a maximum beyond which additional apertures make no difference to the transmission. A similar array of symmetric cruciform apertures was fabricated as a control sample. This array had the same periodicity and same number of unit cells as the arrays of asymmetric apertures.

In milling arrays it must be noted that the size of features in the design, whether using bitmap images or dxf files, does not correspond to the size of features produced using the FIB. This is in part due to inaccuracies produced by, for example, redeposition, but is also, and more problematically, an issue resulting from the interpretation of the designed image by the FIB software. Before the FIB can be used to pattern the gold surface, the design must be uploaded and displayed on the portion of the gold to be patterned. This is carried out using an FIB software facility called feature mill. First, an area of the gold surface is selected, then feature mill is activated, which opens a window showing a screen shot of the selected area. The array design is then opened in this window where it is shown superimposed on the gold surface. The design is then manually sized as appropriate by stretching the design across the screenshot. However, the pixel size of the FIB software does not map smoothly with the pixel size of the design, resulting in irregularities in the dimensions of the cruciform apertures. Thus the milling process also mills these irregularities. Also, the larger the dimensions of the array, the greater are these adverse effects. By producing smaller arrays these designs can be shown at a larger scale in the feature mill window and so there is greater resulting conformity in the milled apertures.

Chapter 5

Transmission and Reflection Measurements Using FTIR

5.1 Fourier Transform Infrared Spectroscopy

The Fourier Transform Infrared Spectrometer (FTIR) was used to determine the fraction of light that is transmitted through, or reflected by, the samples. The experimental apparatus consisted of two main components: the FTIR spectrometer and the microscope (Fig. 5.1). At the heart of the spectrometer is an interferometer, first designed by Michelson in 1891 [112, 113].

An interferometer is a device that splits a beam into two paths using a beam splitter, and then recombines them. The variation in intensity of the resulting beam can then be measured as a function of path difference. In the case of the Michelson interferometer, one of the split beams reflects off a mirror that moves with a constant velocity so that the path distance constantly changes. If we consider a monochromatic source with a wavenumber σ_0 and an intensity $B(\sigma_0)$ [114, 115], then the intensity of the signal can be expressed as a function of the optical path difference between the two beams,

$$I_0(x) = B(\sigma_0)[1 + \cos(2\pi\sigma_0 x)] \tag{5.1}$$

where σ is the wavenumber, defined by $\sigma = \frac{1}{\lambda} = \frac{\nu}{c}$ and measured in reciprocal centimetres. As the moving mirror scans back and forth, the resulting combined beam displays patterns of constructive and destructive interference, and the resulting signal over the complete movement of the mirror is called the interferogram. The inteferogram is a cosine with spatial frequency, or wavenumber, σ. If we then consider a source that has more than one frequency, then the result is a superposition of such cosines,

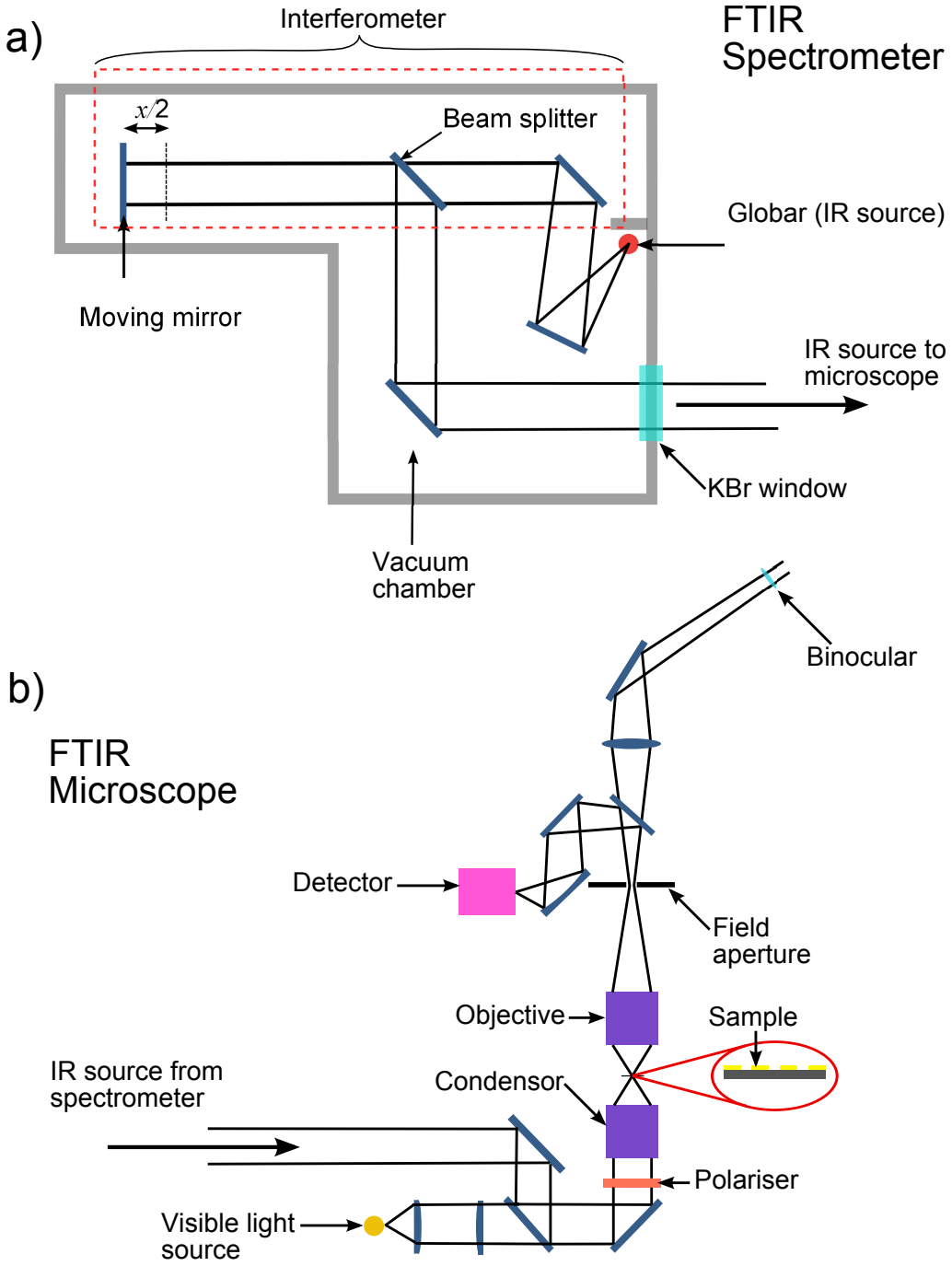

Figure 5.1: a) The arrangement of the FTIR spectrometer. This equipment can be used independently to analyse the transmission properties of bulk materials. b) The arrangement of the FTIR microscope, which enables transmission spectra to be obtained for small specific regions of a sample.

$$I_0(x) = \int_0^\infty B(\sigma_0)[1 + \cos(2\pi\sigma_0 x)]d\sigma \tag{5.2}$$

and the interferogram tends towards a sharp transmission peak (Fig. 5.2). If the mean value of the interferogram is subtracted, an expression for the intensity as a function of x is formed,

$$I(x) = I_0(x) - \overline{I(x)} = \int_0^\infty B(\sigma_0)[1 + \cos(2\pi\sigma_0 x)]d\sigma \tag{5.3}$$

This is the information that arrives at the detector. By performing the inverse Fourier transform on the interferogram the original source spectrum can be retrieved. The position of the mirror is determined by a HeNe laser (wavelength 633 nm), which follows the IR beam path in the interferometer. Thus as the mirror moves, the HeNe beam experiences a periodic series of interference maxima and minima. The position of the moving mirror is determined by zero crossings of this beam, that is, the path difference between an interference maxima and an interference minima. Therefore the minimum measurable distance moved by the mirror is half the HeNe laser wavelength (316.5 nm).

Since this signal varies with changing position of the mirror, the natural units of transmission are the inverse of distance and are therefore wavenumbers in cm^{-1}, though for this research all transmission spectra data were converted to wavelength in μm.

The interferogram signal passes out of the interferometer chamber via a KBr window and enters the FTIR microscope. In transmission mode, the optics of this device are arranged as in Fig. 5.1b. Before a transmission

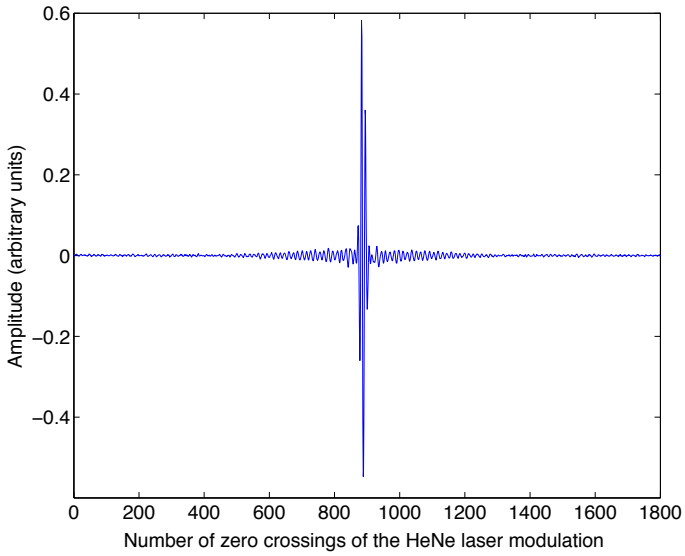

Figure 5.2: An interferogram

spectrum of the sample array can be obtained it is necessary to obtain a background, or reference, transmission spectrum for the purpose of normalization. This is also referred to as the single-channel spectrum, reference (abbreviated to RSC). The method for taking a background scan depends on the experiment being carried out. In this case it is necessary to remove the effects of transmission through air and the CaF_2 substrate; the characteristics of the IR source; and the characteristics of the detector to understand what fraction of the signal is transmitted through the array. Therefore the transmission through the bare CaF_2 substrate was used as the background. An area of the substrate is positioned at the focus of the beam. The visible light source and the binoculars are used to focus onto the substrate and select a clear region. A microscope aperture is selected. This must be the same size as the microscope aperture used to obtain the transmission through

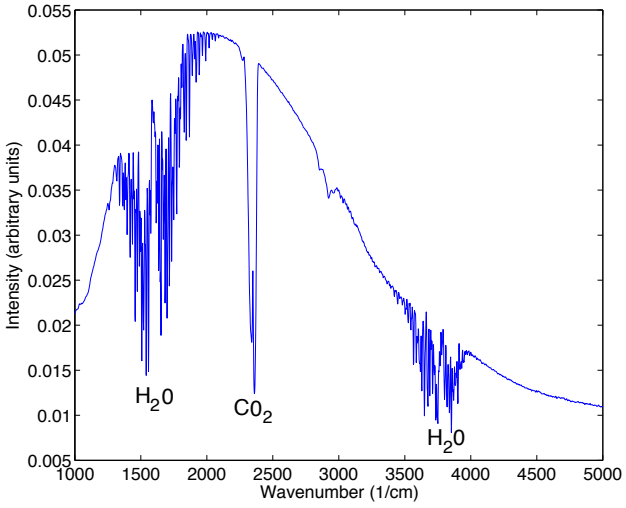

Figure 5.3: A background transmission spectrum, or RSC, for a 0.5 mm thick CaF_2 sample. The absorption by atmospheric $C0_2$ and H_20 are shown. The maximum around 2000 wavenumbers ($\lambda = 5$) indicates that the signal through the CaF_2, as detected by the detector, is strongest at this point.

the array. In most of the experiments carried out here the arrays were 30 x 30 μm. The microscope aperture size chosen was 30 μm diameter, which allowed for the maximum amount of light to be transmitted through the array. This was necessary as the signal at such small microscope apertures is greatly reduced. A background transmission spectrum is then obtained through the bare CaF_2 and the results are displayed as a function of intensity (in arbitrary units) against wavenumber in reciprocal centimetres. An example background spectrum is shown in Fig.5.3.

This spectrum shows the intensity of the signal over its wavelength range, but also is a product of the sensitivity of the detector over the complete spectral range combined with the effect of absorption of particular wavelengths by atmospheric gases, as well as absorption by the CaF_2.

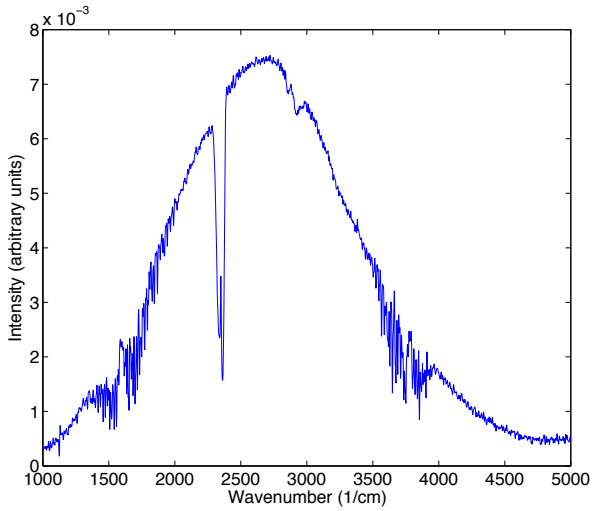

Figure 5.4: A single channel spectrum, or SSC, of a cruciform aperture array.

The second stage is to obtain a transmission spectrum through the substrate and array. This is referred to as the single-channel spectrum, sample (abbreviated to SSC). The array is carefully positioned so that the aperture is entirely within the bounds of the array. An example of an SSC is shown in Fig. 5.4.

The next stage is carried out automatically by the OPUS software. The SCC intensity data are divided by the RSC intensity data resulting in the fraction of the beam signal transmitted as a function of wavenumber (Fig. 5.5). This resulting transmission data are referred to as TR. The x axis data are then converted from wavenumbers to microns as shown in Fig. 5.6.

For the mid-IR region used in this research, the source is a globar, the beam splitter is made of KBr, and the detector is a liquid-nitrogen cooled mercury cadmium telluride (MCT) detector. One of the advantages of an FTIR is that it simultaneously obtains data for a broad band of wavelengths,

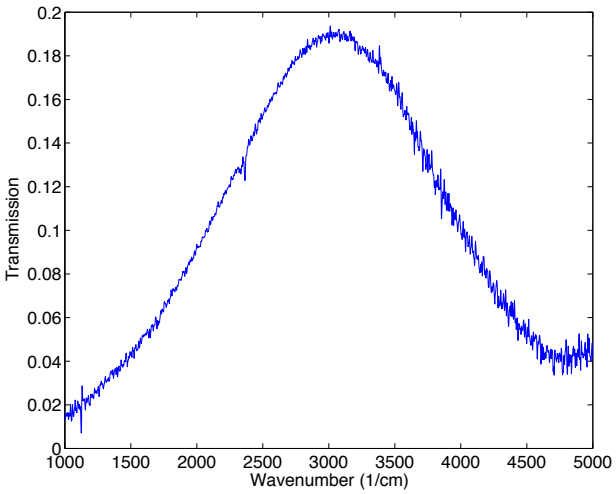

Figure 5.5: A transmission spectrum for the cruciform aperture array obtained by dividing the SSC intensity data by the RSC intensity data.

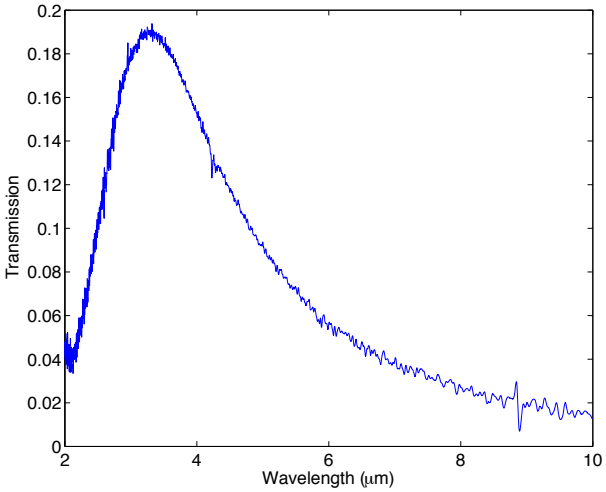

Figure 5.6: The same transmission spectrum as in Fig. 5.5 but with the x-axis converted to microns

thus vastly reducing the data acquisition time necessary by comparison with other types of spectrometer that produce transmission spectra wavelength by wavelength. To obtain information on polarisation characteristics, an optional IR polarising filter can be placed before the condenser lens. An additional polariser can also be included for use as an analyzer by placing it between objective and the field aperture.

The spot size of the beam incident onto the underside of the sample was 0.33 mm and is thus substantially larger than the array. The metal films are optically opaque for the thickness used in our experiments and therefore the measured transmission corresponds to the light transmitted through the aperture array. Transmission data were obtained for incident in-plane polarisation angles (as defined in Fig. 4.3a) between $\theta = 0$ and $\theta = 90^\circ$ in 15° increments. According to manufacturer's data, the extinction ratio of the polarizer varied from 100 to 300 across the range of wavelength values observed.

Chapter 6

Results and Discussion

6.1 Transmission Data

An array with designed cruciform dimension L_x = 1660 nm, L_y = 920 nm, g_x = 360 nm and g_y = 120 nm was milled in 30 nm Au on 5 nm Cr on a 0.5 mm thick CaF_2 substrate. Both L and g were varied as this produced clear and distinct resonances in simulations, without any overlapping of lsp resonances with propagating surface plasmon resonances. The array had 15 x 15 unit cells and a periodicity of $\Lambda = 2\mu m$ (see Fig. 6.1). When measured using SEM, the mean dimensions were found to be L_x = 1675 nm, L_y = 1003 nm, g_x = 418 nm and g_y = 165 nm The array's transmission characteristics were measured using FTIR. The transmission spectra for the asymmetric cruciform array are displayed in Fig. 6.2a.

Two distinct peaks are observed and the positions of these peaks, to within the accuracy of the measurement, are invariant with respect to the angle of polarisation (where $\theta = 0°$ represents the E-field parallel to the x-axis). These two peaks, A and B, occur around $\lambda = 3.9\ \mu m$ and $\lambda = 5.75\ \mu m$ respectively. As the polarisation angle is changed from $\theta = 0$ to $\theta = 90°$, the amplitude of peak A decreases from its maximum value reached at $\theta = 0$ and eventually decays to below the noise level. Conversely, peak B begins to emerge and increases in amplitude to reach its maximum at $\theta = 90°$. The spectra in Fig. 6.2a also show a point, I, at which transmission is independent of polarisation. This point occurs around $\lambda = 4.46\mu m$. Drawing from an analogy from molecular spectroscopy, point I is termed an isosbestic point.

An isosbestic point is defined as a wavelength, wavenumber or frequency at which the total absorbance of a sample does not change during a chemical

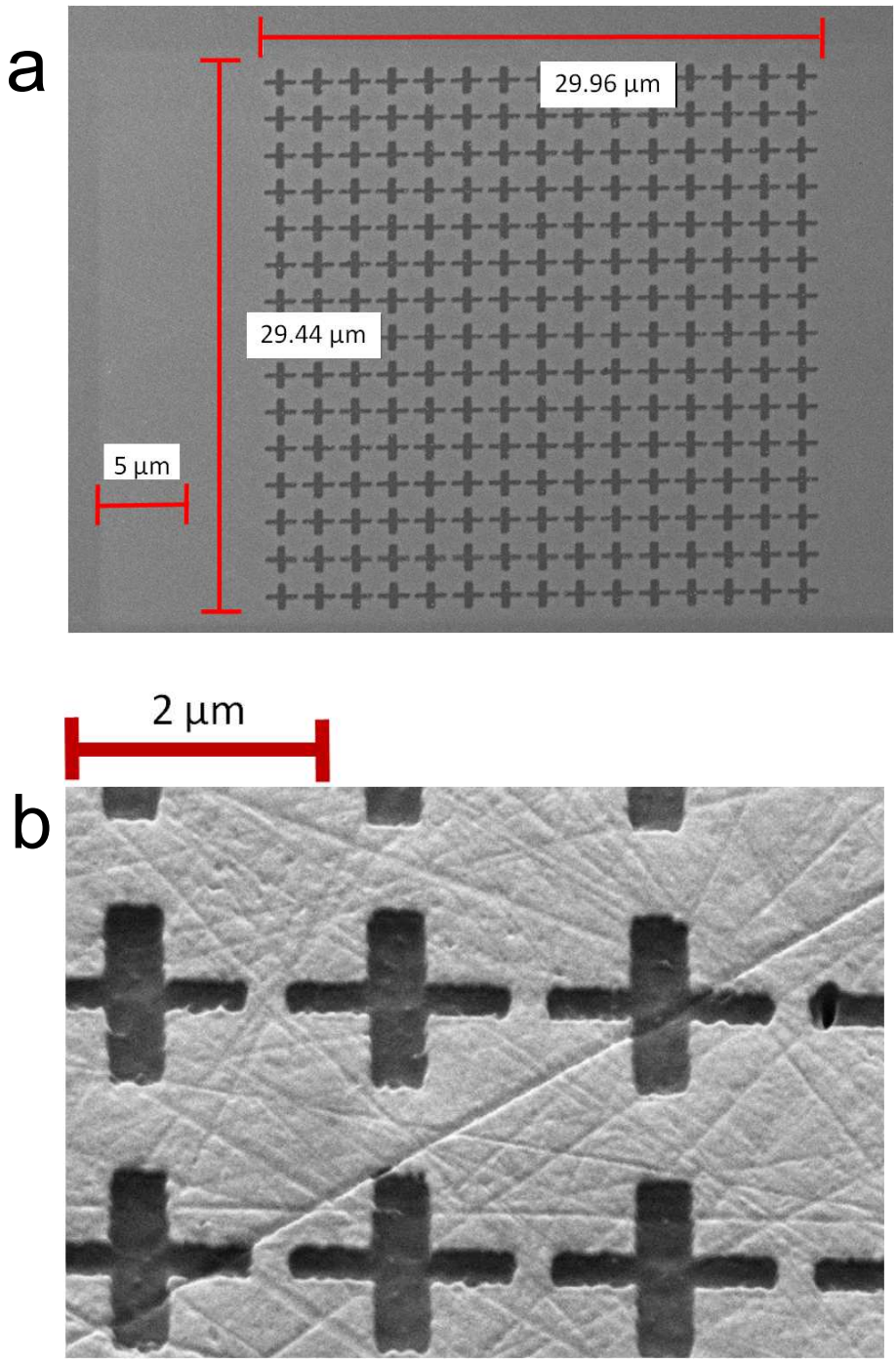

Figure 6.1: a) A scanning electron micrograph of the array with measured dimensions of $L_x = 1675$ nm, $L_y = 1003$ nm, $g_x = 418$ nm and $g_y = 165$ nm. b) Close up of array's unit cells.

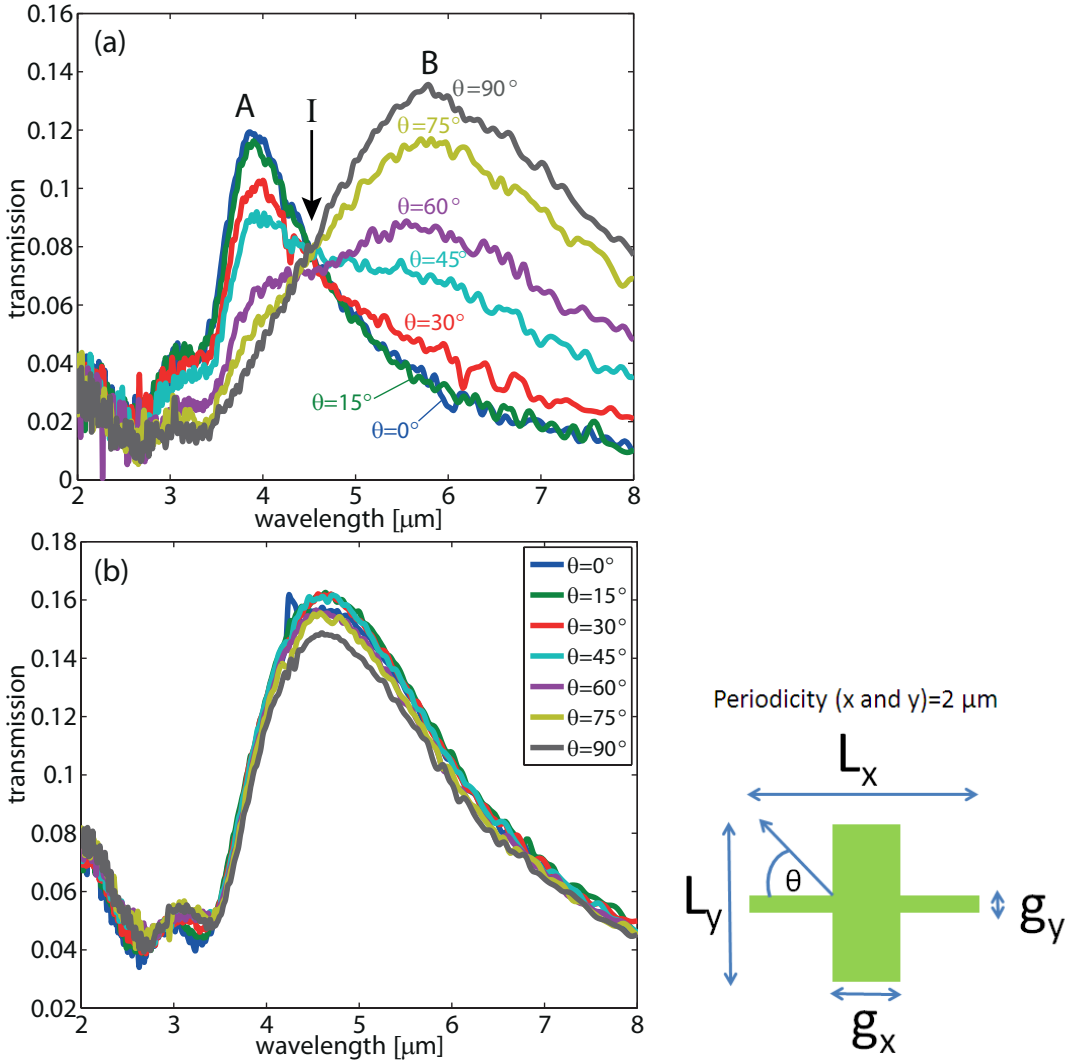

Figure 6.2: (a) Measured FTIR transmission spectra for an array of asymmetric cruciform apertures with $L_x = 1675$ nm, $L_y = 1003$ nm, $g_x = 418$ nm and $g_y = 165$ nm. (b) Measured FTIR transmission spectra for the control array of symmetric cruciform apertures with dimensions $L_x = L_y = 1264$ nm and $g_x = g_y = 368$ nm.

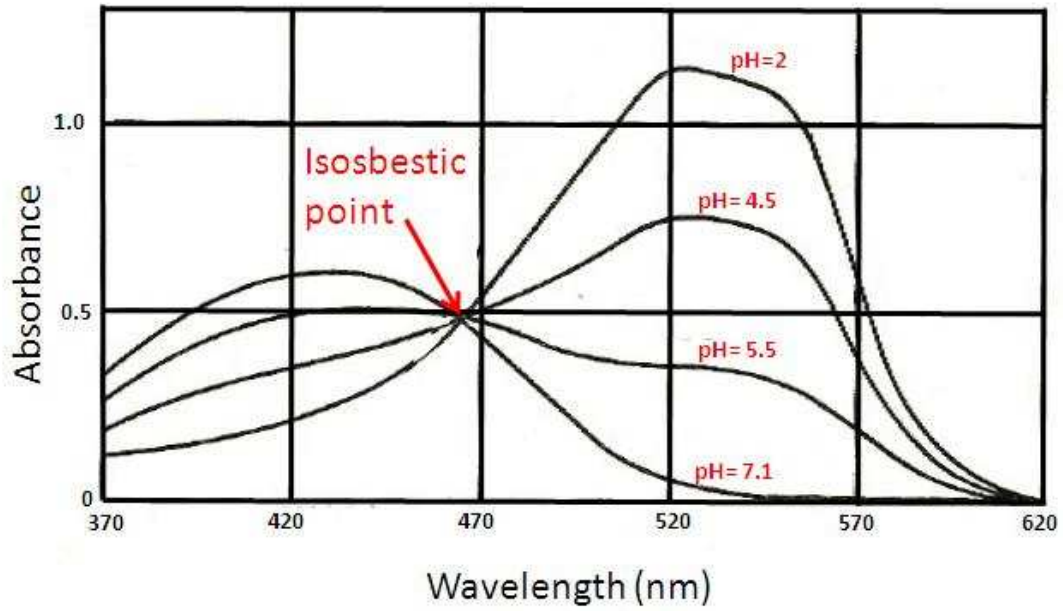

Figure 6.3: Image taken from King [117]. The absorption spectra for methyl red at a concentration of 0.01 percent as a function of pH for values ranging from a pH of 4.5 to 7.1. The wavelength at which the transmission is invariant is termed the isosbestic point.

.

reaction or a physical change of the sample [116]. This term derives from a Greek word meaning "equal extinction." A simple example occurs for the pH indicator methyl red when absorption spectra of solutions of varying pH are taken (see Fig. 6.3). At a wavelelength $\lambda = 456nm$, the isosbestic point, the absorption is invariant.

By comparison, the spectra for the control array of symmetric cruciform apertures show a single peak (see Fig. 6.2b) and, within the inherent variations introduced by the fabrication process, the transmission is insensitive to the polarisation of the electric field. In addition, at $\lambda = 3.3$ μm, for arrays

of both asymmetric and symmetric apertures, a minimum is observed. This minimum corresponds to the Wood's anomaly of the periodic array, which from equation 3.117 is predicted to occur at $\lambda_W = n_d\Lambda/\sqrt{i^2+j^2}$, where n_d is the index of refraction of the dielectric medium and i and j are mode indices. In the case of square arrays the largest wavelength at which the Wood's anomaly occurs corresponds to $i = 1$ and $j = 0$. As such, for an array with $\Lambda = 2$ μm the wavelength of the Wood's anomalies corresponding to Au-air ($n_d = 1$) and Au-CaF_2 ($n_d = 1.4$) interfaces are $\lambda_W = 2$ μm and $\lambda_W = 2.8$ μm, respectively.

6.2 Transmission Simulations

A set of simulations was carried out to compare the experimental data with theoretically derived data. This required two types of simulation data: transmission spectra for each polarisation and electric field profiles for an individual cruciform. In these simulations the refractive indices of the Au film, the Cr adhesion layer and the CaF_x substrate were all taken account of. Using the simulated transmission spectra the positions of peaks A and B and the isosbestic point, I, were determined. The electric field simulations were carried out for the wavelengths at the two peaks ($\lambda = 3.9\mu m$ and $\lambda = 5.75\mu m$) at polarisation angles $\theta = 0$ and 90°, and at the isosbestic point $\lambda = 4.75\mu m$ for polarisation angles $\theta = 0, 45°$ and 90°.

To carry out these simulations it was necessary to know the fabricated dimensions of the arrays, as defined in 4.3a. As was previously stated, owing to fabrication process variability, the dimensions of each aperture vary and

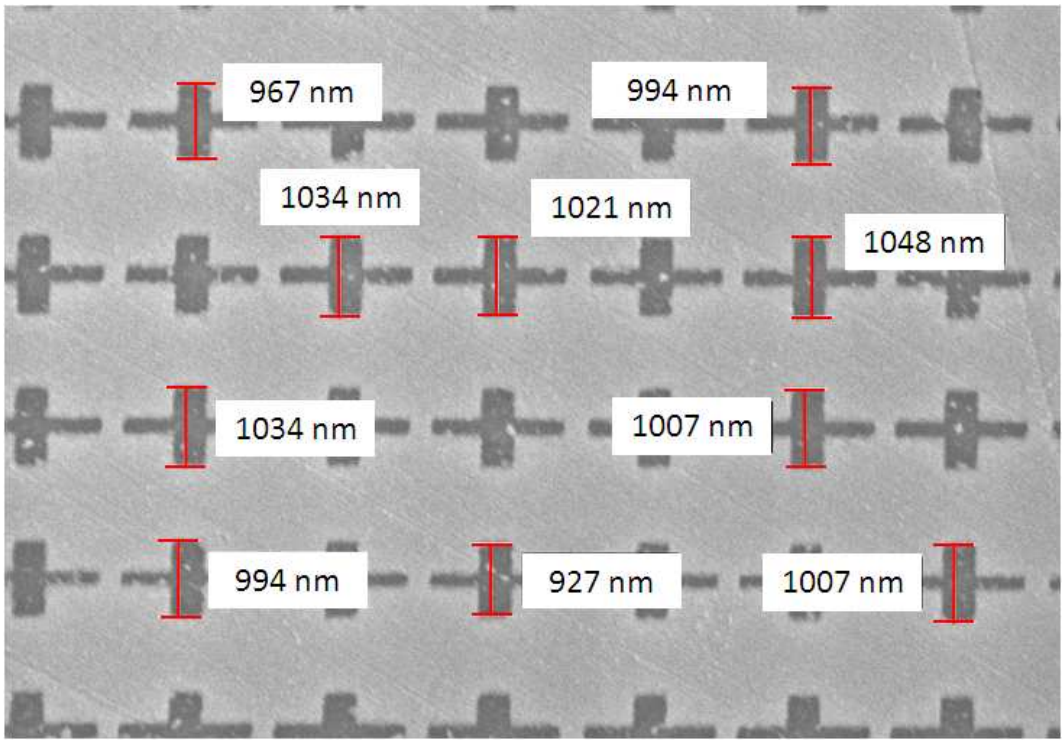

Figure 6.4: Scanning electron micrograph showing a portion of the L_y = 1003 nm array. In this image, ten measurements have been taken of the L_y dimension. These are then averaged to arrive at the mean L_y dimension. The same procedure is carried out for the other dimensions.

do not exactly conform to the dimensions used in the CAD design used to fabricate the array. Therefore measurements were taken of ten fabricated apertures in each array using scanning electron microscopy and the dimensions averaged resulting in the values already stated (Fig. 6.4).

Note also that for the array of nominally symmetric cruciform apertures fabrication tolerances led to a small degree of asymmetry, the corresponding mean values being $L_x = 1270$ nm, $L_y = 1258$ nm, $g_x = 362$ nm, and $g_y = 373$ nm. Therefore, in this case the values of L_x and L_y were averaged to arrive at a single mean value: $L_x = L_y = 1264$ nm. Similarly, the values of

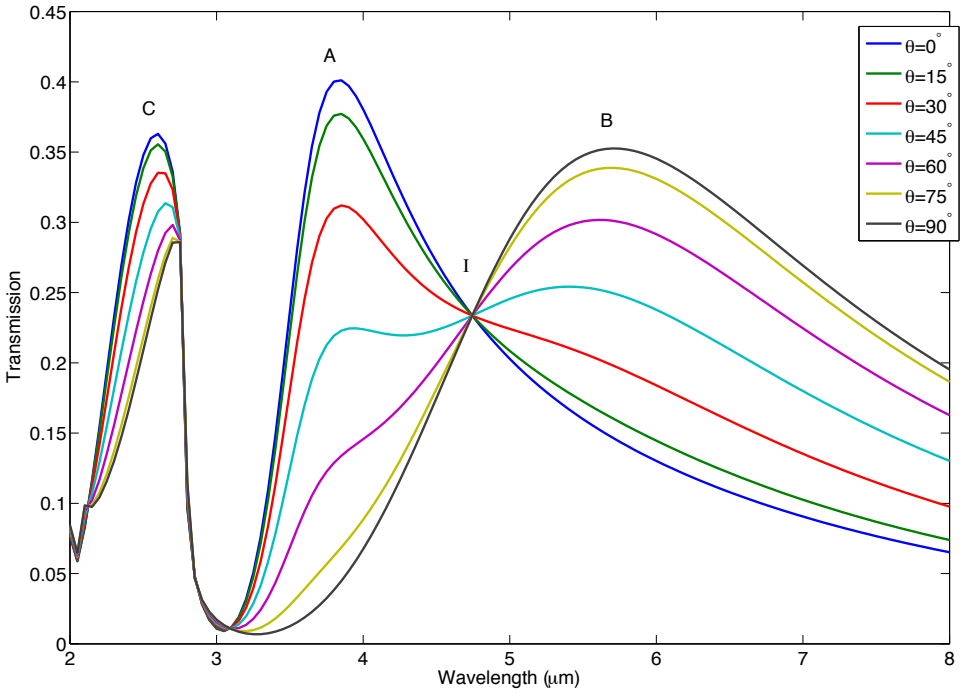

Figure 6.5: Simulated transmission spectra for an array of asymmetric cruciform apertures with $L_x = 1675$ nm, $L_y = 1003$ nm, $g_x = 418$ nm, and $g_y = 165$ nm for polarisation angles varying from $\theta = 0$ to $\theta = 90°$ in increments of 15°.

the width of the arms, g_x and g_y, were averaged to the mean value $g_x = g_y = 368$ nm.

Device simulations were carried out by Claudiu Biris using RSoft's DiffractMOD software, which implements the rigorous coupled-wave analysis method. Simulated transmission spectra for the arrays of asymmetric and symmetric cruciform apertures are shown in Fig. 6.5 and Fig. 6.6 respectively.

In these simulations it is assumed that the frequency-dependent dielectric constant of Au is described by the Drude model as expressed in equation 3.13, $\epsilon_{Au}(\omega) = \epsilon_0 \left(1 - \frac{\omega_p^2}{\omega(\omega + i\Gamma)}\right)$. In the case of Au, $\omega_p = 13.72 \times 10^{15}$ rad/s and

$\Gamma = 4.05 \times 10^{13}$ s^{-1} [119]. Since these devices operate in the mid-infrared frequency domain the contribution to the dielectric constant of inter-band effects can be neglected. It was observed, however, that in order to achieve a good agreement between the experimental data and the numerical results it was necessary to use an increased damping frequency of $\Gamma \rightarrow 1.5\Gamma = 6.08 \times 10^{13}$ s^{-1}. This fact is not surprising since it is well known that due to electron scattering into surface states the dielectric constant of metallic nanostructures depends on their size when the corresponding characteristic size is comparable to the skin depth [118].

The two transmission maxima and their polarisation-dependence, as well as the spectral location of the isosbestic point and the Wood's anomaly in the experimentally-measured spectra are well reproduced in the simulated spectra for the asymmetric apertures. An additional peak, labeled C ($\lambda = 2.6$ μm), is however observed in the simulation, which in the experimental data appears to be only slightly above the noise level. Likewise for the array of symmetric apertures, the simulation reproduces the single peak of the experimental data at $\lambda = 4.6$ μm, but also predicts the existence of an additional peak C at shorter wavelength (Fig. 6.6). This additional peak is at the same wavelength as for the asymmetric apertures. The insensitivity of the position of peak C to the detailed geometry of the unit cell suggests that it is due to extended surface plasmon polariton (SPP) resonances. Indeed, the wavelength of SPPs is given by equation 3.115, which is

$$\lambda_{\mathrm{SPP}} = (\Lambda/\sqrt{i^2 + j^2}) Re \sqrt{\epsilon_d \epsilon_{\mathrm{Au}}/(\epsilon_d + \epsilon_{\mathrm{Au}})} \tag{6.1}$$

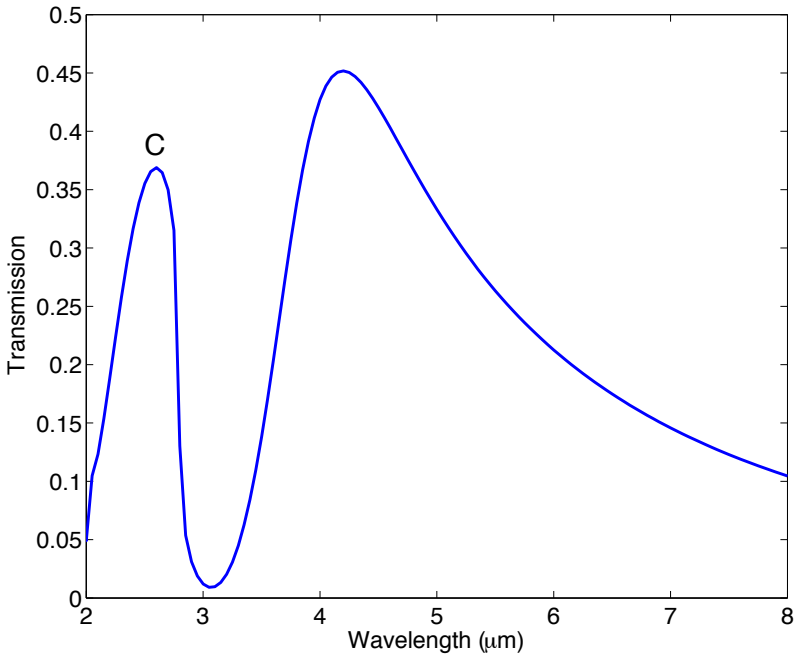

Figure 6.6: Simulated transmission spectra for an array of symmetric cruciform apertures with $L_x = L_y = 1264$ nm, $g_x = g_y = 368$ nm, and $g_y = 165$ nm for polarisation angles varying from $\theta = 0$ to $\theta = 90°$ in increments of 15°. All the curves lie on top of each other

which implies that for Au-air and Au-CaF_2 interfaces the SPP wavelength is $\lambda_{\mathrm{SPP}} = 2.005$ μm and $\lambda_{\mathrm{SPP}} = 2.807$ μm, respectively. Since $|\epsilon_{\mathrm{Au}}| \gg \epsilon_d$, λ_{SPP} is only slightly larger than λ_{W}. The extended SPP resonances are significantly weaker in our experimental measurements, as compared to those in simulations, presumably due to losses resulting from the surface roughness of the evaporated metal film [31] and low sensitivity of the detector in the lower-wavelength spectral domain.

Peaks A and B, however, result from local surface plasmon resonances in the shorter and longer arms of the asymmetric aperture, respectively.

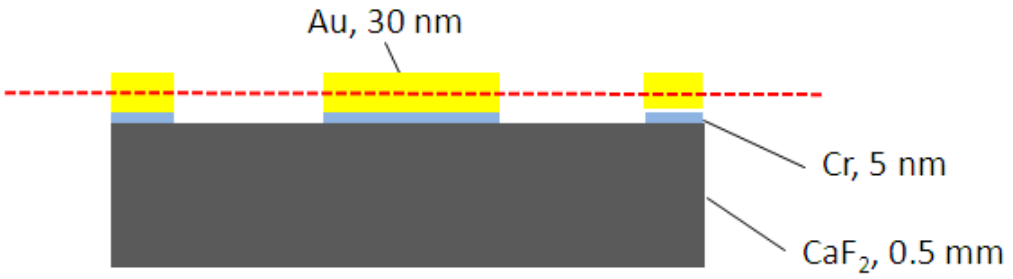

Figure 6.7: The simulated field profiles were taken at a depth of half the thickness of the Au film at a position represented by the red dotted line.

More specifically, they correspond to the cut-off wavelength of the waveguide modes supported by the cruciform apertures. This interpretation is further supported by the fact that the simulated spectra for the symmetric apertures are polarisation-independent as in this case the two modes are degenerate. Importantly, since the properties of these modes are defined entirely by the shape of the apertures, the corresponding transmission depends only on the optical coupling between these modes and the incoming plane wave and as such it is not affected by the roughness of the top surface of the metallic film.

6.3 Field Profile Simulations

In order to confirm our interpretation that peaks A and B correspond to LSP resonances, Claudiu Biris simulated the field distributions within the apertures using eight diffraction orders. The field profiles correspond to a depth of half of the thickness of the Au film (Fig. 6.7). The simulation images in Fig. 6.8 show the field distributions at polarisation angles of $\theta = 0$ and $\theta = 90^{\circ}$ at the two transmission peaks.

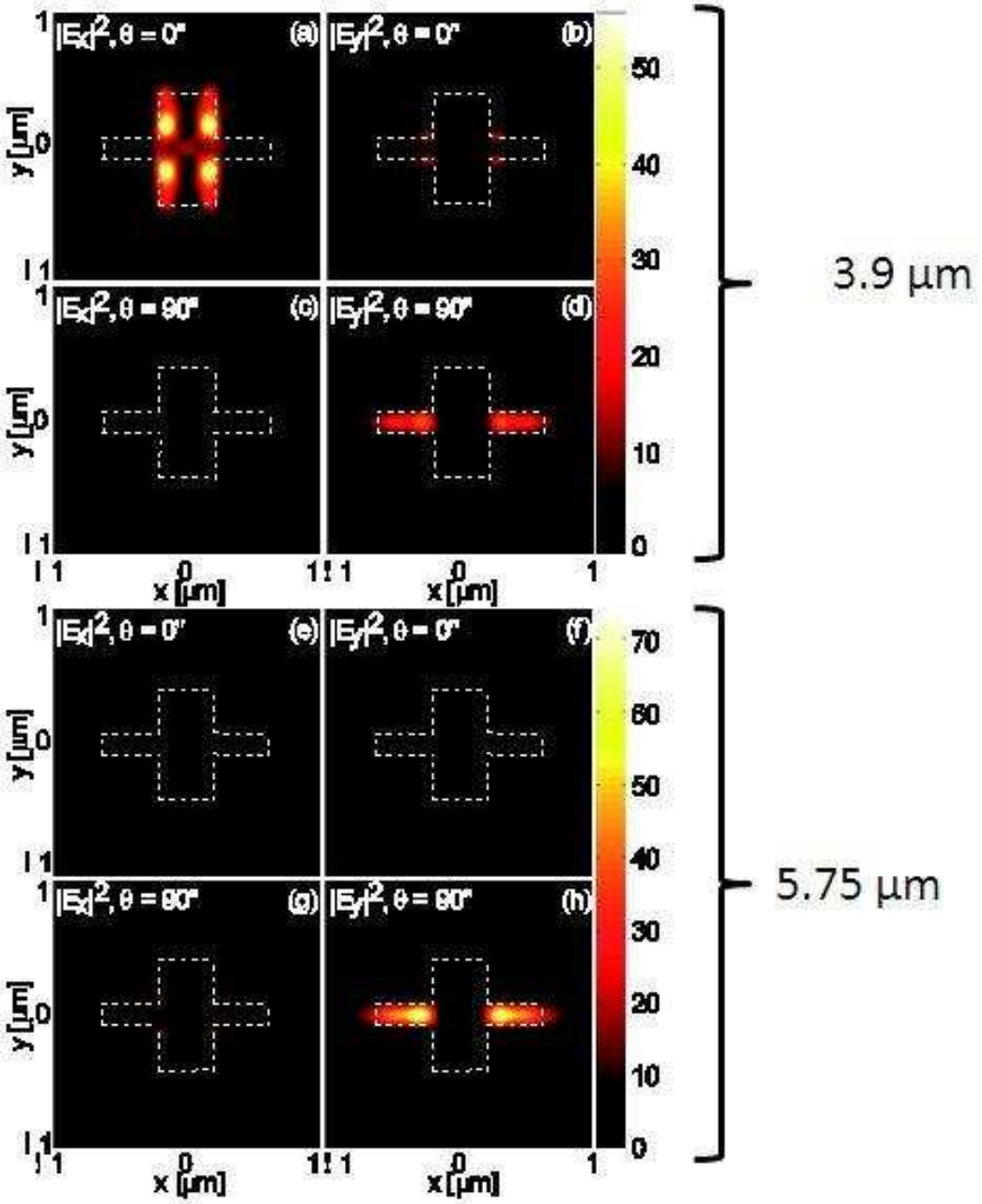

Figure 6.8: Simulated spatial profiles of the electric field for $\theta = 0$ and $\theta = 90°$. Panels a, b, c, and d show the field profiles at a wavelength of 3.9 μm (corresponding to peak A in Fig. 6.2), while panels e, f, g, and h show the field profiles at a wavelength of 5.75 μm (corresponding to peak B in Fig. 6.2). The electric field is normalized to the amplitude of the incident plane wave.

The field profiles in panels (a)–(d) in Fig. 6.8 illustrate the in-plane electric-field components at $\lambda = 3.9$ μm (corresponding to peak A), while panels (e)–(h) in this same figure show the field profiles at $\lambda = 5.75$ μm (corresponding to peak B). From these simulations it is clear that peak A occurs due to the resonant excitation of a waveguide mode that is primarily polarized transverse to the shorter, y-oriented arm of the aperture (as shown in Fig. 6.8a). Similarly, peak B corresponds to the cut-off wavelength of a waveguide mode with polarisation primarily transverse to the longer, x-oriented arm (as shown in Fig. 6.8h). Switching between these two modes is accomplished by changing the polarisation of the incident plane wave. It should be noted that these LSP resonances do not correspond to the cut-off modes of the separate arms of the cruciform apertures, as in this case the cut-off wavelength would obey the relation $\lambda_c < 2\max(L_x, L_y)$ (since this allows half a wavelength to fit precisely within the length of the arms). Importantly, this result suggests that the wavelength of the transmission peaks can be readily tuned over a wide spectral range by simply changing the shape of the apertures.

Fig. 6.9 shows the in-plane electric field distributions at the isosbestic point, $\lambda = 4.75$ μm, at polarisation angles of $\theta = 0$, $\theta = 45°$, and $\theta = 90°$. Unlike the fields corresponding to transmission maxima, the fields calculated at the isosbestic point do not have a predominant polarisation state, which means that irrespective of the polarisation of the incident wave both waveguide modes are excited. This phenomenon also explains why such an isosbestic point exists. This can be further explained in the following way. The following two equations

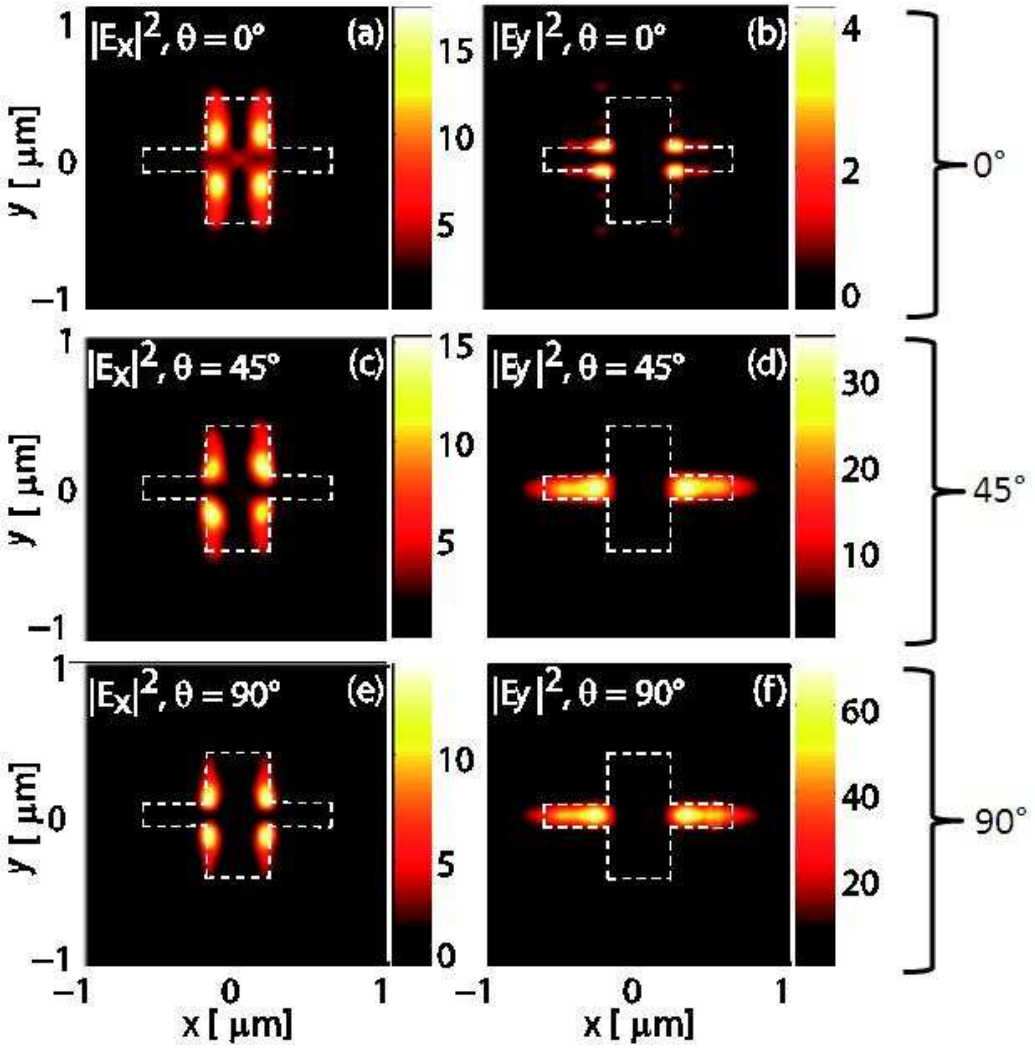

Figure 6.9: Simulated spatial profiles of the electric field at the isosbestic point ($\lambda = 4.75$ μm) for $\theta = 0$, $\theta = 45°$, and $\theta = 90°$. The electric field is normalized to the amplitude of the incident plane wave.

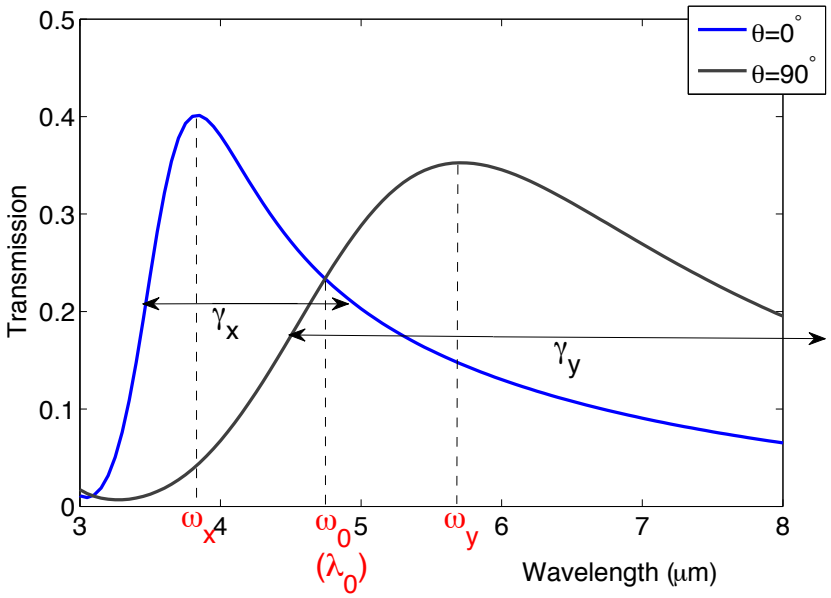

Figure 6.10: At $\lambda = 0$ and $\lambda = 90°$ the full width half maximum of the two curves represent the damping terms γ_x and γ_y respectively. The plasmon resonances occur at ω_p^x and ω_p^y.

$$t_x(\omega) \sim \frac{A_x}{\omega - \omega_p^x + i\gamma_p^x} \tag{6.2}$$

$$t_y(\omega) \sim \frac{A_y}{\omega - \omega_p^y + i\gamma_p^y} \tag{6.3}$$

represent the E-fields of transmission in the x and y directions, where A is the amplitude, ω_p is the plasmon frequency and γ is the damping term (see Fig 6.10).

The transmission is equal to the square of the electric field, and therefore

$$T_x(\omega) = |t_x(\omega)|^2 = \frac{|A_x|^2}{(\omega - \omega_p^x)^2 + (\gamma_p^x)^2} \tag{6.4}$$

and

$$T_y(\omega) = |t_y(\omega)|^2 = \frac{|A_y|^2}{(\omega - \omega_p^y)^2 + (\gamma_p^y)^2} \tag{6.5}$$

If there is a transmission frequency at which T_x and T_y are equal, i.e.

$$T_0(\lambda_0) = T_x(\lambda_0) = T_y(\lambda_0) \tag{6.6}$$

then it follows that for any value of polarisation at this value of ω

$$T_0(\lambda_0) = T_0(\lambda_0)cos^2\theta + T_0(\lambda_0)sin^2\theta \tag{6.7}$$

Therefore at this value of ω the transmission is independent of the polarisation angle θ and its amplitude is constant. Going back to the analogy with physical chemistry, we can view the plasmonic metasurface as a 2D distribution of meta-molecules whose polarisability, at the isosbestic point, is independent of polarisation.

6.3.1 Dependence Of Transmission Spectra on Unit Cell Geometry

In order to further validate the interpretation of the physical origin of the resonant transmission peaks, spectra were experimentally measured for an ensemble of asymmetric cruciform aperture arrays, in which one geometrical parameter (in this case the length of the shorter arm, L_y), is systematically varied. A total of seven additional arrays were fabricated. Again FIB was used to mill these arrays using the same substrate and film materials and

thicknesses as before. Each of the seven arrays had 15×15 unit cells and a periodicity of $\Lambda = 2$ μm. The mean and standard deviation of L_y for each array were determined using SEM. The transmission spectra for $\theta = 0$, $\theta = 45°$, and $\theta = 90°$ are displayed in Fig. 6.11.

The extracted spectral location of the resonant peaks A and B, as well as that of the isosbestic point I, are plotted in Fig. 6.12. As expected, peak A (the shorter wavelength peak) shifts to longer wavelengths as the length, L_y, of the shorter arm increases, whereas peak B (the longer wavelength peak) is invariant with L_y. Also, as the length of L_y increases, the cruciform apertures tend toward symmetry in L_x and L_y. Thus peaks A and B, and the isosbestic point I, tend to converge toward a single peak with the amplitude of peak A increasing (due to an increasing area of the optical mode) and the amplitude of peak B decreasing. Also plotted in Fig. 6.12 are the results of our simulations for varying L_y. The values of L_x, g_x, and g_y used in the simulations are given by the mean of all these values across all the fabricated arrays, as measured by SEM. These values are $L_x = 1645$ nm, $g_x = 418$ nm and $g_y = 165$ nm.The results of our numerical simulations agree well with the experimental data, confirming our physical interpretation of the features observed in the experimental spectra.

An additional set of simulations was carried out to determine the effect of changing the values for g_x 6.13. These simulations show that the wavelength of the resonances are not significantly changed by varying the value of g_x. However, a small increase in the transmission intensity is observed for increasing g_x. Thus the most important factor for influencing the wavelength of the transmission resonances is the length of the aperture arms, with longer

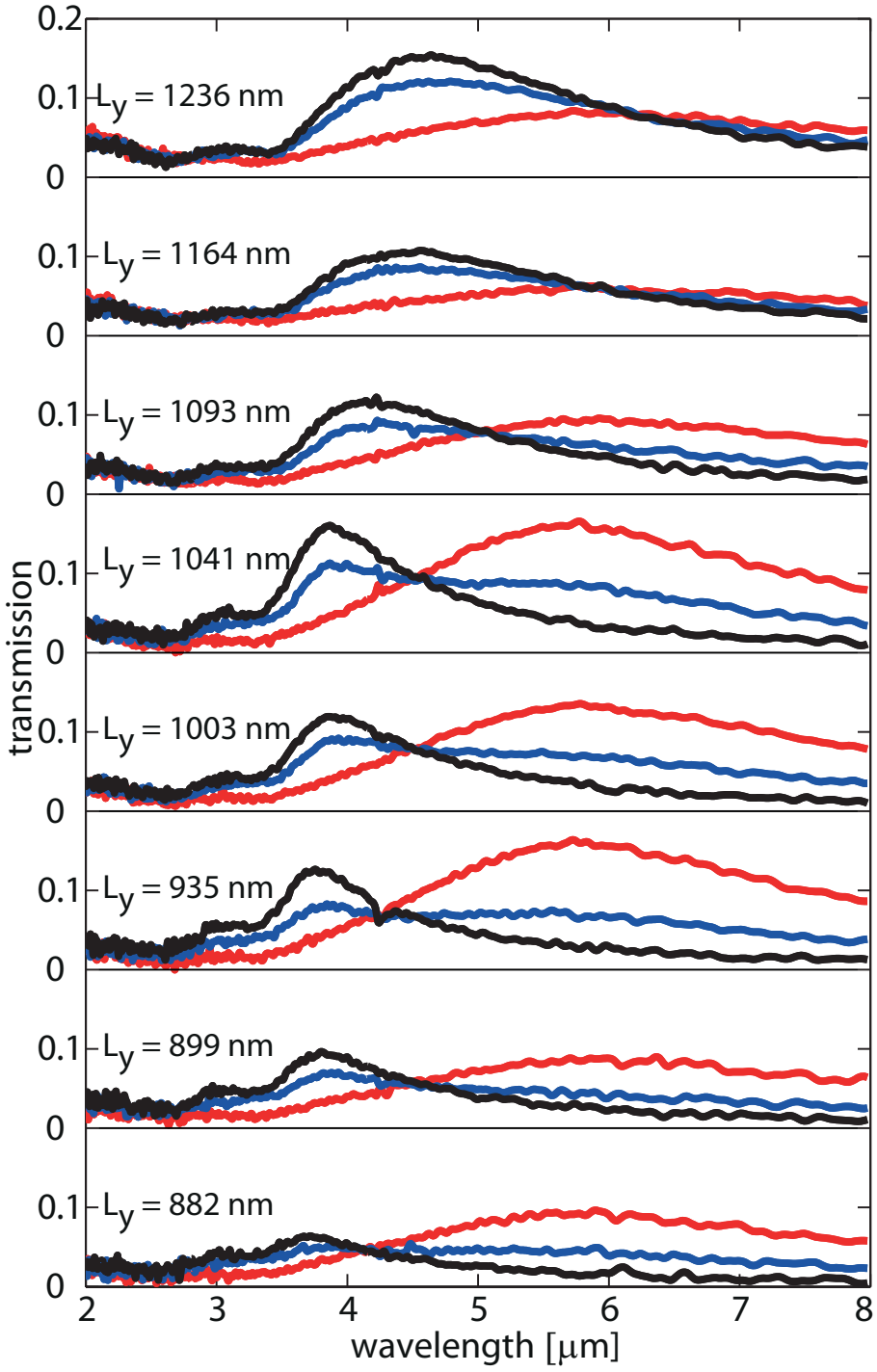

Figure 6.11: Experimentally measured transmission spectra for all fabricated arrays of asymmetric cruciform apertures at polarisation angles of $\theta = 0$ (black), $\theta = 45°$ (blue), and $\theta = 90°$ (red). The mean values of the other dimensions are $L_x = 1645$ nm, $g_x = 418$ nm and $g_y = 165$ nm.

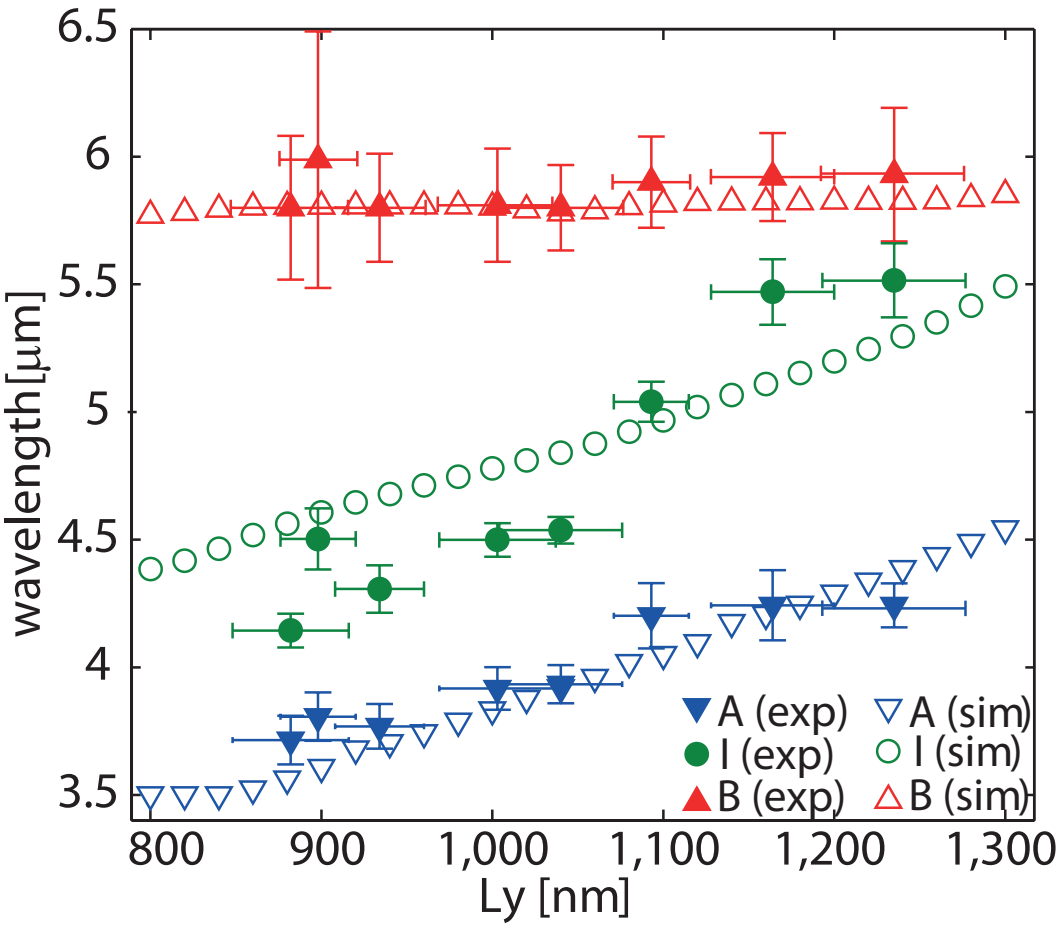

Figure 6.12: L_y-dependence of the wavelength of the LSP resonances A (blue) and B (red), and the isosbestic point I (green). Filled points are experimental data; unfilled points are data from simulations. Error bars in L_y correspond to the standard deviation of the fabricated device dimensions.

transmission wavelengths occurring for longer aperture arms.

Additionally, if we vary the refractive index of the substrate between values of n=1 and n=1.8 we see that as the value of the refractive index increase, the wavelength of the plasmon resonance is red shifted (see Fig 6.14). This is to be expected because of equations 3.30 and 3.31. We also see that the intensity of the transmission reduces with increasing refractive index owing to increasing reflectivity caused by the increasing difference between the refractive index of the substrate and the refractive index of the air in the apertures.

6.4 Reflection and Absorption

To further investigate the properties of the arrays, reflection spectra were taken of the $Ly = 1003$ nm array and this was used, in conjunction with the transmission data to obtain absorption data. This was arrived at by using the equation

$$A = 1 - (T + R) \tag{6.8}$$

where A is the absorption, T is the transmission and R is the reflection.

The spectra for all three sets of data are shown in Fig. 6.15. The measured reflection spectra are qualitatively anticorrelated with the transmission spectra, with clear reflection minima at the wavelengths of the transmission peaks A and B. For both the reflection and absorption spectra there is an isosbestic point, its wavelength being blue-shifted with respect to that of the

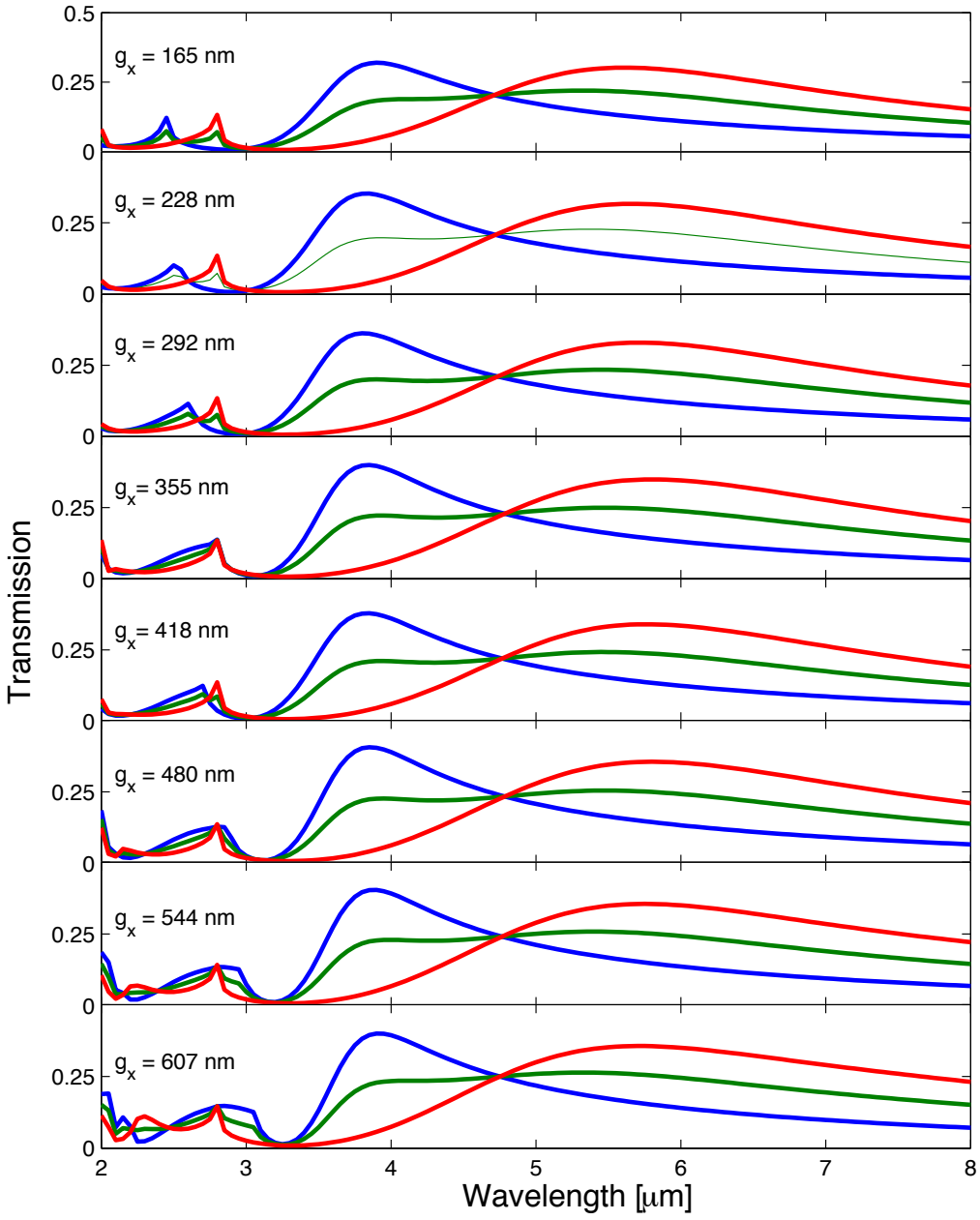

Figure 6.13: Transmission simulations for varying $g_x$dependence of the wavelength of the LSP resonances for polarisation angles of $\theta = 0$ (black), $\theta = 45°$ (blue), and $\theta = 90°$ (red). The values of the other dimensions are $L_x = 1645$ nm, $L_y = 1003$ nm and $g_y = 165$ nm. The wavelength of the resonances does not significantly change as g_x is varied. However, there is a small increase in transmission intensity with increasing g_x.

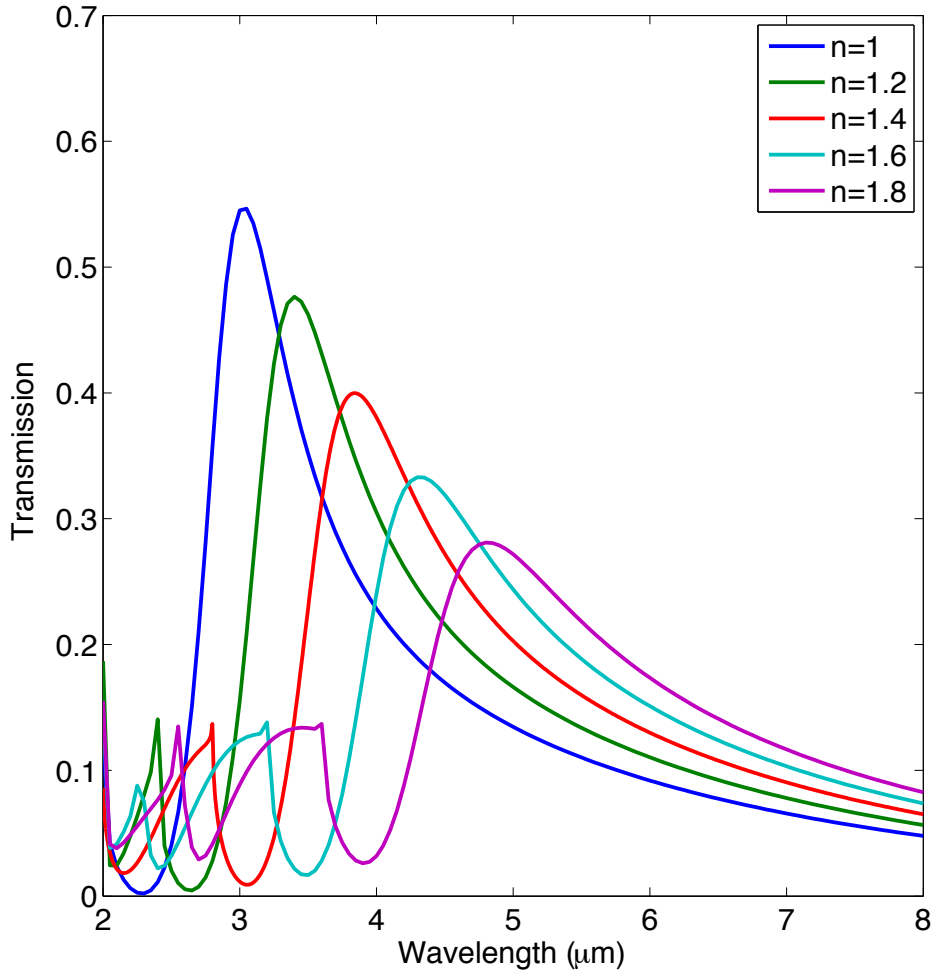

Figure 6.14: Transmission simulations for varying values of the refractive index for an incident polarisation of $\theta = 0$. The wavelength of the plasmon resonance is red shifted with increasing refractive index.

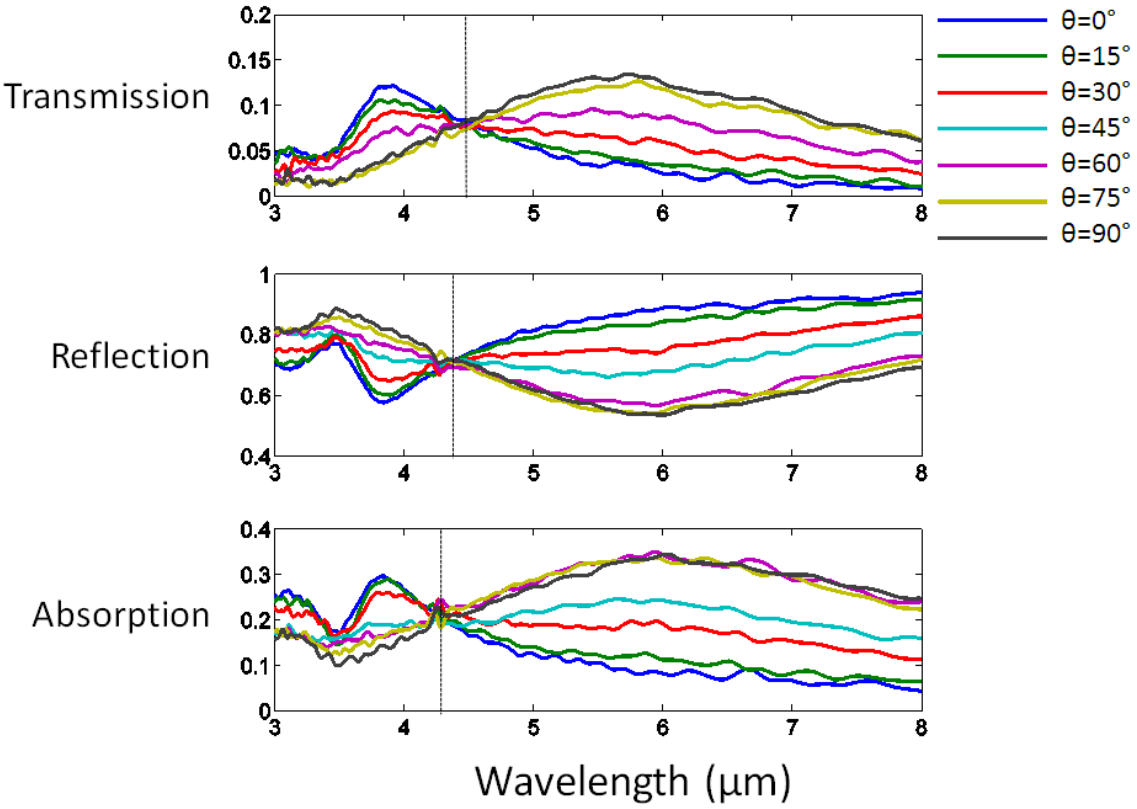

Figure 6.15: The experimental data for transmission, reflection and absorption for the L_y =1003 nm array shows that there is an isosbestic point for all three sets of data and that the position of the isosbestic point changes.

isosbestic point in the transmission spectra. The isosbestic point of the transmission, reflection and absorption spectra is at the wavelength $\lambda = 4.53\mu m$ $\lambda = 4.36\mu m$ and $\lambda = 4.32\mu m$, respectively.

Simulation confirm that the isosbestic point is different for transmission, reflection and absorption (Fig. 6.16)

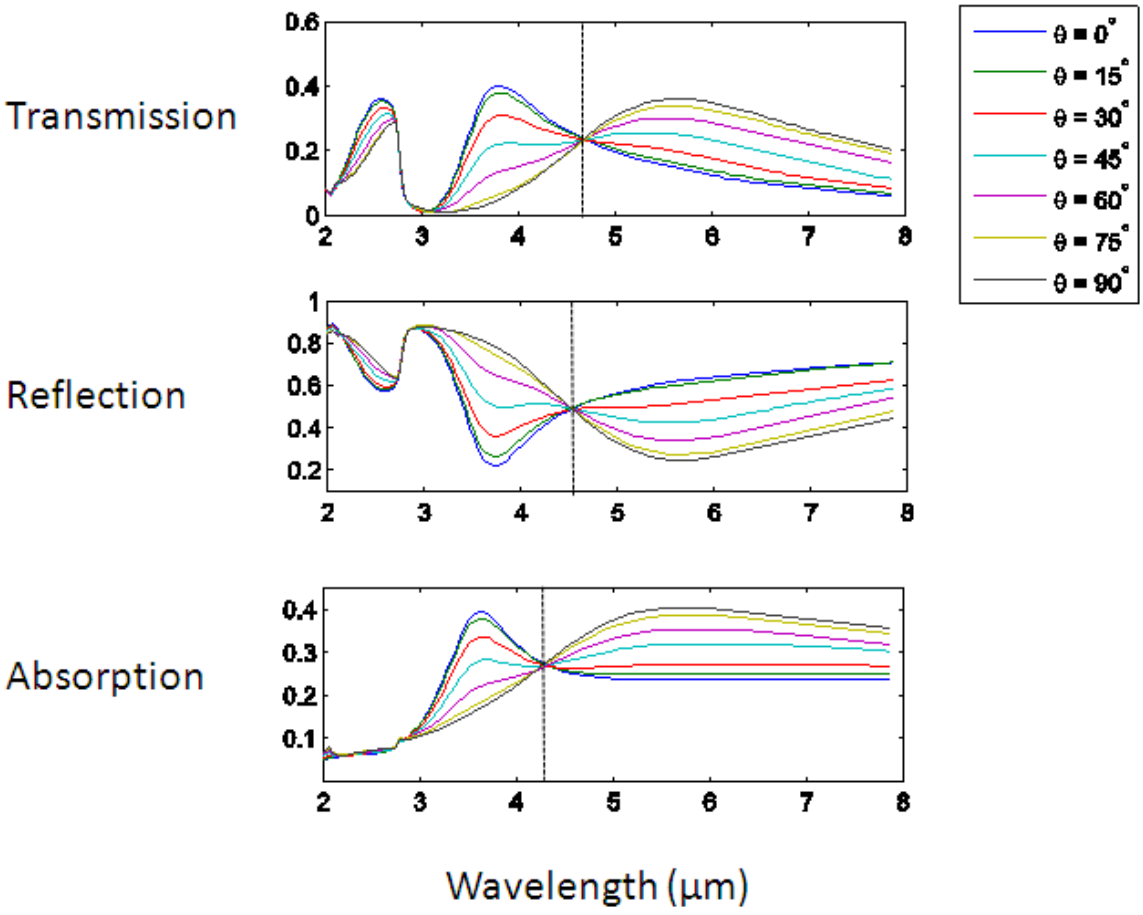

Figure 6.16: Simulation data for transmission, reflection and absorption show that the isosbestic point changes position. These occur at $\lambda = 4.75$ μm, 4.55 μm and 4.35 μm respectively.

6.5 Array Induced Rotation of Polarisation

An intriguing piece of additional research was carried out using a second polariser as an analyser (see Fig. 6.17). This was used to determine the polarisation state of the light transmitted through the arrays. The polariser was set to $\theta = 45°$ and the analyser was rotated through $\alpha = 0$ to $\alpha = 90°$ in increments of 22.5°. If the incident polarised beam was unchanged by the array, then the result would show a single wavelength for the transmission peak, with a maximum transmission at $\alpha = 45°$. However, the spectra show two distinct peaks occurring at $\alpha = 0$ and $\alpha = 90°$ respectively, which indicate that the arms of the array are polarizing the incoming beam (Fig. 6.18). These results stimulated further investigations of the arrays' polarising properties.

A series of transmission spectra was obtained for incident polarisations ranging from $\theta = 0$ to 90° in steps of 15°. For each of these polarisations an analyser was used to obtain spectra at analyser angles ranging from $\alpha = 0$ to 180° in increments of 5°. For this set of experiments it was therefore necessary to correct for the transmission characteristics of the analyser. This was carried out by removing the sample, aligning the analyser with the polariser and taking a transmission spectrum. The transmission data for the sample were then renormalised by dividing by this second background data.

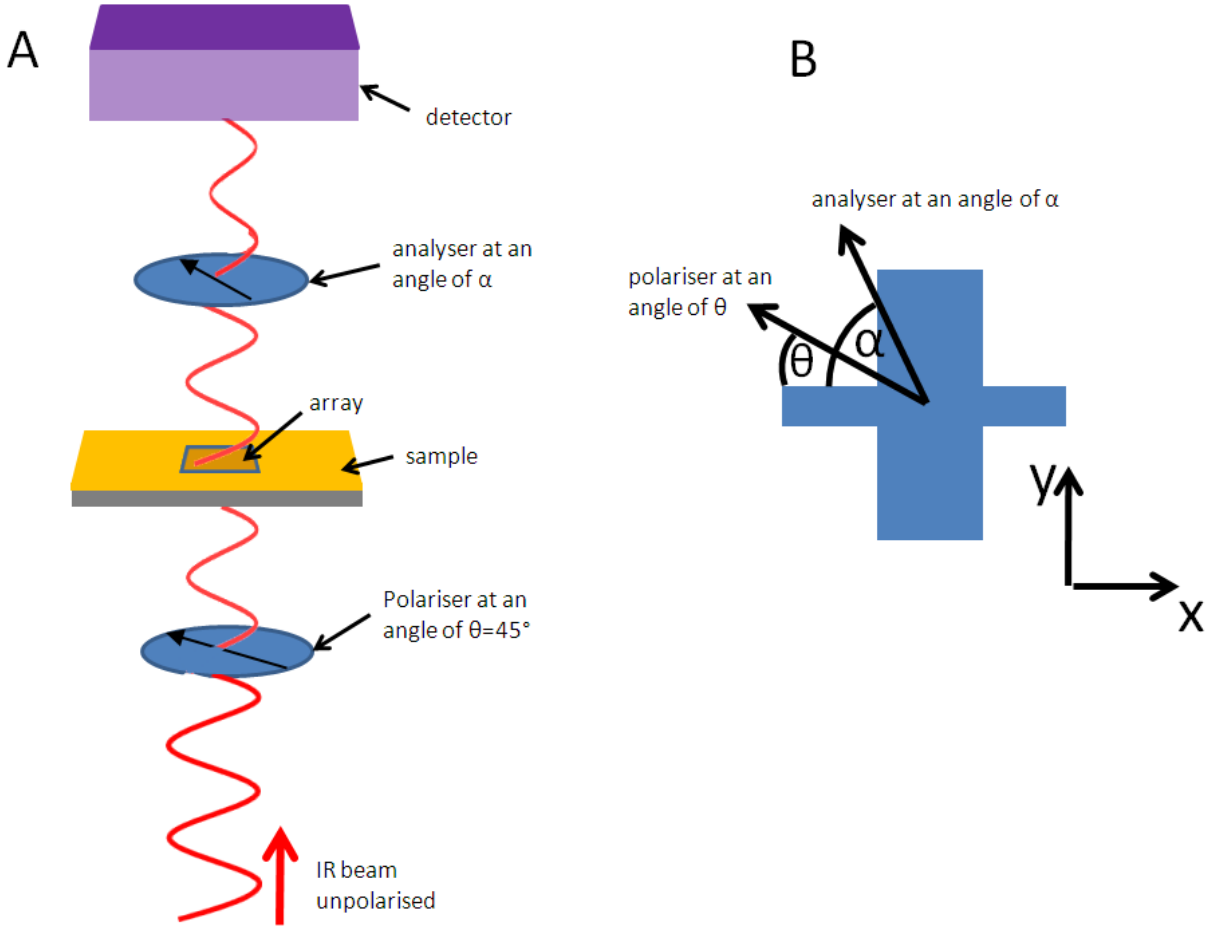

Figure 6.17: A) Schematic diagram showing the arrangement of the polariser and analyser. The IR beam that exits the array is normally incident upon an analyser oriented at an angle of α to the negative x axis. B) Plan view of the analyser orientation showing that the angle of the analyser is measured relative to the negative x-axis.

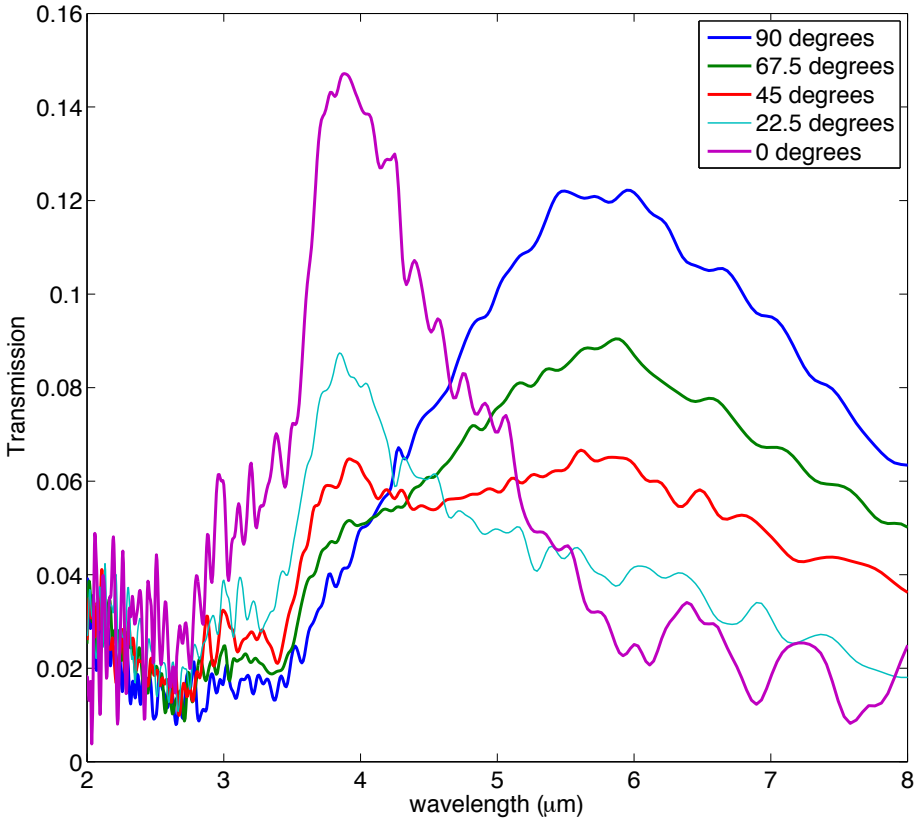

Figure 6.18: This data represents transmission through the $L_y = 1003$ nm array where the polariser is fixed at $\theta = 45°$ and spectra are taken for different angles of the analyser between $\theta = 0°$ and $\theta = 90°$ in 22.5° increments.

A set of simulations was carried out using RSoft to obtain comparable data. RSoft provides only information for the E fields in the x and y directions and their phase difference, whereas the FTIR provides transmission data but no information regarding phase. If x and y components of the E-field do not reach their maxima and minima at the same time then they have a phase difference.The phase information is important for determining whether a beam is linearly, circularly or elliptically polarised. This is done using the

Stokes parameters and the polarisation ellipse. If there is no phase difference, then the beam is linearly polarised. If the phase difference is 90°, then the beam is circularly polarised, and for any other phase difference the beam is elliptically polarised. Therefore, the lack of phase information on the FTIR poses a problem for experimental verification.

Using equation 3.81, however, it was possible to compare the simulation data with experimentally obtained data (Fig 6.19). This was carried out for the wavelengths of peak A and peak B for 7 incident polarisations, $\theta = 0$ to $\theta = 90°$ in 15° steps. There is a correlation between the experimental and simulation data for the position of the maxima and minima for the different polariser angles. It is also clear that the maxima occur at analyser angles that are not the same as the polariser angles, implying that the array is changing the polarisation state of the incoming beam. Also, if the transmitted beam was linearly polarised then one would expect to see the transmission through the analyser go to zero when the analyser was positioned perpendicular to the beam transmitted through the array. Since in both the simulation and experimental data the transmission for some polarisations does not go to zero for any angle of the analyser, this implies that in these instances the output beam is elliptically polarised.

Using the simulation data we can look at the analyser angles at which the maxima occur and compare these with the polariser angles. The difference between the two can be plotted against the input polarisation for several different wavelengths (Fig 6.20). We see that the maximum change in polarisation occurs for the wavelength $\lambda = 3.9\mu m$ (Peak A) at a polarisation of around 55-60°, where there is a shift of around 36°. It is also clear that the

difference in polarisation changes from positive to negative as we move from peak B to peak A. For the isosbestic point the difference shifts from negative to positive, with a shift of zero around 50° polarisation. Using the experimental data shown in Fig. 6.19 it was possible to estimate the polarisation position of the transmission peaks for the wavelengths of Peak A and B and find the difference between this and the incident polarisation. Comparing this data with the simulation data for the polarisation shift in A and B we see that the experimental data confirms the simulation (Fig. 6.21).

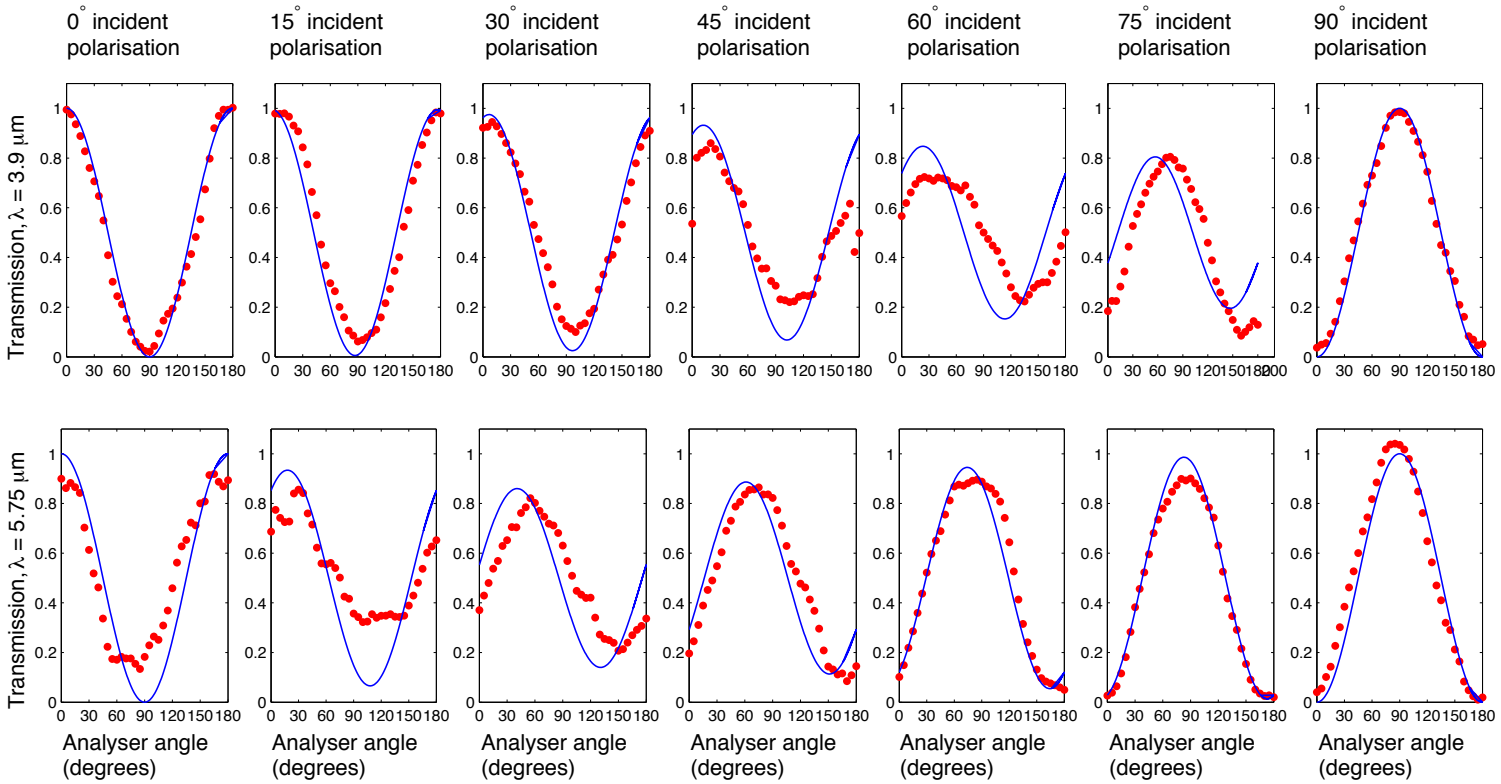

Figure 6.19: Experimental and simulation data for the transmission through an analyser for the $L_y = 1003$ array. Red dots represent experimental data and blue lines are simulation data. Data was obtained for wavelengths $\lambda = 3.9\mu$m and $\lambda = 5.75\mu$m, corresponding to peaks A and B, for 7 polarisations.

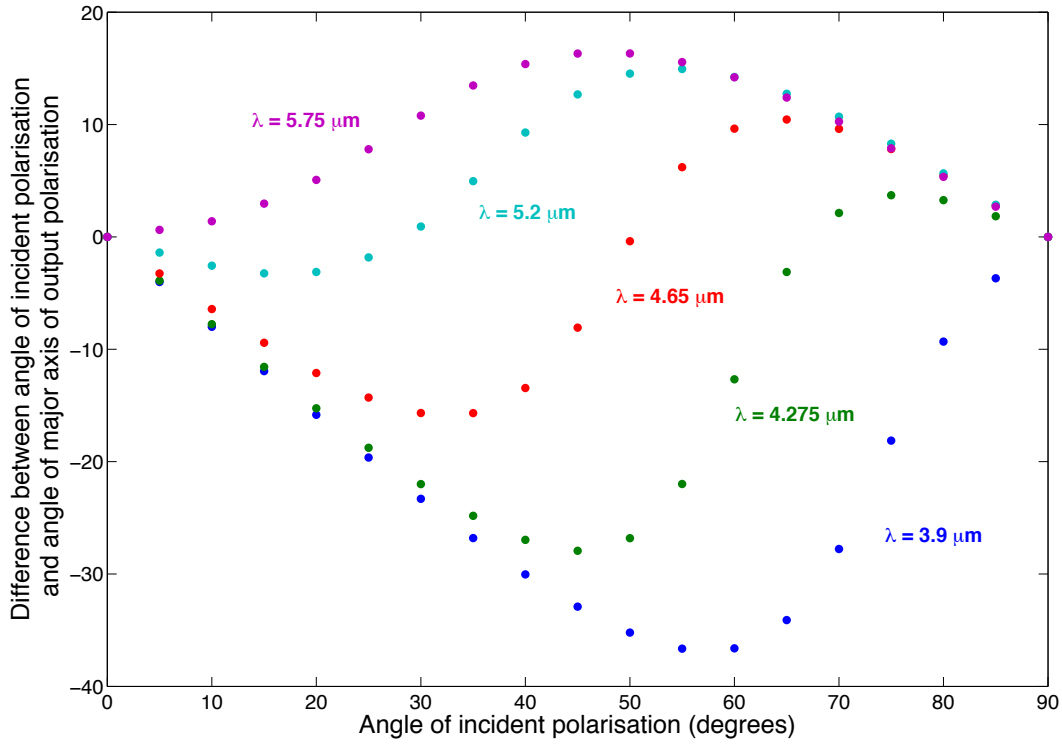

Figure 6.20: Simulation data showing the difference in polarisation between the incident beam and the major axis of the output elliptical polarisation. We see that the difference in polarisation shifts from positive to negative as the wavelength increases. For peaks A and B the shift in polarisation is entirely positive and negative respectively. At wavelength between A and B there are input polarisations at which the shift is positive and input polarisations where the shift in negative. In these cases there is also an incident polarisation for which the angle of the major axis of the transmitted polarisation remains unchanged.

It is also possible to use the simulation data in conjunction with the equations of the polarisation ellipse (Eq. 3.92) and the Stokes parameters (Fig. 3.106) to determine the ellipticity of the transmitted waves (Eq. 6.22). These simulations show that the transmitted wave changes from being linearly polarised when the polariser is parallel to either the x or y direction. Between

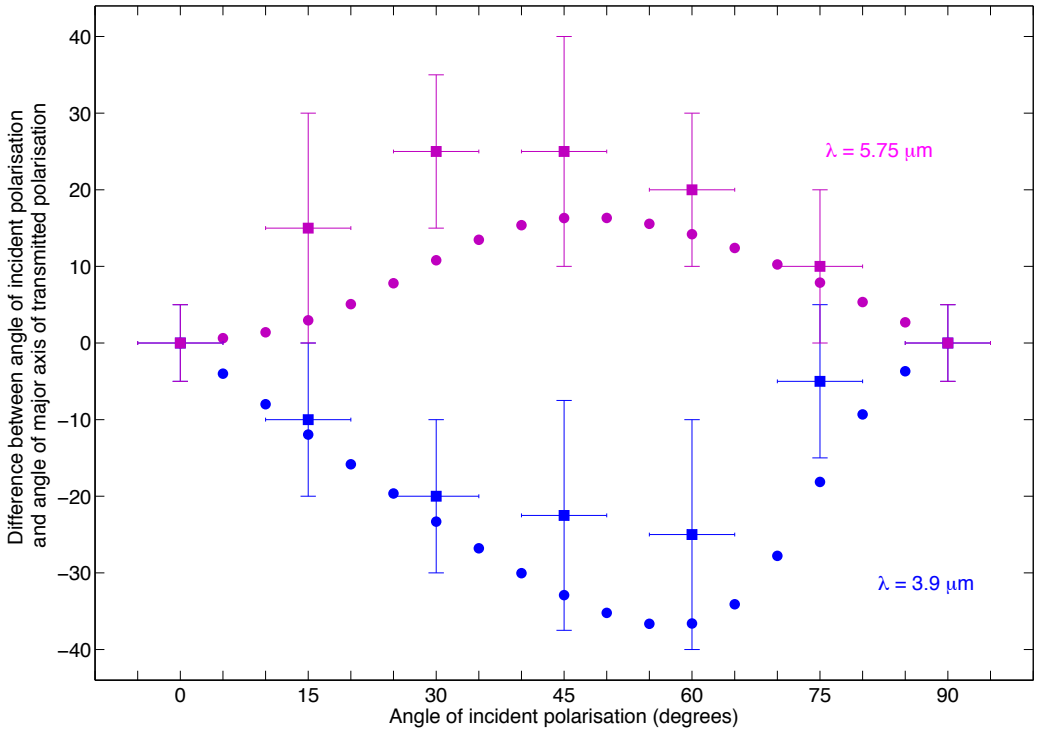

Figure 6.21: Simulation data (solid circles) and experimental data (solid squares) showing the difference in polarisation between the incident beam and the major axis of the output elliptical polarisation for the wavelengths of peaks A and B (3.9μm and 5.75μm respectively) The experimental data confirms the general trend in polarisation shift.

these orientations the ratio of the major to minor axis of the ellipse decreases as the polariser is moved anticlockwise from being parallel to x and then increases again as it is moved toward the y axis. Also, using Stokes equations it is possible to infer the sense of the polarisation for different wavelengths. For $\lambda = 3.9, 4.75$ and $5.75\mu m$, the polarisations are all clockwise. To measure the ellipticity and sense of polarisation experimentally would have involved the use of additional polarisers such as quarter waveplates, which our experimental setup did not accommodate. For an wavelength of $\lambda = 3.9\mu m$ and an incident polarisation of around $\theta = 60^\circ$ there is a rotation of the major axis of around 1° per nm in the z direction through the Au film.

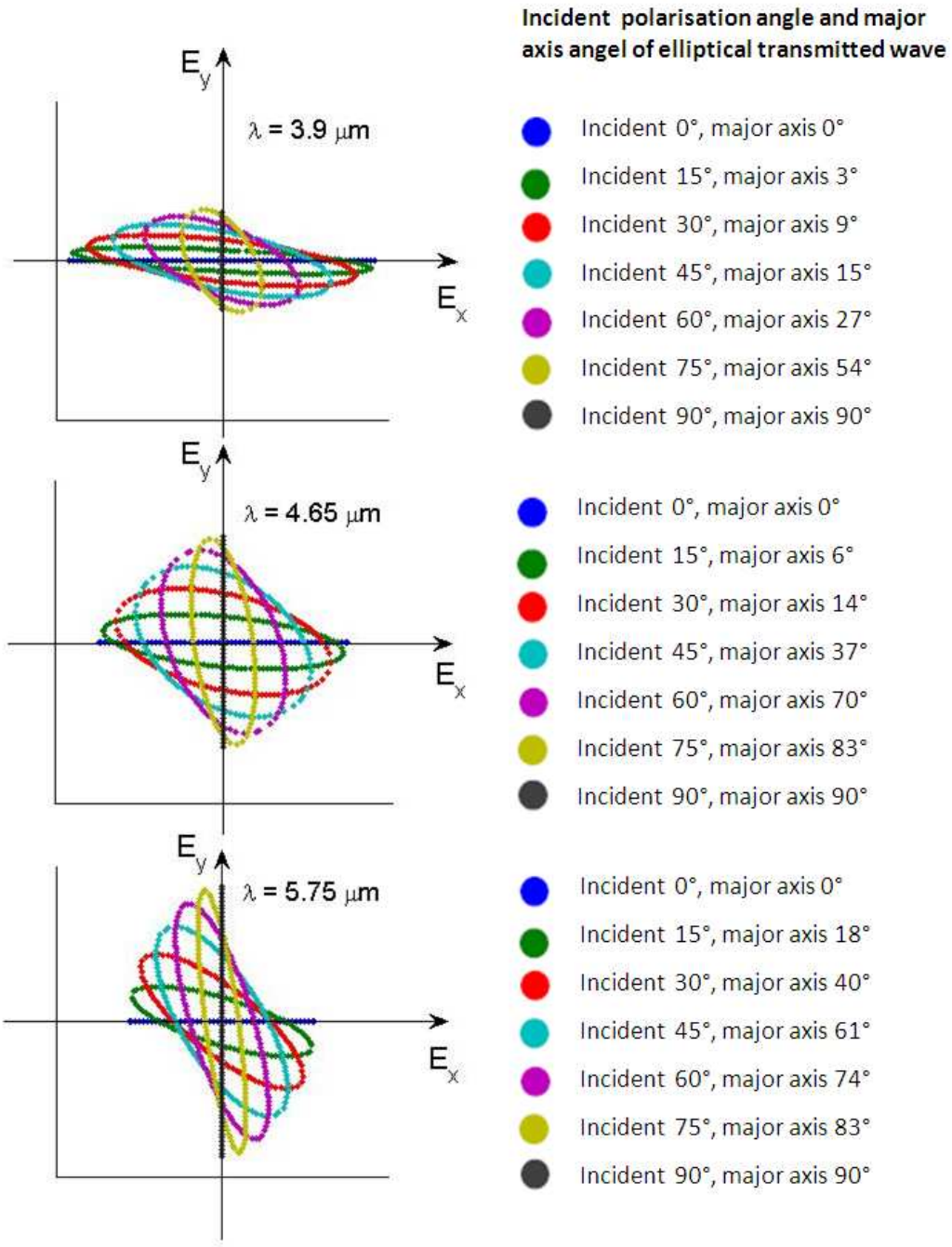

Figure 6.22: The form of the elliptical polarisation derived from simulations for three wavelengths corresponding to Peak A, the isosbestic point, and peak B respectively. For each of these the elliptical polarisation was calculated at seven incident polarisations.

Chapter 7

Conclusions

Arrays of subwavelength asymmetric cruciform apertures have been fabricated that display extraordinary transmission in the mid infrared region. These arrays display a polarisation dependence such that the transmission characteristics of each array display two distinct peaks that alternately vary in intensity as the incident polarisation is changed. Each array also displayed a wavelength at which the transmission was invariant - the isosbestic point. For the fabricated array with dimension $L_y = 1003nm$ the two transmission peaks occurred around $\lambda = 3.9\mu m$ and $\lambda = 5.75\mu m$. The isosbestic point occurred at $\lambda = 4.46\mu m$. These findings suggest that the functionality of our proposed plasmonic nanostructures can be greatly enhanced by interspersing arrays whose unit cell consist of cruciform apertures with different sizes or, more generally, apertures with different shapes. Since the transmission maxima of the arrays is determined solely by the frequency of the corresponding LSP resonances, the spectral optical response of these plasmonic nanostructures can be tailored for specific applications, allowing one to explore new designs of frequency-agile metasurfaces with enhanced functionality. Equally important the conclusions of our work can be readily extended to the technically relevant 1.55 μm wavelength region by simply scaling the size of the apertures. In addition, these arrays of asymmetric cruciform apertures show the surprising ability to rotate the polarisation of light by more than 30° over a thickness of only around 30 nm. Usually one would expect such a change in polarisation to occur only over many microns. For example, to achieve a $\frac{\pi}{2}$ shift in polarisation for $\lambda = 3.9\mu m$ using a birefringent quarter wave plate would require a minimum material thickness of around $170\mu m$ [120]. Thus these devices have possible applications in optical systems where

nanoscale polarisers would be necessary. In similar arrays of subwavelength apertures a change in polarisation has been observed but only when the apertures are themselves chiral or when the incident beam is not normal to the array surface. By changing the dimensions of the apertures in our arrays it would be possible to engineer a specific change in polarisation for a particular wavelength and incident polarisation.

7.1 Further Work

The following section will outline a number of intended developments of this research, both in the near term and long term. Broadly, this work can be divided into further exploration of existing arrays, investigation of the mechanisms involved in losses, and fabrication and characterisation of new arrays to explore phenomena such as second harmonic generation.

In order to understand further the causes of losses in the arrays it is necessary to understand the role of gallium ion implantation in the CaF_2 substrate. To do this, a series of 10 circular areas of the substrate, each $40\mu m$ in diameter could be exposed to the FIB in increasing dosages. These would range from 10 pC/μm^2 to 100 pC/μm^2. A similar exercise could be carried out for a 30 nm layer of Au (and a 5 nm adhesion layer of Cr) on the CaF_2 substrate. The transmission through these two sets of circular areas would then be individually tested using FTIR and the results analyzed to determine how, and whether, ion implantation affects transmission.

Further investigation into the phenomena causing the resonances in the arrays is also necessary. This will help to enhance understanding of the

waveguide and plasmonic behaviour in the apertures. This could involve further simulations and use of SNOM to investigate the apertures near field distribution.

It would also be useful to understand the effect on transmission of changing the angle of incidence of the MIR beam on the arrays. To achieve this it would be necessary to fabricate a tilting stage that can fit within the tight optical arrangement of the microscope.

It would be useful also to explore the application of these arrays as biosensors and to see if the polarisation dependence of transmission can be used to increase the functionality of a single biosensor device. Such a device could be included within a microfluidic structure, such as that, for example fabricated by Yang *et al* [8] but would require the inclusion of a polariser. By producing several arrays with different aperture dimensions it would be possible to increase the capacity for multiplexing that these researchers demonstrated.

Additionally, it would be interesting to explore the effect of enhanced second harmonic generation by including within the apertures materials such as GaAs. A further proposal is to include apertures of different dimensions in the same array to achieve broadband transmission characteristics.

Bibliography

[1] T. W. Ebbesen, H. J. Lezec, H. F. Ghaemi, T. Thio and P. A. Wolff. "Extraordinary optical transmission through sub-wavelength hole arrays." *Nature*, **391**(6668), 667-669, 1998.

[2] N. Engheta. "Circuits with light at nanoscales: Optical nanocircuits inspired by metamaterials." *Science*, **317**, 1698-702, 2007.

[3] F. D. Nunes and J. Weiner. "Equivalent circuits and nanoplasmonics." *IEEE T. Nanotechnol.*, **7**, 2009.

[4] J. Weiner. "The physics of light transmission through subwavelength apertures and aperture arrays." *Rep. Prog. Phys.*, **72**, 064401, 2009.

[5] W. Fan, S. Zhang, N. C. Panoiu, A. Abdenour, S. Krishna, R. M. Osgood, K. J. Malloy and S. R. J. Brueck. "Second harmonic generation from a nanopatterned isotropic nonlinear material." *Nano Lett.*, **6**, 1027–1030, 2006.

[6] T. J. Kim, T. Thio, T. W. Ebbesen, D. E. Grupp and H. J. Lezec. "Control of optical transmission through metals perforated with subwavelength hole arrays." *Opt. Lett.*, **24**, 256, 1999.

[7] L. Martín-Moreno, F. J. Garcia-Vidal, H. J. Lezec, K. M. Pellerin, T. Thio, J. B. Pendry and T. W. Ebbesen. "Theory of Extraordinary Optical Transmission through Subwavelength Hole Arrays." *Phys. Rev. Lett.*, **86**, 1114, 2001.

[8] J. C. Yang, J. Ji, J. M. Hogle and D. N. Larson. "Multiplexed plasmonic sensing based on small-dimension nanohole arrays and intensity interrogation." *Biosens. Bioelectron.*, **24**(8), 2334–2338, 2009.

[9] J. C. Yang, J. Ji, J. M. Hogle and D. N. Larson. "Metallic nanohole arrays on fluoropolymer substrates as small label-free real-time bioorobes." *Nano Lett.*, **8**(9): 2718-2724, 2008.

[10] B. Ung and Y. Sheng. "Optical surface waves over metallo-dielectric nanostructures: Sommerfeld integrals revisited." *Optics Express*, **16**(12), 90739086, 2008.

[11] P. R. H. Stark, A. E. Halleck and D. N. Larson. "Short order nanohole arrays in metals for highly sensitive probing of local indices of refraction as the basis for a highly multiplexed biosensor technology." *Methods*, **37**(1), 3747, 2005.

[12] A. G. Brolo, R. Gordon and K. L. Kavanagh. "A new generation of sensors based on extraordinary light transmission." *Acc. Chem. Res.*, **41**(8), 1049-1057, 2008.

[13] M. Beruete, M. Sorolla and I. Campillo. "Left-Handed Extraordinary Optical Transmission through a Photonic Crystal of Subwavelength Hole Arrays." *Optics Express*, **14**(12), 5445-5455, 2006.

[14] S. Zhang, W. Fan, N. C. Panoiu, K. J. Malloy, R. M. Osgood and S. R. J. Brueck. "Experimental demonstration of near-infrared negative-index metamaterials." *Phys. Rev. Lett.*, **95**, 137404, 2005.

[15] L. Lin, X. M. Goh, L. P. McGuinness and A. Roberts. "Plasmonic Lenses Formed by Two-Dimensional Nanometric Cross-Shaped Aperture Arrays for Fresnel-Region Focusing." *Nano Lett.*, **10**(5), 19361940, 2010.

[16] H. T. Chen, W. J. Padilla1, J. M. O. Zide, A. C. Gossard, A. J. Taylor and R. D. Averitt. "Active terahertz metamaterial devices." *Nature*, **444**, 597-600, 2006.

[17] S. Xiao, U. K. Chettiar, A. V. Kildishev, V. Drachev, I. C. Khoo and V. M. Shalaev. "Tunable magnetic response of metamaterials." *Appl. Phys. Lett.*, **95**, 033115, 2009.

[18] I. M. Pryce, K. Aydin, Y. A. Kelaita, R. M. Briggs and H. A. Atwater. "Highly strained compliant optical metamaterials with large frequency tunability." *Nano Lett.*, **10**(10), 4222-4227, 2010.

[19] R. E. Collin and W. H. Eggimann. "Dynamic interaction fields in a two-dimensional lattice." *IRE Trans. Microwave Theory Tech.*, **10**, 110-115, 1961.

[20] W. H. Eggimann and R. E. Collin. "Electromagnetic diffraction by a planar array of circular disks." *IRE Trans. Microwave Theory Tech.*, **10**, 528-535, 1962.

[21] R. Ulrich. "Far-infrared properties of metallic mesh and its complementary structure." *Infrared Phys.*, **7**(1), 37-55, 1967.

[22] C. C. Chen. "Diffraction of electromagnetic waves by a conducting screen perforated periodically with circular holes." *IEEE Trans. Microwave Theory Tech.* **19**(5), 475-481, 1971.

[23] D. Maystre. "Electromagnetic Theory of Gratings." edited by R. Petit, Springer-Verlag, Berlin, 63-100, 1980.

[24] R.C. McPhedran, G. H. Derrick and L. C. Botten. "Electromagnetic Theory of Gratings." Edited by R. Petit Springer-Verlag, Berlin, 227-276, 1980.

[25] R. Mittra, C. H. Chan and T. Cwik. "Techniques for analyzing frequency selective surfaces: A review." *Proc. IEEE*, **76**, 1593-1615, 1988.

[26] H.A. Bethe. "Theory of Diffraction by Small Holes." *Phys. Rev.*, **66**, 163–182, 1944.

[27] R. H. Ritchie. "Plasma Losses by Fast Electrons in Thin Films." *Phys. Rev.*, **106**, 874-881, 1957.

[28] C. J. Powell and J. B. Swan. "Origin of the Characteristic Electron Energy Losses in Aluminum." *Phys. Rev.*, **115**, 869-875, 1959.

[29] J. C. Gmez-Rivas, C. Schotsch, P. Haring Bolivar and H. Kurz. "Enhanced transmission of THz radiation through sub-wavelength holes." *Phys. Rev. B*, **68**, 201306, 2003.

[30] R. H. Ritchie, E. T Arakawa, J. J. Cowan and R. N. Hamm. "Surface-Plasmon Resonance Effect in Grating Diffraction." *Phys. Rev. Lett.*, **21**, 1530-1533, 1968.

[31] H. Raether. "Surface Plasmons." Springer, Berlin, 1988.

[32] Y. J. Chen, E. S. Koteles, R. J. Seymour, G. J. Sonek and J. M. Ballantyne. "Surface plasmons on gratings: Coupling in the minigap regions." *Solid State Commun.* **46**, 95-99, 1983.

[33] S. C. Kitson, W. L. Barnes and J. R. Sambles. "Full photonic band gap for surface modes in the visible." *Phys. Rev. Lett.* **77**, 2670-2673, 1996.

[34] R. A. Watts, J. B. Harris, A. P. Hibbins, T. W. Preist and J. R. Sambles. "Optical excitation of surface plasmon polaritons on 90 degrees and 60 degrees bi-gratings." *J. Mod. Opt.* **43**, 1351-1360, 1996.

[35] G. H. Derrick, R. C. McPhedran, D. Maystre and M. Neviere. "Crossed gratings: A theory and its applications." *Appl. Phys.* **18**, 39-52, 1979.

[36] A. V. Zayats, I. I. Smolyaninov and A. A. Maradudin. "Nano-optics of surface plasmon polaritons." *Phy. Rep.*, **408**, 131–314 2005.

[37] F. J. Garca-Vidal, L. Martín-Moreno, T. W. Ebbesen and L. Kuipers. "Light passing through subwavelength apertures." *Rev. Mod. Phys.*, **82**, 729–787, 2010.

[38] S. A. Maier. "Plasmonics: Fundamentals and Applications." Springer, New York, 2007.

[39] F. Falcone, T. Lopetegi, M. A. G. Laso, J. D. Baena, J. Bonache, M. Beruete, R. Marqus, F. Martn and M. Sorolla. "Babinet principle applied to the design of metasurfaces and metamaterials." *Phys. Rev. Lett.*, **93**, 197401–4, 2004.

[40] J. D. Jackson. "Classical Electrodynamics." Wiley, New York, page 488 3rd ed., 1999.

[41] F. J. Garcia-Vidal, L. Martín-Moreno, H. J. Lezed and T. W. Ebbesen. "Multiple paths to enhance optical transmission through a single subwavelength slit." *Phys. Rev. Lett.*, **90**, 213901, 2003.

[42] S. Selcuk, K. Woo, D. B. Tanner, A. F. Hebard, A. G. Borisov and S. V. Shabanov. "Trapped electromagnetic modes and scaling in the transmittance of perforated metal films." *Phys. Rev. Lett.*, **97**, 067403, 2006.

[43] Y. Ekinci, H. H. Solak and C. David. "Extraordinary optical transmission in the ultraviolet region through aluminum hole arrays." *Opt. Lett.*, **32**, 172-174, 2007.

[44] F. Przybilla, A. Degiron, J. Y. Laluet, C. Genet and T. W. Ebbesen. "Optical transmission in perforated noble and transition metal films." *J. Opt. A, Pure Appl. Opt.*, **8**, 458-463, 2006.

[45] M. Sun, J. Tian, Z. Y. Li, B. Y. Cheng, D. Z. Zhang, A. Z. Jin and H. F. Yang. "The role of periodicity in enhanced transmission through subwavelength hole arrays." *Chin. Phys. Lett.*, **23**, 486-488, 2006.

[46] J. Elliott, I. I. Smolyaninov, N. I. Zheludev and A. V. Zayats. "Polarization control of optical transmission of a periodic array of elliptical nanoholes in a metal film." *Opt. Lett.*, **29**, 1414-1416, 2004.

[47] R. Gordon, A. G. Brolo, A. McKinnon, A. Rajora, B. Leathem and K. L. Kavanagh. "Strong polarization in the optical transmission through elliptical nanohole arrays." *Phys. Rev. Lett.*, **92**, 037401, 2004.

[48] K. J. Koerkamp, S. Enoch, F. B. Segerink, N. F. van Hulst and L. Kuipers. "Strong influence of hole shape on extraordinary transmission through periodic arrays of subwavelength holes." *Phys. Rev. Lett.*, **92**, 183901, 2004.

[49] J. A. Matteo, D. P. Fromm, Y. Yuen, P. J. Schuck, W. E. Moerner and L. Hesselink. "Spectral analysis of strongly enhanced visible light transmission through single C-shaped nanoapertures." *App. Phys. Lett.*, **85**, 648-650, 2004.

[50] N. Liu, H. Liu, S. N. Zhu and H. Giessen. "Stereometamaterials." *Nat. Photon.*, **3**, 157–162, 2009.

[51] V. G. Kravets, F. Schedin and A. N. Grigorenko. "Plasmonic blackbody: Almost complete absorption of light in nanostructured metallic coatings." *Phys. Rev. B*, **78**, 205405, 2008.

[52] J. M. Hao, J. Wang, X. L. Liu, W. J. Padilla, L. Zhou and M. Qiu. "High performance optical absorber based on a plasmonic metamaterial." *Appl. Phys. Lett.*, **96**, 251104, 2010.

[53] M. Thiel, M. S. Rill, G. von Freymann and M. Wegener. "Three-dimensional bi-chiral photonic crystals." *Adv. Mater.*, **21**, 4680–4682, 2009.

[54] R. A. Shelby, D. R. Smith and S. Schultz. "Experimental verification of a negative index of refraction." *Science*, **292**, 77–79, 2001.

[55] V. M. Shalaev, W. Cai, U. K. Chettiar, H. K. Yuan, A. K. Sarychev, V. P. Drachev and A. V. Kildishev. "Negative index of refraction in optical metamaterials." *Opt. Lett.*, **30**, 3356–3358, 2005.

[56] S. Zhang, Y. S. Park, J. S. Li, X. C. Lu, W. L. Zhang and X. Zhang. "Negative Refractive Index in Chiral Metamaterials." *Phys. Rev. Lett.*, **102**, 023901, 2009.

[57] J. L. Yan, Q. Hao, J. S. T Smalley, J. Liou, I. C. Khoo and T. J. Huang."A frequency-addressed plasmonic switch based on dual-frequency liquid crystals." *Appl. Phys. Lett.*, **97**, 091101, 2010

[58] R. Singh, E. Plum, W. Zhang and N. I. Zheludev. "Highly tunable optical activity in planar achiral terahertz metamaterials." *Opt. Express*, **18**, 13425-13430, 2010.

[59] C. Menzel, C. Helgert, C. Rockstuhl, E. -B. Kley, A. Tnnermann, T. Pertsch and F. Lederer. "Asymmetric transmission of linearly polarized light at optical metamaterials." *Phys. Rev. Lett.*, **104**, 253902, 2010.

[60] H. T. Chen, H. Yang, R. Singh, J. F. O'Hara, A. K. Azad, S. A. Trugman, Q. X. Jia and A. J. Taylor. "Tuning the resonance in high temper-

ature superconducting terahertz metamaterials." *Pys. Rev. Lett.*, **105**, 247402, 2010.

[61] Ryan M. Roth, Nicolae C. Panoiu, Matthew M. Adams, Jerry I. Dadap and Richard M. Osgood, Jr. "Polarization-tunable plasmon-enhanced extraordinary transmission through metallic films using asymmetric cruciform apertures." *Opt. Lett.*, **32**, 3414-3416, 2007.

[62] R. W. Wood. "On a remarkable case of uneven distribution of light in a diffraction grating spectrum." *Philos. Mag.*, **4**, 396, 1902.

[63] R. W. Wood. "Anomalous Diffraction Gratings." *Phys. Rev.*, **48**, 928, 1935.

[64] L. Lin, L. B. Hande and A. Roberts. "Resonant nanometric cross-shaped apertures: Single apertures versus periodic arrays." *Appl. Phys. Lett.*, **95**, 201116, 2009.

[65] H. J. Lezec, A. Degiron, E. Devaux, R. A. Linke, L. Martin-Moreno, F. J. Garcia-Vidal and T. W. Ebbesen. "Beaming Light from a Subwavelength Aperture." *Science*, **297**, 820, 2002.

[66] R. F. Oulton, V. J. Sorger, T. Zentgraf, R. Ma, C. Gladden, L. Dai, G. Bartall and X. Zhang. "Plasmon Lasers at Deep Subwavelength Scale." *Nature*, **461**,7264, 2009.

[67] G. Stengel and W. Knoll. "Surface plasmon field-enhanced fluorescence spectroscopy studies of primer extension reactions." *Nucl. Acids Res.* **7**, 2005.

[68] D. Canneson, I. Mallek-Zouari, S. Buil, X. Quelin, C. Javaux, B. Mahler, B. Dubertret and J. -P. Hermier. "Strong Purcell effect observed in single thick-shell CdSe/CdS nanocrystals coupled to localized surface plasmons." *Phys. Rev* **84**, 245423, 2011.

[69] L. Lin and A. Roberts. "Angle-robust resonances in cross-shaped aperture arrays." *Appl. Phys. Lett.*, **97**, 061109, 2010.

[70] A. G. Brolo, R. Gordon, B. Leathem and K. L. Kavanagh. "Surface plasmon sensor based on the enhanced light transmission through arrays of nanoholes in gold films." *Langmuir*, **20**, 4813-4815, 2004.

[71] W. Fan, S. Zhang, K. J. Malloy, S. R. J. Brueck, N. C. Panoiu and R. M. Osgood. "Second harmonic generation from patterned GaAs inside a subwavelength metallic hole array." Optics Express, **14**, 9570-9575, 2006.

[72] E. Laux, C. Genet, T. Skauli and T. W. Ebbesen. "Plasmon Photon Sorters for Spectral and Polarimetric Imaging." *Nature Photonics*, **2**, 161-164, 2008.

[73] A. Drezet, C. Genet and T. W. Ebbesen. "Miniature plasmonic wave plates." *Phys. Rev. Lett.*, **10**, 043902, 2008.

[74] J. R. Krenn, H. Ditlbacher, G. Schider, A. Hohenau, A. Leitner and F. R. Aussenegg. "Surface plasmon micro- and nano-optics." *J. Microsc.*, **209**, 167-172, 2003.

[75] Z. W. Liu, J. M. Steele, W. Srituravanich, Y. Pikus, C. Sun and X. Zhang. "Focusing surface plasmons with a plasmonic lens." *Nano Lett.*, **5**(9) 1726-1729, 2005.

[76] L. Novotny and B. Hecht. "Principles of nano-optics." 379-387, Cambridge, 2006.

[77] M. Fox. "Optical properties of solids." Oxford, 29-33, 2001.

[78] S. M. Nie and S. R. Emory. "Probing single molecules and single nanoparticles by surface-enhanced Raman scattering." *Science*, **275**, 1102–1106, 1997.

[79] K. Kneipp, Y. Wang, H. Kneipp, L. T. Perelman, I. Itzkan, R. R. Dasari and M. S. Feld. "Single molecule detection using surface-enhanced Raman scattering (SERS)." *Phys. Rev. Lett.*, **78**, 1667–1670, 1997.

[80] C. L. Haynes and R. P. Van Duyne. "Plasmon-sampled surface-enhanced Raman excitation spectroscopy." *J. Phys. Chem. B*, **107**, 7426–7433, 2003.

[81] B. Knoll and F. Keilmann. "Near-field probing of vibrational absorption for chemical microscopy." *Nature*, **399**, 134–137, 1999.

[82] T. Ichimura, N. Hayazawa, M. Hashimoto, Y. Inouye and S. Kawata. "Tip-enhanced coherent anti-Stokes Raman scattering for vibrational nano-imaging." *Phys. Rev. Lett.*, **92**, 220801, 2004.

[83] R. M. Roth, N. C. Panoiu, M. M. Adams, R. M. Osgood, C. C. Neacsu and M. B. Raschke. "Resonant-plasmon field enhancement from asym-

metrically illuminated conical metallic-probe tips." *Opt. Express.*, **14**, 2921–2931, 2006.

[84] J. L. West and N. J. Halas. "Engineered nanomaterials for biophotonics applications: Improving sensing, imaging, and therapeutics." *Annu. Rev. Biomed. Eng.*, **5**, 285–292, 2003.

[85] C. Soennichsen and A. P. Alivisatos. "Gold nanorods as novel nonbleaching plasmon-based orientation sensors for polarized single-particle microscopy." *Nano. Lett.*, **5**, 301–304, 2005.

[86] N. Liu, M. Mesch, T. Weiss, M. Hentschel and H. Giessen. "Infrared perfect absorber and its application as plasmonic sensor." *Nano. Lett.*, **10**, 2342–2348, 2010.

[87] G. Boisde and A. Harmer. "Chemical and biochemical sensing with optical fibers and waveguides." Arthech House, Boston, 1996.

[88] P. Muhlschlegel, H. J. Eisler, O. J. F. Martin, B. Hecht and D. W. Pohl. "Resonant optical antennas." *Science*, **308**, 1607–1609, 2005.

[89] P. J. Schuck, D. P. Fromm, A. Sundaramurthy, G. S. Kino and W. E. Moerner. "Improving the mismatch between light and nanoscale objects with gold bowtie nanoantennas." *Phys. Rev. Lett.*, **94**, 017402, 2005.

[90] T. H. Taminiau, R. J. Moerland, F. B. Segerink, L. Kuipers and N. F. van Hulst. "$\lambda/4$ resonance of an optical monopole antenna probed by single molecule fluorescence." *Nano. Lett.*, **7**, 28–33, 2007.

[91] N. W. Ashcroft and N. D. Mermin. "Solid state physics." Brooks/Cole, Boston, 1976.

[92] D. J. Griffiths. "Introduction to Electrodynamics." Prentice Hall, NJ,1999.

[93] P. Lalanne. "Improved formulation of the coupled-wave method for two-dimensional gratings." *J. Opt. Soc. Am. A*, **14**, 1592-1598, 1997

[94] M. G. Moharam, E. B. Grann and D. A. Pommet. "Formulation for stable and efficient implementation of the rigorous coupled-wave analysis of binary gratings." *J. Opt. Soc. Am. A*, **12**, 1068-1076, 1995.

[95] M. G. Moharam, E. B. Grann, D. A. Pommet and T. K. Gaylord. "Stable implementation of the rigorous coupled-wave analysis for surface-relief gratings: Enhanced transmittance matrix approach." *J. Opt. Soc. Am. A* **12**, 1068-1076, 1995.

[96] M. G. Moharam and T. K. Gaylord. "Rigorous coupled-wave analysis of metallic surface-relief gratings." *J. Opt. Soc. Am. A* **3**, 1780, 1986.

[97] M. G. Moharam and T. K. Gaylord. "Rigorous coupled-wave analysis of grating diffraction-E mode polarization and losses." *J. Opt. Soc. Am.*, **73**, 451-455, 1983.

[98] T.K. Gaylord and M. G. Moharam. "Analysis and applications of optical diffraction by gratings." *Proceedings of the IEEE*, **5**, 894-937, 1985.

[99] C. L. Liu and J. W. S. Liu. "Linear systems analysis." McGraw-Hill, New York, 1975.

[100] M. G. Moharam and T. K. Gaylord. "Three-dimensional vector coupled-wave analysis of planar-grating diffraction." *J. Opt. Soc. Am.* **73**, 1105-1112, 1983.

[101] E. Collet. "Polarized light: Fundamentals and applications." Dekker, New York, 1993.

[102] H. F. Ghaemi, T. Thio, D. E. Grupp, T. W. Ebbesen and H. J. Lezec. "Surface plasmons enhance optical transmission through subwavelength holes." *Phys. Rev. B*, **58**, 6779, 1998.

[103] R. Qiang, J. Chen, T. Zhao, S. Wang, P. Ruchhoeft and M. Morgan. "Modeling of infrared bandpass filters using a three-dimensional FDTD method." *Electr. Lett.*, **41**, 914–915, 2005.

[104] C. Imhof and R. Zengerle. "Pairs of metallic crosses as a left-handed metamaterial with improved polarization properties." *Opt. Express.*, **14**, 8257–8262, 2006.

[105] D. F. Bezuidenhout. "OpticConstHandbookSi." (Vol. 2), Academic Press, 1991.

[106] D. F. Edwards. "OpticConstHandbookSi." (Vol. 1), Academic Press, 1991.

[107] I. H. Malitson. "A Redetermination of Some Optical Properties of Calcium Fluoride" *Applied Optics*, **2**, 1103-1107, 1963.

[108] V. E. Krohn. "Liquid metal droplets for heavy particle propulsion." *Progress in Astronautics and Rocketry*, **5**, 73–80, 1961.

[109] V. E. Krohn and G. E. Ringo. "Ion source of high brightness using liquid metal." *Appl. Phys. Lett.*, **27**, 479-481, 1975.

[110] N. Yao. "Focused Ion Beam Systems." Cambridge, 2-29, 2007.

[111] L. A. Gianuzzi and F. A. Stevie. "Introduction to focused ion beams." Springer, Boston 1-11, 2005.

[112] A. A. Michelson. "Visibility of interference-fringes in the focus of a telescope." *Phil. Mag.*, **5**, 256, 1891.

[113] A. A. Michelson. "On the application of interference-methods to spectroscopic measurements." *Phil. Mag.*, **5**, 280, 1892.

[114] P. D. Sumner, M. C. Abrams and J. W. Brault. "Fourier transform spectrometry." Academic Press, New York, 2001.

[115] P. R. Griffiths and J. A. De Haseth. "Fourier transform infrared spectrometry." Wiley, New York, 1986.

[116] IUPAC. "Compendium of chemical terminology, 2nd ed. (the Gold Book)." Compiled by A. D. McNaught and A. Wilkinson. Blackwell Scientific Publications, Oxford, 1997.

[117] E. J. King. "Acid-Base Equilibria." Pergamon Press, Oxford, 1965.

[118] U. Kreibig and M. Vollmer. "Optical Properties of Metallic Clusters." Springer, Berlin, 1995.

[119] M. A. Ordal, R. J. Bell, R. W. Alexander Jr, L. L. Long and M. R. Querry. "Optical properties of fourteen metals in the infrared and far

infrared - Al, Co, Cu, Au, Fe, Pb, Mo, Ni, Pd, Pt, Ag, Ti, V, and W." *Appl. Opt.*, **24**, 44934499, 1985.

[120] F. L. Pedrotti and L. S. Pedrotti. "Introduction to Optics." Prentice Hall, New Jersey, 1993.

[121] A. Papakostas, A. Potts, D. M. Bagnall, S. L. Prosvirnin, H. J. Coles and N. I. Zheludev. "Optical manifestations of planar chirality." *Phys. Rev. Lett.*, **90**, 107404, 2003.

[122] A. V. Krasavin, A. S. Schwanecke, N. I. Zheludev, M. Reichelt, T. Stroucken, S. W. Koch and E. M. Wright. "Polarization conversion and focusing of light propagating through a small chiral hole in a metallic screen." *Appl. Phys. Lett.*, **86**, 201105, 2005.

Appendix A

Published Paper

Polarization-induced tunability of localized surface plasmon resonances in arrays of sub-wavelength cruciform apertures. **Paul G. Thompson**, Claudiu G. Biris, Edward J. Osley, Ophir Gaathon, Richard M. Osgood, Jr., Nicolae C. Panoiu and Paul A. Warburton. *Optics Express*, **19**(25), 25035-25047, 2011.